Pulse propagation in the pulmonary and systemic arteries

by

Gareth D.A. Vaughan

A thesis submitted to the

Faculty of Information and Mathematical Sciences

at the University of Glasgow

for the degree of

Doctor of Philosophy

September 2009

Abstract

The one-dimensional model of Olufsen (2000) [34] for blood flow in the systemic arteries has been extended and built upon in a number of ways. Firstly, it has been applied to hypotheses of diseases of the systemic circulation, and that of the microcirculation. With a view to better understanding the microcirculation (the smallest vessels of the systemic circulation) and its diseases, the model has been extended to provide predictions of the propagating pressure pulse and flow rate in small arteries.

Secondly, Olufsen's model has been used as a base upon which to build a model of the pulmonary circulation, incorporating both the pulmonary arterial and venous circulations, with detailed simulations of pressure and flow predicted in the large pulmonary arteries and large pulmonary veins. To this end, a new model has been developed to describe a connected network of small arteries and small veins, replacing the small arterial model used as an outflow condition in the original model. A new outflow condition to describe the return of blood from the pulmonary venous system to the left atrium of the heart has also been implemented.

Finally, this new pulmonary model has been applied to various hypotheses as to the causes of diseases and disorders of the pulmonary circulation, providing predictions of pressure and flow in the large pulmonary arteries and veins in both normal and abnormal circumstances, and showing agreement with clinical observations.

Acknowledgements

First and foremost, I would like to thank my supervisor Nick Hill for his advice, support and encouragement over the past few years. I also wish to thank Mette Olufsen for her contribution to this project, and for her hospitality during my two visits to North Carolina. I am also extremely grateful to Chris Sainsbury and Martin Johnson for their invaluable input and expertise over the course of my studies, and to Charlie Peskin for suggesting the equations used in Chapter 4.

I would also like to acknowledge each and every person I have shared an office with in the last four years — 24 at the last count! — but in particular Robert Kerr and John Walker for their assistance with Linux, C++, LaTeX and lunch related issues.

Finally, I must acknowledge the continued support of my friends and family — my parents, sister and brother — over these last four years.

Statement

This thesis is submitted in accordance with the regulations for the degree of Doctor of Philosophy at the University of Glasgow.

Contents

List of Figures

List of Tables

Chapter 1

Introduction

Physiological fluid dynamics, particularly the mathematical modelling of the propagation of the pressure pulse in arteries, is an area of applied mathematics that has witnessed great advancement in the last half century. The drive behind this has not least been because of the strong multi-disciplinary aspect of an area that is of great interest to both mathematicians and clinical investigators alike, but also the explosion in the availability of ever improving high powered computational resources has led to more detailed investigation of fluid dynamical phenomena, with the goal of further enhancing our understanding of the cardiovascular system.

The history of fluid mechanics stretches as far back as Archimedes who, in the 3rd century BC, first investigated hydrostatics and buoyancy. Significant advancements in the field were developed over the centuries by the likes of Isaac Newton (viscosity, C17), Blaise Pascal (hydrostatics, C17), Daniel Bernoulli (hydrodynamics, C18), Jean Louis Marie Poiseuille (viscous/laminar flow, C19) [1], and significantly Claude-Louis Navier and George Gabriel Stokes (Navier-Stokes equations, C19), but it was the more recent work of mathematicians such as John R Womersley and Sir James Lighthill that developed the field of physiological fluid dynamics and the study of blood flow in arteries.

A paper in memorial of Lighthill by Timothy J Pedley, 2003 [39] describes some of his contribution to the field of cardiovascular fluid dynamics, as well as summarising other contributions to the field in recent history, including those of Womersley, and touching on that of Mette Olufsen, upon whose work much of this thesis is based.

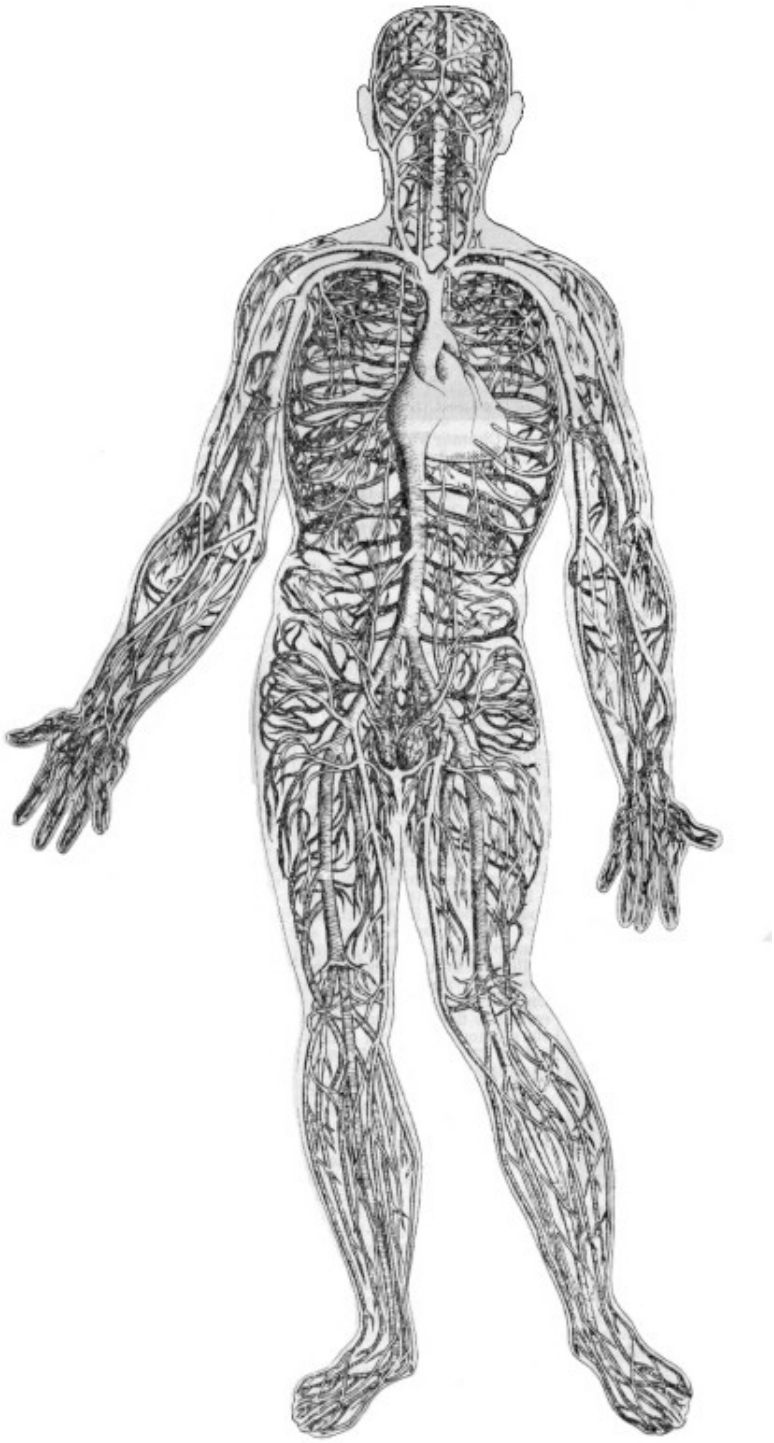

Figure 1.1: The Vein Man, Vesalius (1554)

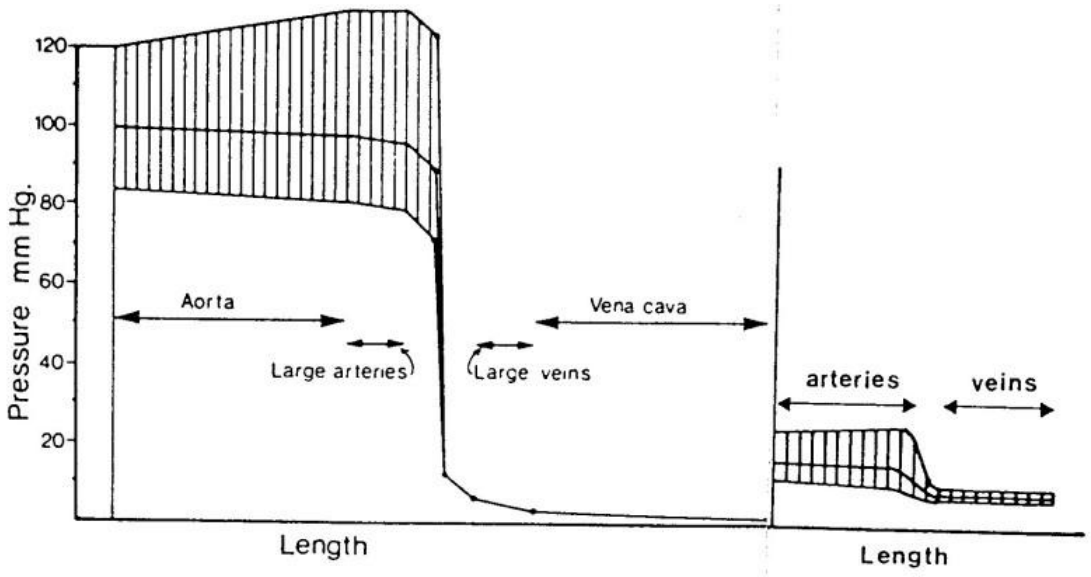

Figure 1.2: Pressure levels along the length of the systemic circulation (left hand side) and the pulmonary circulation (right hand side) [30].

The Cardiovascular Circulatory System

The mechanism by which blood is transported around the human body is the cardiovascular circulatory system, consisting of two distinct parts - the systemic circulation, and the pulmonary circulation - both connected to the heart. By far the larger of the two, the systemic circulation originates at the left ventricle of the heart, and its purpose is to transport oxygenated blood to the many tissues of the body where oxygen and carbon dioxide are exchanged, and then return the deoxygenated blood to the right atrium of the heart. The pulmonary circulation, emanating from the right ventricle, then carries blood to the lungs to be re-oxygenated, before returning to the heart at the left atrium to begin the entire circulatory process over again [30], [37].

In both systemic and pulmonary circulations, the vessels that carry blood away from the heart are the arteries, while the veins are the vessels through which blood returns to the heart. The smallest arteries may be referred to as arterioles, and similarly the smallest veins as venules, while the tiny interconnecting vessels are the capillaries.

The heart, through beating, regularly ejects blood from the left and right ventricles into the aorta (of the systemic circulation) and the main pulmonary artery (of the pulmonary circulation), and valves prevent this fluid from flowing immediately back into the heart. Since the arterial walls are elastic, this increase in pressure due to the introduction of

more fluid causes the vessel to distend, and the fluid is set in motion. The restoring force of the vessel walls, combined with the inertia of the blood results in a pressure wave propagating along the artery. As indicated in Figure 1.2, the pressure in the systemic arteries is considerably higher than in the systemic veins or any part of the pulmonary circulation. This means that the walls of the large systemic arteries are generally thick and strong, while the systemic veins and pulmonary arteries and veins are generally thinner.

As a propagating pressure pulse reaches a bifurcation - where a larger artery splits into two smaller arteries - part of the energy of the pulse wave is transmitted into each of the smaller arteries, and part is reflected back along the original artery. A bifurcation is said to be 'well-matched' if most of the energy of an incoming pressure pulse is transmitted and very little reflected. Most notably in physiological bifurcations, the iliac bifurcation is not well-matched and a significant proportion of the pressure pulse is reflected. This reflected wave component can be seen in the shape of the pressure-time waveform measured in the aorta.

Why model the circulation?

There are a number of reasons why we may wish to study the mechanics of the cardiovascular circulatory system and physiological flows [38]. From a purely physiological point of view, we may wish simply to further improve our understanding of how the circulatory system works. In terms of pathophysiology, we may study how the circulatory system might go wrong to assist understanding of the origins and development of disease, and similarly for diagnosis we may attempt to infer what has gone wrong from measurements of, for example, blood pressure. Finally there is the possibility of a cure - detection and quantification of a stenosis may serve as the basis for surgical intervention, while simulation of physiological flows is extremely important in the design of prosthetic devices.

Diseases of the Circulation

The majority of deaths in the developed world result from cardiovascular diseases, most of which are associated with abnormal flow in the arteries [25], [32]. Both the development and effects of atherosclerosis are strongly linked to fluid mechanical factors [18], the result of which can lead to constriction or blockage (stenosis) of arteries, and ultimately heart attacks and strokes. Stiffening of the arterial vessel walls, and the resulting effect on blood flow through these vessels, generally occurs with ageing, and has been linked to

hypertensive abnormalities in both the systemic [29] and pulmonary [43] circulations.

While the above disorders are generally diseases of the larger arteries of the circulation, in both the pulmonary and systemic circulations problems may also arise in the smaller vessels. A reduction in density of vessels in the vascular beds serving some tissues, whether due to anatomical absence of vessels (vascular remodelling), occlusion or lack of perfusion, has also been linked to instances of hypertension, although whether this is a cause of, or result of the increased blood pressure is not clear [12], [51]. It is important, therefore, to be able to study the effect of blood flow in the small arteries, as well as the large arteries.

One-Dimensional theory of pulse propagation in arteries

Linear Theory

Linear models of blood flow in large arteries begin by considering an infinitely long, distensible tube of uniform area A, containing incompressible, inviscid fluid of density ρ, perturbed by small, long wavelength disturbances and governed by three equations — conservation of fluid mass and momentum, and a state equation or "tube law" relating cross-sectional area A to local transmural pressure P [37]. Some straightforward analysis shows that these disturbances obey the linear wave equation, propagating without changing shape at wave speed c_0, called the Moens–Korteweg wave speed (although first discovered by Thomas Young [55]).

Based on continuity of pressure and flow rate at a junction, peaking of the pressure wave can be explained by reflections which occur at bifurcations where there is a discontinuity in the characteristic impedance, $Y = A/\rho c$, of vessels. Incident and reflected waves travel in opposite directions with the same wave speed (in that particular vessel), and the reflected wave is in phase with the incident wave (causing an increase in pressure wave amplitude in the parent vessel) if the sum of the admittances of the daughter vessels is less than that of the parent vessel, called a "closed end" junction, or of opposite phase (causing a reduction in parent vessel pressure wave amplitude) if the sum of the admittances of the daughter vessels is more than that of the parent vessel, called an "open end" junction. If the sum of the daughter vessel admittances equals that of the parent vessel, there is no reflection and the junction is well-matched.

This simple analysis, however, predicts pressure and flow waveforms that are in phase with one another, contrary to what is clinically observed. The phase difference between these waveforms was explained by the analysis of Womersley [54], who introduced viscous

and viscoelastic effects, and the Womersley parameter $\alpha = a\sqrt{\omega/\nu}$, where a is vessel radius, ω is the angular frequency of the oscillation in pressure gradient and ν is kinematic viscosity. This parameter relates pulsatile frequency and viscous effects — when α is small (≤ 1), the frequency of oscillations is low enough that a parabolic velocity profile has time to develop during each cycle, and the flow will be very nearly in phase with the pressure gradient, but when α is large (≥ 10), as is the case in the large arteries, the velocity profile is relatively flat or plug-like, and there is a phase lag between the pressure gradient and the flow.

Nonlinear theory

The nonlinear form of the governing equations of blood flow in arteries — the conservation of fluid mass and momentum, and the state equation — are hyperbolic in form, and can be integrated using the method of characteristics. This type of analysis suggests that nonlinear waves propagate in the forward and backward directions in a vessels with variable speeds, meaning that characteristics can run together and form discontinuities or shocks. In normal physiological conditions, a shock would not be expected to form, however in cases of aortic valve incompetence the heart compensates by ejecting a greater volume of blood and clinicians report a 'pistol-shot' pulse, likely to correspond to the formation of a shock.

It is also possible, and in some cases preferable, to compute solutions to the governing equations numerically using finite difference methods [17].

Models of the Circulation

Attempts to model the full arterial circulation generally begin with the same basic building blocks — dividing the arterial tree up into short cylindrical vessel segments between bifurcations in which the axisymmetric flow and pressure can be calculated numerically, with an inflow condition at one end, and with continuous pressure and conserved flow into its daughter vessels at the other end, or an outflow condition if it is a terminal vessel of the tree. The inflow condition may be a prescribed pressure-time, or flow-time relationship, while a lumped resistance to flow is generally applied as an outflow condition after a few generations of large vessels, and this is enough to produce decent predictions of blood flow and pressure in the large arteries [42].

Olufsen's Model

Faced with the increasing complexity of describing more and more generations of the arterial tree in order to improve the accuracy of these models, Mette Olufsen [33], [34] devised a method of analytically determining the dynamic, frequency dependent impedance of a peripheral arterial tree, to be applied as an outflow condition to a model of just three or four generations of large arteries simulated in detail. The output of her model showed a much better phase relationship between pressure and flow-rate wave forms than models with constant peripheral admittances.

The advantage of Olufsen's approach over other one dimensional models is that, although they are not simulated in detail, in a fluid dynamical sense the smaller arteries of each vascular bed are included in the model by means of the dynamic impedance (which may be different for each vascular bed). This approach is also not any less efficient than other one-dimensional models, due to the fact that these impedances need only be calculated once, and not at every time step of the numerical scheme (the two-step Lax-Wendroff method) being used to resolve detailed flows and pressures in the large arteries.

Three-Dimensional Models

As large scale computation has become more feasible, it is now possible to compute detailed three-dimensional flows in large arteries. While this is undoubtedly useful in computing flows around, for example, a stenosis, the reasons for continuing with a one-dimensional model are two-fold. Firstly, it is still not computationally feasible to simulate a model of the arterial system in any higher dimension, and secondly that measured flow and pressure profiles during surgery are one-dimensional.

The Pulmonary Circulation

The pulmonary circulation has received relatively little attention in terms of pressure and flow modelling when compared to the systemic circulation. Unlike the systemic circulation, where the pressure drop occurs across the arteries, the pulmonary pressure drop continues across both the arterial and venous sides of the circulation, and including this venous tree into a one-dimensional model along with an arterial tree is obviously a challenge.

Existing models of the pulmonary circulation [5], [6] have applied a constant pressure gradient over the circulation, along with detailed models of small tree structures, to in-

vestigate regions of perfusion when the lung is in different orientations. A group headed by C.A. Taylor have recently developed detailed, patient-specific one-dimensional models of blood flow in pulmonary arteries [47], [50], but there has not to our knowledge been a model of pulsatile flow and pressure in the pulmonary circulation including the pulmonary veins.

Aims of this thesis

There are two aims to the work in this thesis. The first aim is to further develop the model of Olufsen [34] to investigate in more detail pulse pressure and flow in the small arteries of the systemic circulation, as well as its application to diseases of the circulation.

The second aim is to develop a new model, based on Olufsen's systemic model, to describe the pulmonary circulation. The particular aims of this new model are to produce detailed simulations of pressure and flow in the large pulmonary veins, as well as the large pulmonary arteries, and to derive a new method for connecting an arterial and venous tree into a single model.

The outline of the thesis is as follows.

Chapter 1 **Introduction.** This introduction.

Chapter 2 **The Systemic Arterial Model.** Gives a more detailed overview of the model of Olufsen, upon which much of the work in this thesis is based.

Chapter 3 **Applications of the Systemic Arterial Model.** Describes a number of applications and adaptations of the systemic arterial model, including testing hypotheses of disease, the derivation of new equations for determining pulse pressures and flows in small arteries, and describes the structure and properties of a pulmonary arterial model.

Chapter 4 **Joining an Arterial and Venous tree.** Derives the equations for the new model of a connected arterial and venous system.

Chapter 5 **The Pulmonary Circulation Model.** Completes the description of the pulmonary system, including the structure and properties of the pulmonary veins.

Chapter 6 **Validation and Applications of the Pulmonary Circulation Model.** Defines the 'normal' conditions of the pulmonary circulation model, and describes its application to hypotheses of disease.

Chapter 7 **Conclusions and Discussion.** Outlines the achievements of the models in this thesis, as well as some of their limitations and potential improvements.

Appendix A **Lax-Wendroff Scheme.** Gives an overview of the equations of the numerical finite difference scheme used to solve the nonlinear equations in the large vessels.

Appendix B **Generations and Orders in Branching Trees.** Gives a brief explanation of the terms 'generation' and 'order' when referring to vascular trees, and describes popular methods of assigning orders.

Chapter 2

The Systemic Arterial Model

In 2000, Mette Olufsen et al. [34] produced a simple, but effective, model for blood flow in the arteries of the systemic circulation using one-dimensional equations derived from the axisymmetric Navier-Stokes equations for incompressible flow in compliant vessels. The model consists of two parts: the large arteries, simulated in detail as a binary tree of compliant, tapering vessels that mimic the actual geometry (lengths and diameters) of the human arterial tree, and the small arteries, modelled as binary asymmetric structured trees at the terminals of the large arteries for which the frequency-dependent input admittance can be calculated analytically. The vessels of the structured trees representing the small peripheral beds of arteries are modelled as straight segments of compliant vessel and, unlike the large arteries, do not mimic the actual geometries of the vessels in the human arterial tree, but are based on general statistical relationships which are estimated from literature data.

2.1 Large Arteries

Blood flow and pressure in the large arteries are predicted from a non-linear one-dimensional model, based on the incompressible Navier–Stokes equations for a Newtonian fluid in a tapering elastic vessel. The inflow boundary condition is based on a velocity profile measured in the ascending aorta, while the outflow condition is predicted from a dynamic impedance applied at all terminals of the large arteries. [35]

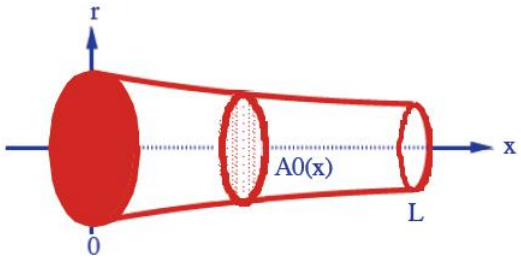

Figure 2.1: Depiction of a tapering large artery [32].

Geometric Properties

As mentioned previously, the large arteries are modelled as a bifurcating tree in which individual vessels are considered to taper along their length. Also, at each bifurcation the radius at the bottom of the parent vessel is larger than the radius at the top of either of the daughter vessels, however, the sum of the cross-sectional area of the two daughter vessels is greater than the area of the parent vessel, meaning that the total cross-sectional area increases at each bifurcation. Further, the tapering of the individual undistended vessels follows an exponential curve of the form

$$r(x) = r_{\text{top}}\exp(-kx), \tag{2.1}$$

where $k = \log(r_{\text{bot}}/r_{\text{top}})/L$ is the tapering factor, r_{top} and r_{bot} are the radii at the top (proximal) and bottom (distal) ends of the vessel respectively, L is the length of the vessel and x is the location along the artery. Thus, to describe the geometry of the large arteries, the proximal ($x = 0$) and distal ($x = L$) radius, and the length of each vessel is required.

Structural Properties

The volume compliance of the arterial wall can be approximated as

$$C = \frac{dV}{dp} \approx \frac{3A_0L}{2}\frac{r_0}{Eh}, \tag{2.2}$$

where V is the volume of the given segment, p is the pressure, r_0 is the equilibrium radius, $A_0 = \pi r_0^2$ is the cross-sectional area, L is the length of the artery, E is Young's modulus, and h is the wall thickness. Thus, elastic properties of the vessels can be described from estimates of Young's modulus, the radius and the wall thickness in the relation Eh/r_0, which is plotted as a function of r_0 in Figure 2.2, using data from Stergiopulos et al. [48]

Using a least squares fit, a curve of the form

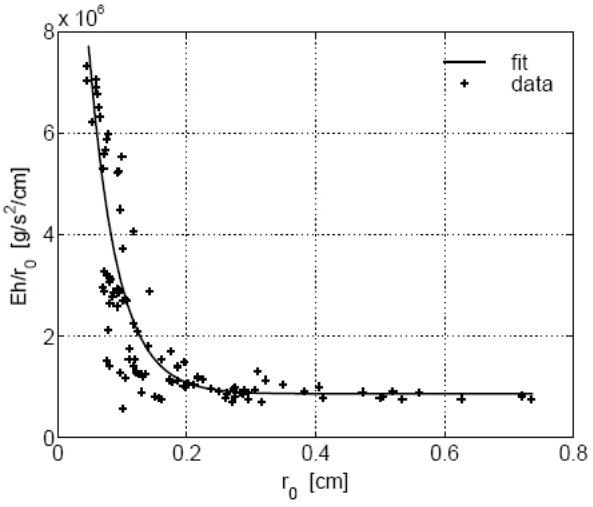

Figure 2.2: Plot of Eh/r_0 as a function of r_0 [33].

$$\frac{Eh}{r_0} = k_1 \exp(k_2 r_0) + k_3 \tag{2.3}$$

has been fitted to the elastic data. The parameters for this are $k_1 = 2.00 \times 10^7 \mathrm{g/(s^2 cm)}$, $k_2 = -22.53 \mathrm{cm}^{-1}$, and $k_3 = 8.65 \times 10^5 \mathrm{g/(s^2 cm)}$.

Fluid Dynamics

A one dimensional model can be built using three equations describing the motion of the fluid in a given vessel in the longitudinal direction, the motion of the vessel walls, and the interaction between the fluid and the walls. These three equations are the Navier–Stokes equations (which describe pressure and flow of the fluid), a continuity equation that ensures what flows in flows out, and a state equation which relates the fluid influence of the vessel walls to the elastic properties.

In order to reduce the three-dimensional problem to a one-dimensional one, further assumptions must be made. First, it is assumed that all vessels have circular cross-section, and that the flow is axisymmetric, eliminating the third dimension from the model. Secondly, the velocity profile is assumed to be flat with a narrow boundary layer providing some friction to the system. Knowing the velocity profile allows integration over the cross-sectional area, removing the second dimension from the model. As a result a one-dimensional model is obtained.

A full derivation of the equations used in this model can be found in [35], and will only

be stated here. These are the momentum equation,

$$\frac{\partial q}{\partial t} + \frac{\partial}{\partial x}\left(\frac{q^2}{A}\right) + \frac{A}{\rho}\frac{\partial p}{\partial x} = \frac{2\pi\nu R}{\delta}\frac{q}{A}, \tag{2.4}$$

the continuity equation,

$$\frac{\partial q}{\partial x} + \frac{\partial A}{\partial t} = 0, \tag{2.5}$$

and the state equation,

$$p(x,t) - p_0 = \frac{4}{3}\frac{Eh}{r_0}\left(1 - \sqrt{\frac{A_0}{A}}\right), \tag{2.6}$$

where q is flow, A is cross-sectional area, ρ is the density of the fluid, p is the pressure, ν is kinematic viscosity, δ is boundary layer thickness, R is the radius of the given vessel, p_0 is external pressure, Eh/r_0 is described above, x is distance along the vessel in the longitudinal direction, and t is time.

Flow and Pressure

The equations above describe flow and pressure in a single vessel segment, and so appropriate boundary equations are required to extend this model to describe the arterial tree.

Firstly, an inflow condition is required, describing the periodic flow into the aorta, i.e. cardiac output at the aortic valve, as shown on the left in Figure 2.3. Second, conditions are required describing flow and pressure across each bifurcation - these are conserved flow $q_p = q_{d_1} + q_{d_2}$ and continuous pressure $p_p = p_{d_1} = p_{d_2}$, where the subscripts p, d_1 and d_2 refer to the parent and first and second daughter vessels of the bifurcation, as in the right picture in Figure 2.3.

Finally, an outflow condition is required at the terminals of the large arteries. Here a frequency dependent impedance, $Z(x,\omega)$, related to flow and pressure by,

$$P(x,\omega) = Z(x,\omega)Q(x,\omega),$$

and determined from the model for the small arteries, is applied.

Since the inflow is periodic, it is assumed that flow and pressure can be expressed using a complex periodic Fourier series. So let

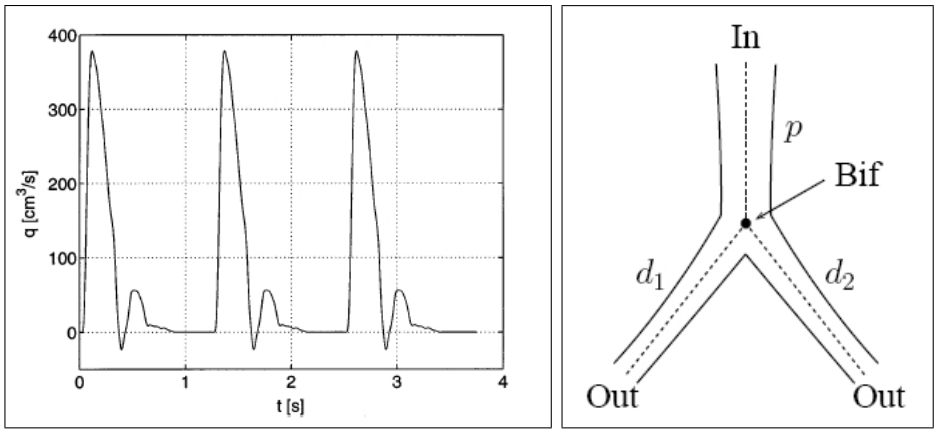

Figure 2.3: Left: Inflow as a function of time, Right: A single bifurcation [33], [35].

$$p(x,t) = \sum_{k=-\infty}^{\infty} P(x,\omega_t)e^{i\omega_k t} \quad \text{and} \quad q(x,t) = \sum_{k=-\infty}^{\infty} Q(x,\omega_t)e^{i\omega_k t},$$

where $\omega_k = 2\pi k/T$ is the angular frequency, and

$$P(x,\omega_k) = \frac{1}{T}\int_{-T/2}^{T/2} p(x,t)e^{i\omega_k t} \quad \text{and} \quad Q(x,\omega_k) = \frac{1}{T}\int_{-T/2}^{T/2} q(x,t)e^{i\omega_k t}.$$

By inverse Fourier transform, $Z(x,\omega)$ can be transformed to obtain $z(x,t)$, and by convolution theorem it is possible to find an analytic relation between p and q:

$$p(x,t) = \int_{t-\tau}^{t} q(x,\tau)z(x,t-\tau)d\tau, \tag{2.7}$$

which is the outflow condition for the large arteries.

2.2 Small Arteries

The purpose of the model of the small arteries is to determine an impedance to apply as the outflow condition to the more detailed model of the large arteries. Blood flow and pressure in the small arteries are predicted from a linear one-dimensional viscous model (a wave equation) which is derived from linearisation of the incompressible axisymmetric Navier-Stokes equations for Newtonian fluid in a non-tapering elastic vessel.

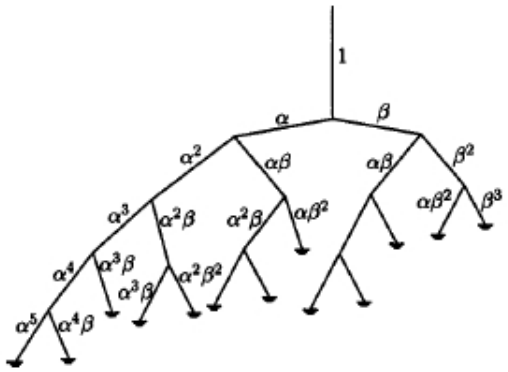

Figure 2.4: Structured tree description of the small arteries [34].

Structure

The small arteries are modelled as a binary asymmetric structured tree, as shown in Figure 2.4. At each bifurcation the radii of the left and right daughter vessels are scaled by a factor α and β, respectively, with respect to the parent vessel. Because each branch is terminated when the radius is less than some pre-described minimum radius, the tree does not have a fixed number of generations.

The branching nature of the structured tree is governed by a number of relations. There is a relation describing how radius changes over an arterial bifurcation, a power law based on the principle of minimum work, given by,

$$r_p^{\xi} = r_{d_1}^{\xi} + r_{d_2}^{\xi},$$

where $2.33 < \xi < 3.00$, since $\xi \geq 3.00$ corresponds to laminar flow, and $\xi \leq 2.33$ corresponds to turbulent flow [52].

There are also relations describing the asymmetry of the tree (ratio of left daughter radius to right daughter radius), and an area ratio (ratio of total cross-sectional area of the two daughter vessels to area of parent vessel). These ratios are, respectively,

$$\gamma = r_{d_1}/r_{d_2} \quad \text{and} \quad \eta = \frac{r_{d_1}^2 + r_{d_2}^2}{r_p^2} = \frac{1+\gamma}{(1+\gamma^{\xi/2})^{2/\xi}}.$$

From these three relations for ξ, γ, and η, it is possible to determine the two scaling relations α and β described in Figure 2.4,

$$\alpha = r_{d_1}/r_p = (1+\gamma^{\xi/2})^{-1/\xi} \quad \text{and} \quad \beta = r_{d_2}/r_p = \alpha\sqrt{\gamma}.$$

From literature [32], it is possible to find values for the radius exponent of $\xi = 2.76$, and area ratio $\eta = 1.16$, yielding an asymmetry ratio of $\gamma = 0.41$, and scaling ratios of $\alpha = 0.9$ and $\beta = 0.6$.

The vessels of the structured tree are scaled until a pre-determined minimum radius r_{min} (0.010cm for the systemic arteries) is reached, at which point the tree is terminated. Also, the length of each segment in the structured tree is determined from the radius by a length to diameter ratio, estimated from literature [32] to be $L/d \approx 25 \pm 5$.

Fluid Dynamics

Unlike the large vessels, the small arteries do not taper, and for computational feasibility a linear model is used. Again, only a brief description of the model will be given here - a more detailed description can be found in [35].

From the one-dimensional axisymmetric Navier–Stokes equations, the linear momentum equation is,

$$\frac{\partial u_x}{\partial t} + \frac{1}{\rho}\frac{\partial p}{\partial x} = \frac{\nu}{r}\frac{\partial}{\partial r}\left(r\frac{\partial u_x}{\partial r}\right), \tag{2.8}$$

where u_x is longitudinal flow velocity, and the other terms are as defined previously. Taking Fourier expansions of velocity and pressure, $u_x(r,x,t) = U_x(r,x)e^{i\omega t}$ and $p(x,t) = P(x)e^{i\omega t}$ and substituting into (2.8), yields,

$$i\omega U_x + \frac{1}{\rho}\frac{\partial P}{\partial x} = \frac{\nu}{r}\frac{\partial}{\partial r}\left(r\frac{\partial u_x}{\partial r}\right). \tag{2.9}$$

Since the vessels do not taper, the solution to (2.9) is,

$$U_x = \frac{1}{i\omega\rho}\frac{\partial P}{\partial x}\left(1 - \frac{J_0(rw_0/r_0)}{J_0(w_0)}\right),$$

where ${w_0}^2 = i^3 w^2$, and $w^2 = {r_0}^2\omega/\nu$ is the squared Womersley number, an J_0 are Bessel functions.

Cross-sectionally averaged flow $q = Qe^{i\omega t}$ is given by

$$Q = 2\pi\int_0^\infty U_x r dr,$$

giving the momentum equation for the small arteries,

$$i\omega Q = -\frac{A_0}{\rho}\frac{\partial P}{\partial x}\left(1 - F_J\right), \tag{2.10}$$

where $F_J = \frac{2J_1(w_0)}{w_0 J_0(w_0)}$.

As for the large arteries, the continuity equation is

$$\frac{\partial q}{\partial x} + \frac{\partial A}{\partial t} = 0,$$

which can be re-written as,

$$C\frac{\partial p}{\partial t} + \frac{\partial q}{\partial x} = 0,$$

where

$$C = \frac{\partial A}{\partial p} = \frac{3A_0 r_0}{2Eh}\left(1 - \frac{3pr_0}{4EH}\right)^{-3} \approx \frac{3A_0 r_0}{2Eh}$$

is the state equation, approximated from linearising the state equation for the large arteries. Taking Fourier expansions again gives the continuity equation for the small arteries,

$$i\omega CP + \frac{\partial Q}{\partial x} = 0. \tag{2.11}$$

Solutions to the Linear Model

Differentiating the continuity equation (2.11) with respect to x, and substituting into the momentum equation (2.10), gives wave equations in flow Q and pressure P,

$$\frac{\omega^2}{c^2}Q + \frac{\partial^2 Q}{\partial x^2} = 0, \text{ or } \frac{\omega^2}{c^2}P + \frac{\partial^2 P}{\partial x^2} = 0, \tag{2.12}$$

with wave propagation velocity $c = \sqrt{\frac{A_0(1-F_J)}{\rho C}}$.

Solving (2.12) gives,

$$Q(x,\omega) = a\cos(\omega x/c) + b\sin(\omega x/c), \text{ and} \tag{2.13}$$

$$P(x,\omega) = i\sqrt{\frac{\rho}{CA_0(1-F_J)}}(-a\cos(\omega x/c) + b\sin(\omega x/c)), \tag{2.14}$$

where a and b are integration constants.

Determining root impedance

Since $P(x,\omega) = Z(x,\omega)Q(x,\omega)$, and writing $g = cC = \sqrt{CA_0(1-F_J)/\rho}$, then from (2.13) and (2.14),

$$Z(x,\omega) = \frac{ig^{-1}(b\cos(\omega x/c) - a\sin(\omega x/c))}{a\cos(\omega x/c) + b\sin(\omega x/c)}.$$

At $x = L$, i.e. at the end of a vessel segment,

$$Z(L,\omega) = \frac{ig^{-1}(b\cos(\omega L/c) - a\sin(\omega L/c))}{a\cos(\omega L/c) + b\sin(\omega L/c)},$$

and at $x = 0$, i.e. the root of a vessel segment,

$$Z(0,\omega) = \frac{i}{g}\frac{b}{a}.$$

So, assuming $Z(L,\omega)$ is known,

$$\frac{b}{a} = \frac{\sin(\omega L/c) - igZ(L,\omega)\cos(\omega L/c)}{\cos(\omega L/c) + igZ(L,\omega)\sin(\omega L/c)},$$

and so the root impedance for any vessel, in terms of its terminal impedance, can be found,

$$Z(0,\omega) = \frac{ig^{-1}\sin(\omega L/c) + Z(L,\omega)\cos(\omega L/c)}{\cos(\omega L/c) + igZ(L,\omega)\sin(\omega L/c)}. \tag{2.15}$$

Also, for any vessel the input impedance for zero frequency is,

$$Z(0,0) = \lim_{\omega\to 0} Z(0,\omega) = \frac{8\mu l_{rr}}{\pi r_0^3} + Z(L,0), \tag{2.16}$$

where l_{rr} is the length to radius ratio of the structured tree.

So we have $Z(0,\omega) = f(Z(L,\omega))$, as well as bifurcation conditions $Z_P^{-1} = Z_{d_1}^{-1} + Z_{d_2}^{-1}$, and terminal conditions for the structured tree, Z_{term} (set to be zero) and r_{min}. This is enough information to determine the impedance at the root of the structured tree, and hence provide an outflow condition to the model.

2.3 Computing Flows and Pressures

The arterial vessel network used in the systemic arterial model is described in Figure 2.5, with vessel dimensions summarised in Table 2.1. The inflow profile representing cardiac output, as described in Figure 2.3, is attached to the start of vessel 1, and structured tree outflow conditions are attached to each of the terminal large arteries, represented by the areas shaded grey.

The length, top and bottom radius of each of the numbered vessels are specified, and the bottom radius of each terminal vessel is also the root radius of its attached structured tree. Equations (2.4) and (2.5) are then solved numerically at a spatial resolution of 4 points per cm, and a temporal resolution of 8192 points per period to find the flow and, through (2.6), the pressure profiles in these vessels.

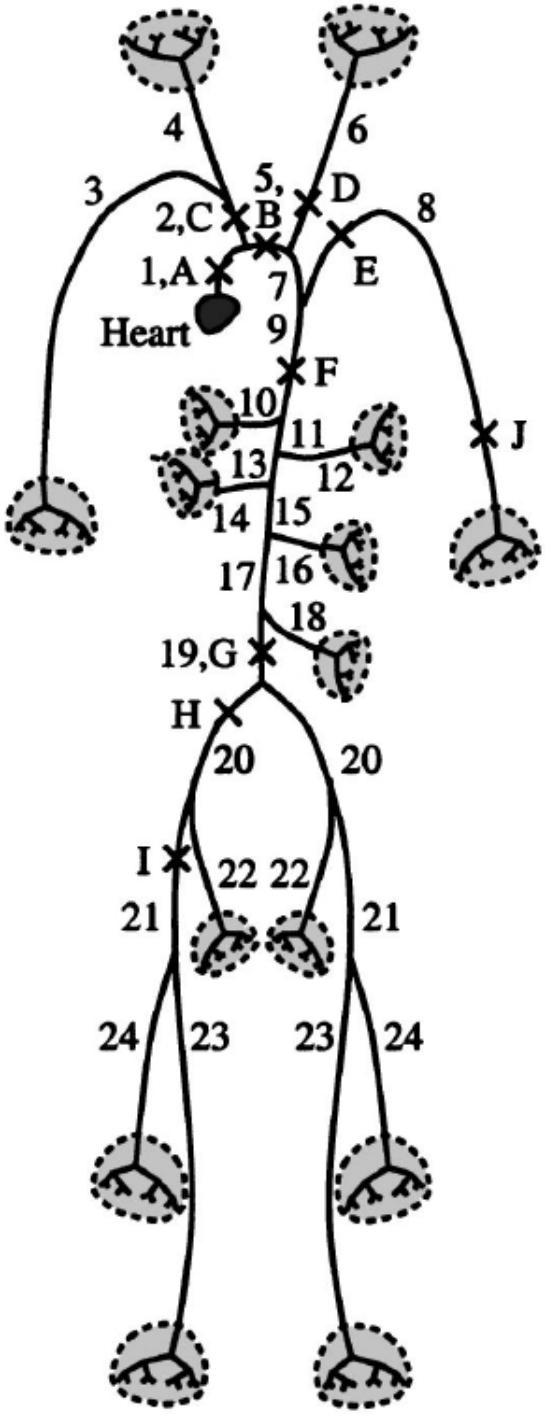

Figure 2.5: Arterial vessel network used in the systemic arterial model [34].

No.	Name	Inlet diameter (cm)	Outlet diameter (cm)	Length (cm)
1	Ascending aorta	1.250	1.140	7.000
5	Aortic arch	1.140	1.110	1.800
7	Aortic arch	1.110	1.090	1.000
9	Thoracic aorta	1.090	0.850	18.800
11	Abdominal aorta	0.850	0.830	2.000
13	Abdominal aorta	0.830	0.800	2.000
15	Abdominal aorta	0.800	0.790	1.000
17	Abdominal aorta	0.790	0.730	6.000
19	Abdominal aorta	0.730	0.700	3.000
20	External iliac	0.450	0.430	6.500
21	Femoral	0.430	0.400	13.000
24	Femoral	0.400	0.300	44.000
22	Internal iliac	0.200	0.200	4.500
23	Deep femoral	0.200	0.200	11.000
2	Anonyma	0.700	0.700	3.500
3, 8	Subcl. and brach.	0.440	0.280	43.000
4	R. com. carotid	0.290	0.280	17.000
6	L. com. carotid	0.290	0.280	19.000
10	Celiac axis	0.330	0.300	3.000
12	Sup. mesenteric	0.330	0.330	5.000
14, 16	Renal	0.280	0.250	3.000
18	Inf. mesenteric	0.200	0.180	4.000

Table 2.1: Dimensions of the large vessels of the Systemic arterial model [32].

Numerical Solutions

In order to solve numerically for flow and pressure in the large arteries, using the two-step Lax-Wendroff method [57], we introduce the function,

$$B(r_0(x), p(x,t)) = \frac{1}{\rho}\int_{p_0}^{p(x,t)} A[r_0(x), p']dp' \tag{2.17}$$

$$\Rightarrow \frac{\partial B}{\partial x} = \frac{A}{\rho}\frac{\partial p}{\partial x} + \frac{\partial B}{\partial r_0}\frac{dr_0}{dx}. \tag{2.18}$$

The last term of this can be evaluated explicitly, and so can be added to both sides of the momentum equation (2.4) to give,

$$\frac{\partial q}{\partial t} + \frac{\partial}{\partial x}\left(\frac{q^2}{A} + B\right) = -\frac{2\pi\nu qR}{\delta A} + \frac{\partial B}{\partial r_0}\frac{dr_0}{dx}. \tag{2.19}$$

This allows us to write (2.4) and (2.5) in conservation form as,

$$\frac{\partial}{\partial t}\mathbf{U} + \frac{\partial}{\partial x}\mathbf{R} = \mathbf{S}, \tag{2.20}$$

with dependent variables,

$$\mathbf{U} = \begin{pmatrix} A \\ q \end{pmatrix},$$

system flux,

$$\mathbf{R} = \begin{pmatrix} q \\ \frac{q^2}{A} + B \end{pmatrix},$$

and right hand side,

$$\mathbf{S} = \begin{pmatrix} 0 \\ \frac{-2\pi r_0}{\delta\mathcal{R}}\frac{q}{A} + \left(2\sqrt{A}\left(\sqrt{\pi}f + \sqrt{A_0}\frac{df}{dr_0}\right)\frac{dr_0}{dx}\right) \end{pmatrix}.$$

With the inflow and bifurcation conditions described in Figure 2.3, and the outflow condition given by (2.7) we have inflow and outflow boundary conditions for each of the large arteries in Figure 2.5 meaning we can solve numerically for flow and pressure in each of these arteries. More details of how we do this numerically can be found in [32] and Appendix A.

Chapter 3

Applications of the Systemic Arterial Model

By means of a number of fairly straightforward adaptations, we have extended Olufsen's systemic model to apply to various physiological scenarios. While the results of these are interesting in their own right, they also provide a useful precursor to the more detailed pulmonary model that we will develop later.

The scenarios that we have looked at are,

- **Arterial compliance and hypertension** - we will later use a similar approach to describe Pulmonary Arterial Hypertension and Chronic Thromboembolic Pulmonary Hypertension.
- **Microcirculatory rarefaction and hypertension** - we will later use a similar approach to describe Pulmonary Hypertension in association with hypoxic lung disease.
- **Pulse Pressure in Small Arteries** - some of the equations used in determining these pressures will later be used when developing the model to describe a joined up arterial and venous network.
- **A Pulmonary Arterial Model** - a simple description of the Pulmonary arteries, providing a basis upon which to build our more detailed model of the entire Pulmonary circulation.

3.1 Arterial compliance and hypertension

Since peak, trough and pulse pressures are related to the physical properties of elastic arteries, much attention has been paid to arterial stiffness and its relation to hypertension and other cardiovascular risk factors [29]. In this section, we investigate this relationship by modelling changes in arterial stiffness and observing the resulting effect on the predicted pressure and flow waveforms in each of the proximal and distal aorta, and radial artery.

In Olufsen's systemic model, arterial compliance is controlled by estimates of Young's modulus E, vessel wall thickness h, and undistended radius r_0, in the parameter Eh/r_0 (see equations (2.3) and (2.6)). By increasing (or decreasing) the value of this parameter, we can model the effects of increased (or decreased) arterial stiffness.

A further advantage of Olufsen's model is that the separate descriptions for large and small arteries allows for parameters to be varied independently in each of the large and small arteries. This means that we can model three different instances of arterial compliance changes - changes in small arterial compliance only, changes in large vessel compliance only, and uniform compliance changes in both large and small arteries.

Results

Figures 3.1 and 3.2 show the effects of compliance changes in the small arteries only on pressure and flow respectively in the proximal aorta. The percentage value refers to the percentage change in the stiffness parameter Eh/r_0 away from the values established by Figure 2.2 and equation (2.3) in Section 2.1, 'Mean' refers to the average value over a period, 'Peak' and 'Trough' are the maximum and minimum values over a period respectively, and 'Pulse' is the difference between 'Peak' and 'Trough'.

Little effect is seen on peak and mean pressures, however a slight drop in trough pressure (and resulting increase in pulse pressure) is seen in instances of stiffer small arteries.

Little or no effect can be seen in the flow profiles for the proximal and distal aorta, although slight earlier and higher peaking of the flow wave in the radial artery can be seen in instances of the most compliant small arteries.

Figures 3.3 and 3.4 show the effects of compliance changes in the large arteries only, and Figures 3.5 and 3.6 show the effects of uniform compliance changes in both the large and small arteries. In both these cases, significant increases in peak and pulse pressures can be seen with increasing arterial stiffness. Further, in both the flow and pressure profiles of the more distal vessels (the distal aorta and the radial artery), we see earlier peaking of the incident and reflected components of the waveforms (the first and second peaks respectively, most obvious in the distal aorta flow plot of Figure 3.6) as a result of the increased wave speed due to stiffer vessels.

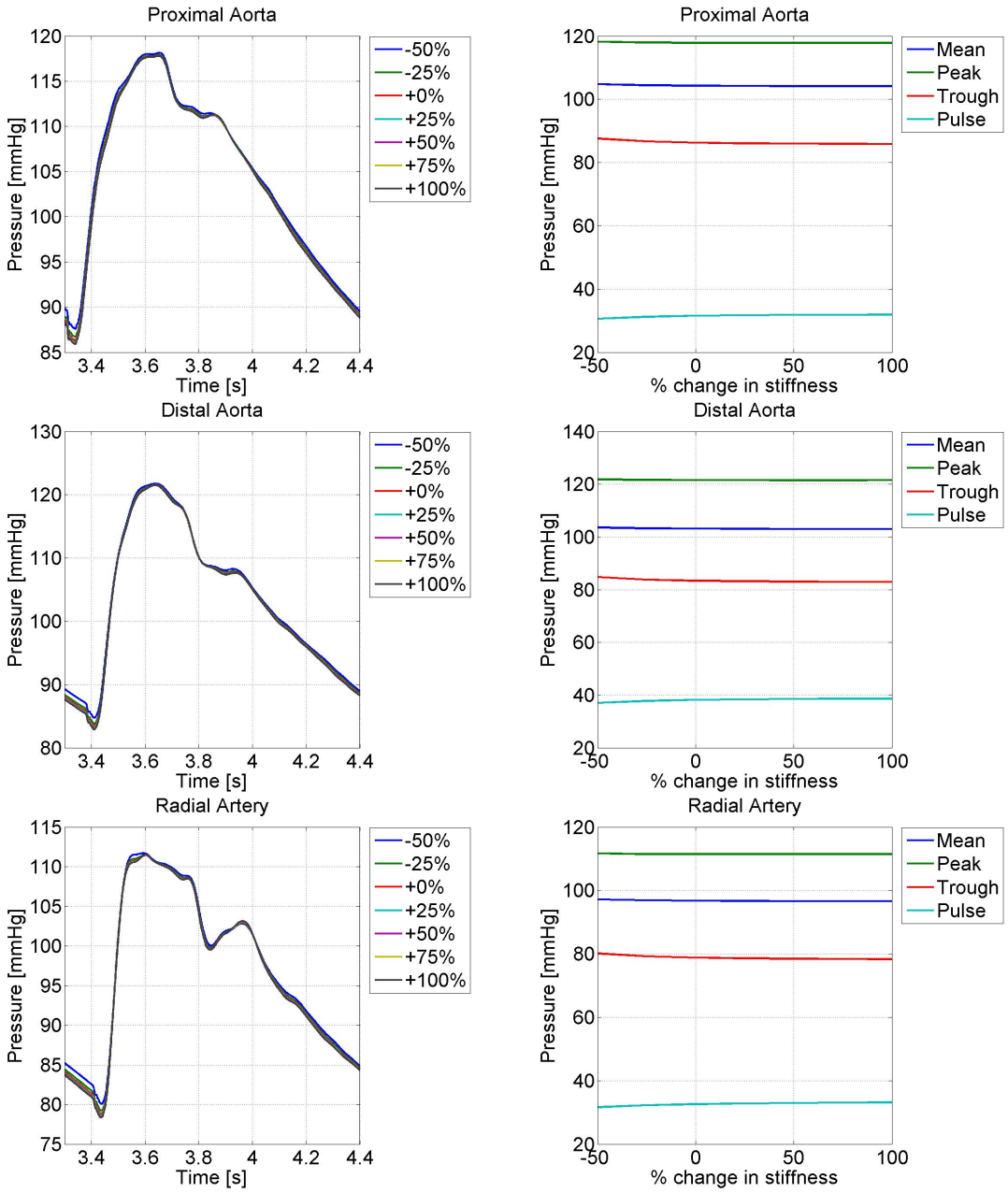

Figure 3.1: Effects of changing small vessel compliance on pressure.

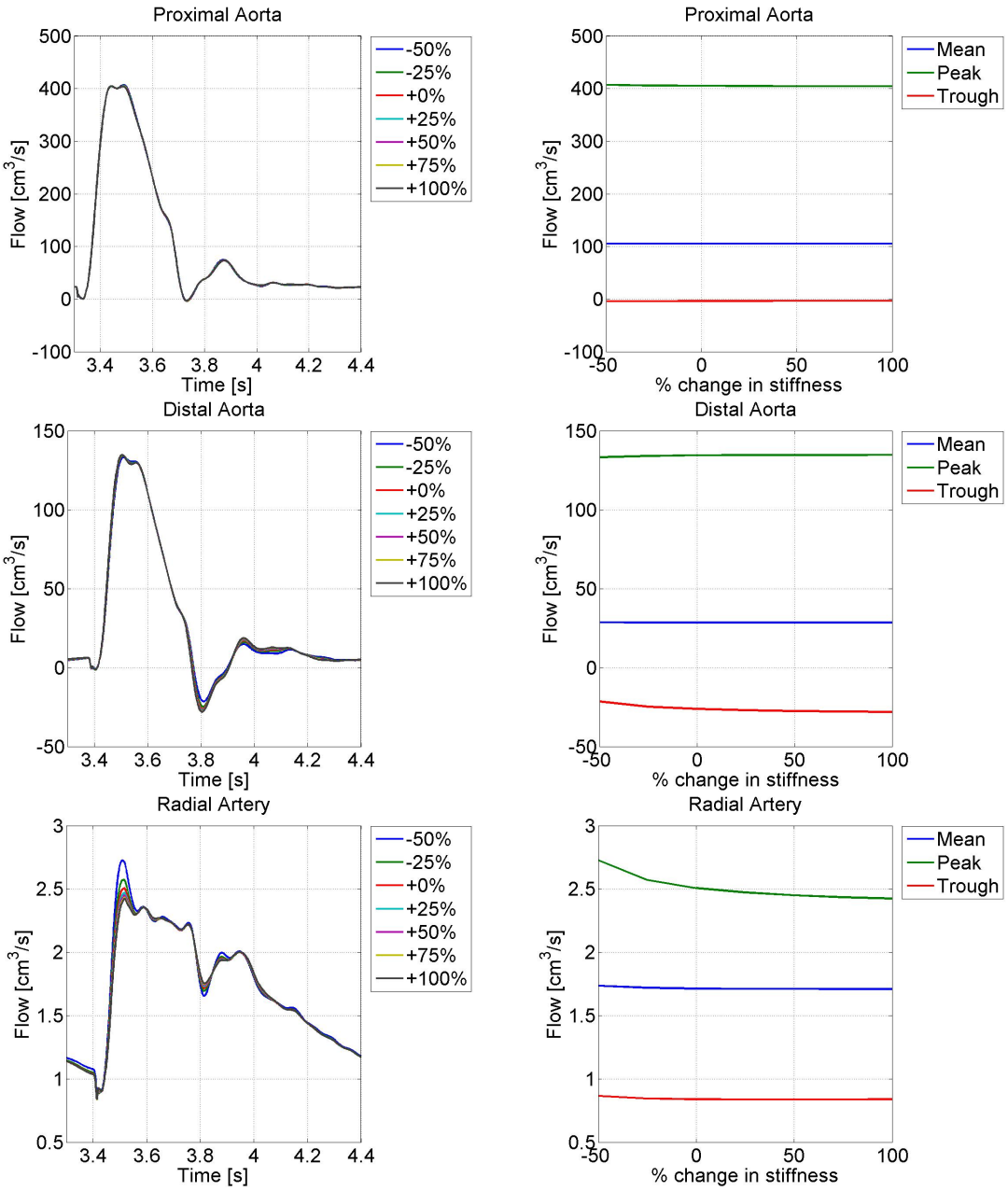

Figure 3.2: Effects of changing small vessel compliance on flow.

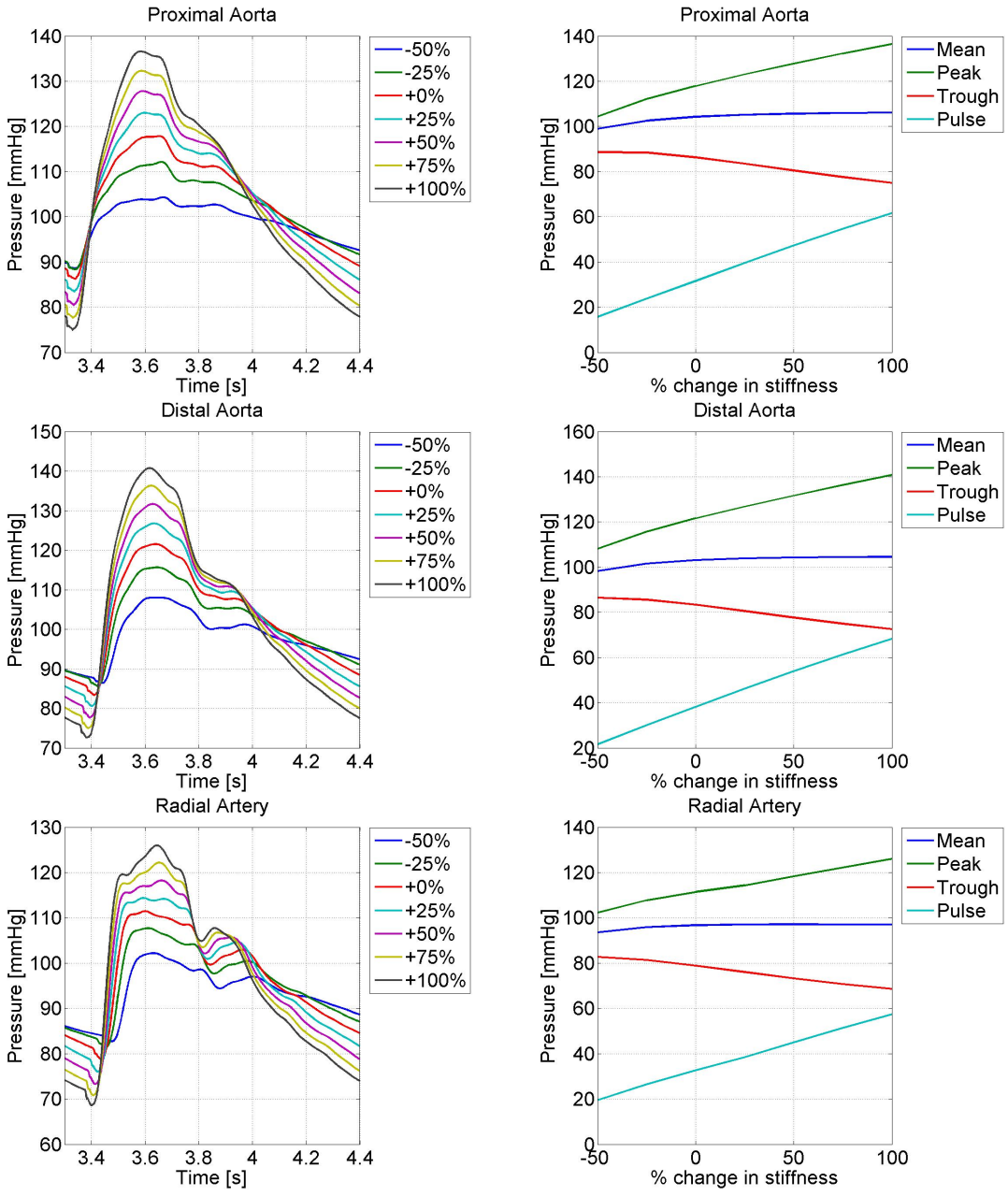

Figure 3.3: Effects of changing large vessel compliance on pressure.

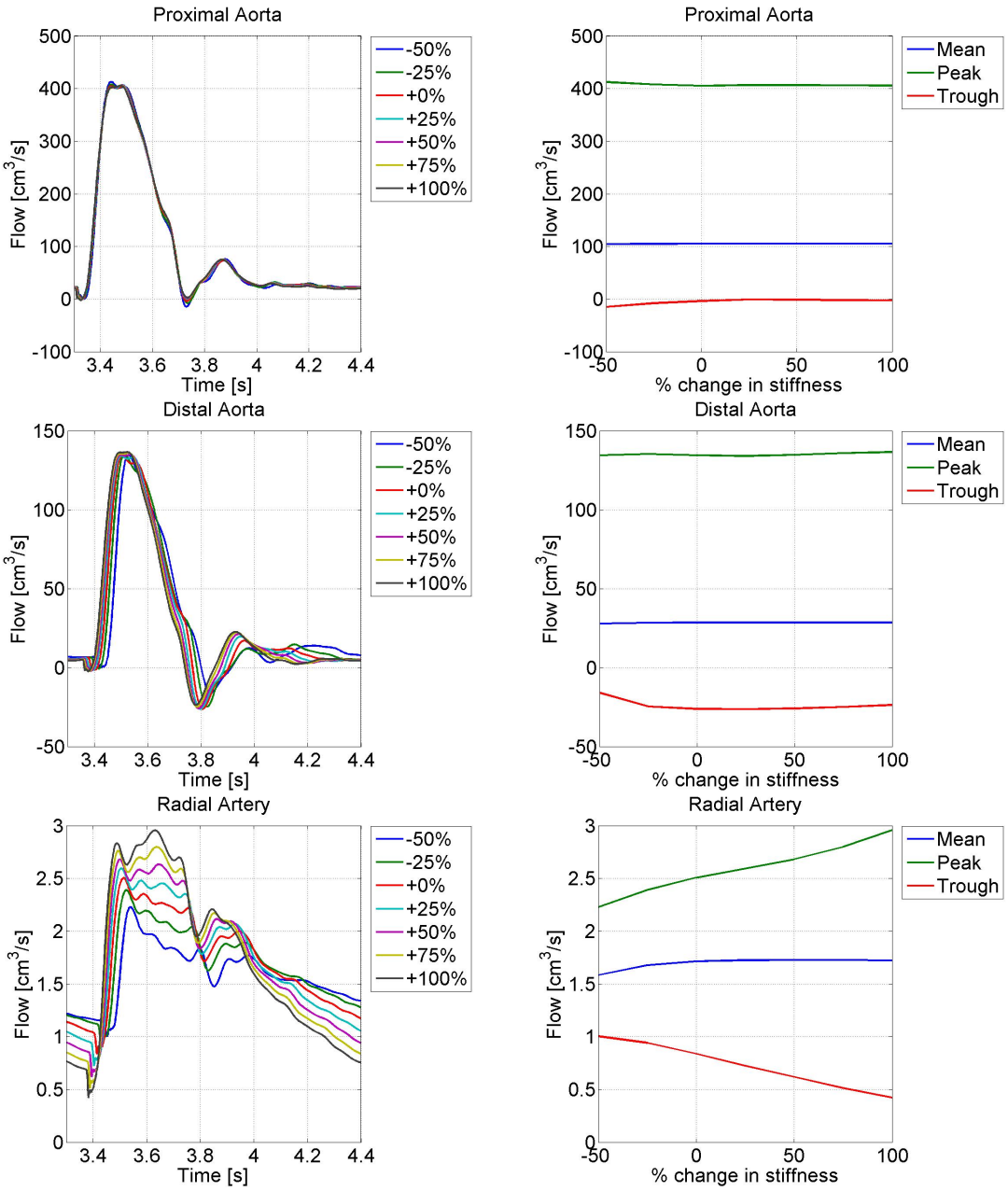

Figure 3.4: Effects of changing large vessel compliance on flow.

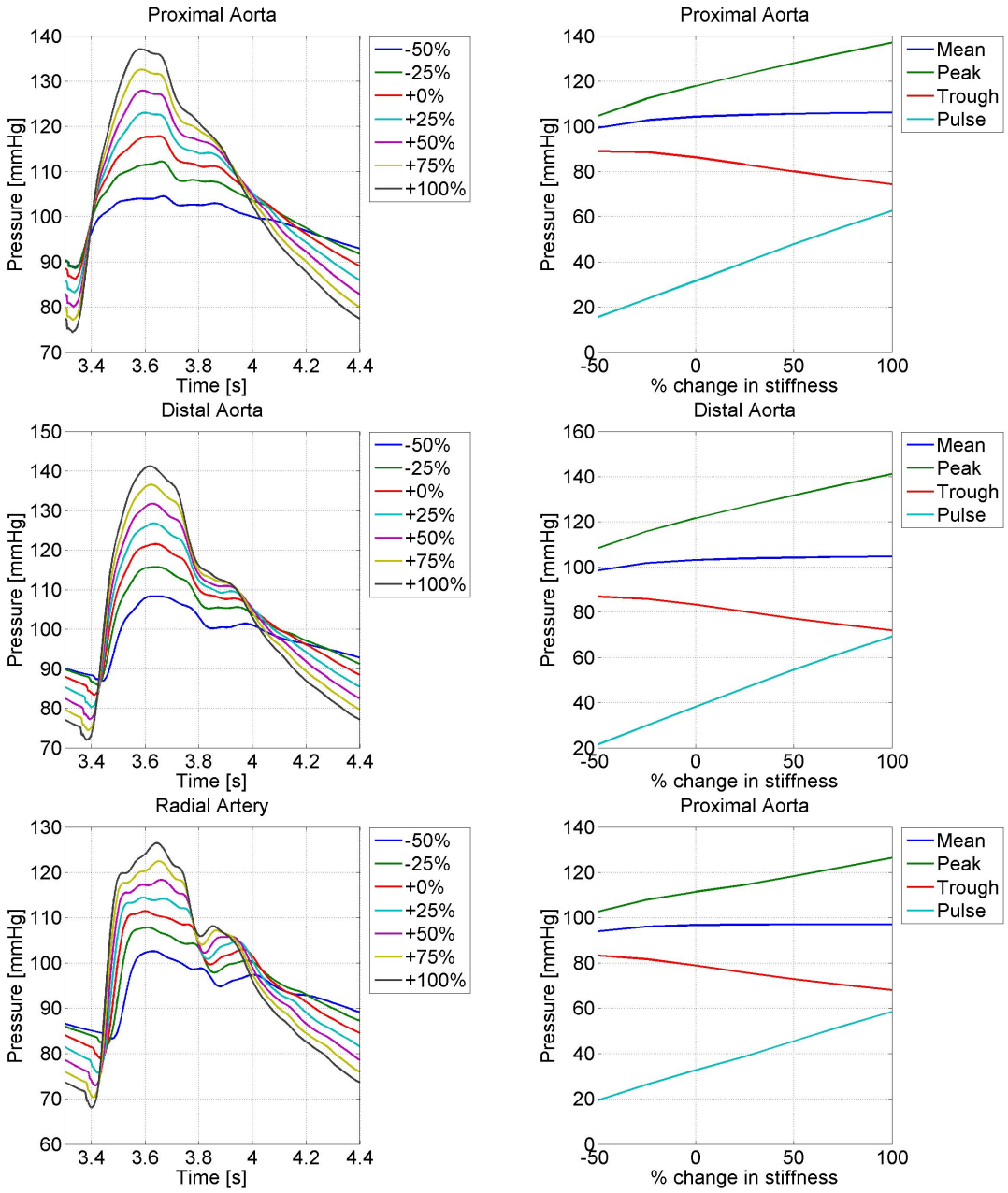

Figure 3.5: Effects of changing both large and small vessel compliance on pressure.

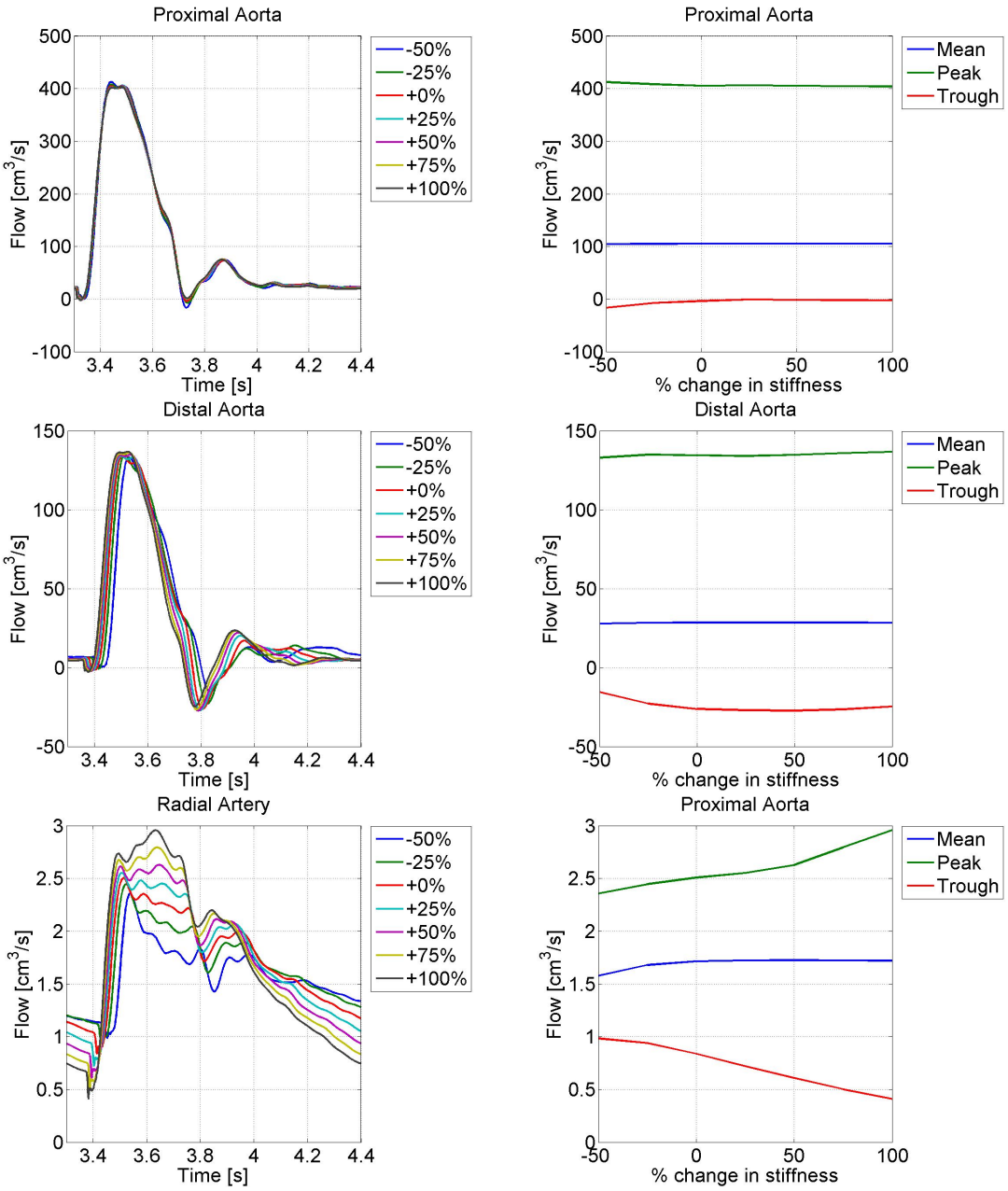

Figure 3.6: Effects of changing both large and small vessel compliance on flow.

Interpreting these results

The similarity of the effects seen by changing large vessel compliance only, and by uniformly changing both large and small vessel compliance, suggest that the effects of stiffening the large vessels far outweigh the effects of stiffening the small vessels. This agrees with the findings of Azer and Peskin [3], who performed a similar brief investigation on a different implementation of the same base model.

Further, our results support Azer and Peskin's conclusion that stiffening of the large arteries results in pressure increases consistent with observations of isolated systolic hypertension, as occurs in aging [13], [19], [29].

3.2 Microcirculatory rarefaction and hypertension.

The microcirculation can be described as the blood flow through the smallest blood vessels of the circulatory system – arterioles, capillaries and venules of typically less than 100μm diameter [40]. Studies have shown that the pre-capillary drop in blood pressure occurs mostly over vessels of diameter 0.001-0.030cm [28], [41], thus the microcirculation is the site of maximum resistance within the arterial tree, although the precise location and nature of these 'resistance arteries' is not well known [10].

Microcirculatory rarefaction is defined as a reduction of vessels per unit volume within the vascular bed, and may be further classified as structural (an anatomical absence of vessels) or functional (vessels anatomically present but not perfused) [12]. Structural rarefaction has been observed in both skin capillaries, and intramuscular resistance arteries in hypertension. Importantly, it has also been demonstrated in borderline hypertension, and in normotensive young offspring of parents with hypertension, suggesting that microcirculatory rarefaction may be a cause of hypertension rather than the other way around.

Developing the model to include microcirculation and effects of rarefaction.

Olufsen's model describes the small vessels of the circulation as a binary asymmetric structured tree, as described in Section 2.2, where the relationship between parent and daughter vessel radii is characterised by a number of parameters, namely the radius relation,

$$r_p^\xi = r_{d_1}^\xi + r_{d_2}^\xi, \tag{3.1}$$

with exponent $2.33 \leq \xi \leq 3.0$, the asymmetry ratio,

$$\gamma = r_{d_1}/r_{d_2}, \tag{3.2}$$

and the area ratio,

$$\eta = \frac{r_{d_1}^2 + r_{d_2}^2}{r_p^2} = \frac{1+\gamma}{(1+\gamma^{\xi/2})^{2/\xi}}, \tag{3.3}$$

where $\eta > 1$.

Physiological data suggests values of $\xi = 2.76$ and $\eta = 1.16$, implying a value of $\gamma = 0.41$, for normal individuals [32], however in instances of rarefaction there are fewer small calibre blood vessels than normal in a given volume of tissue, and this can be modelled by decreasing the value of the area ratio, η. This is a good model for structural

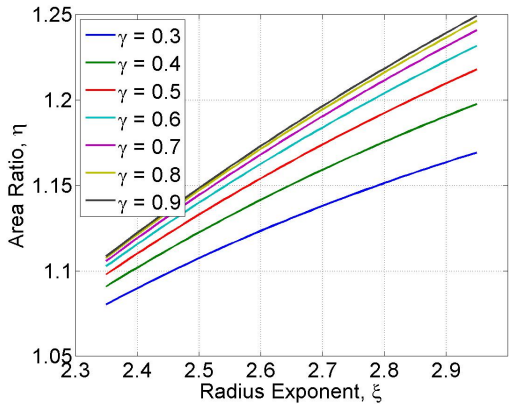

Figure 3.7: Relationship between radius exponent ξ, asymmetry ratio γ and area ratio η.

rarefaction as decreasing η results in there being fewer generations in the structured tree, and vessel radius decreasing in size with generation number more rapidly than would normally occur, mimicking the observed reduction in density of small vessels.

Results - Effects on vessel density

Figure 3.7 shows how the area ratio, η, varies with changing radius exponent ξ for different values of the asymmetry ratio γ. Increasing either ξ or γ results in an increase in η.

Figure 3.8 shows the effect of changing the radius exponent ξ (and thus altering the area ratio η) on the total number of vessels in a structured tree modelled vascular bed. It shows how the vascular bed becomes rarefied (i.e. the total number, and thus density, of vessels is reduced) when the area ratio η is decreased, and also how the vascular bed becomes more dense with increased values of η.

Figure 3.9 shows how many terminal vessels - the smallest calibre vessels - there are in the structured tree, and how this varies with ξ and η. Again, we see that a reduced area ratio results in rarefied trees with fewer small calibre blood vessels.

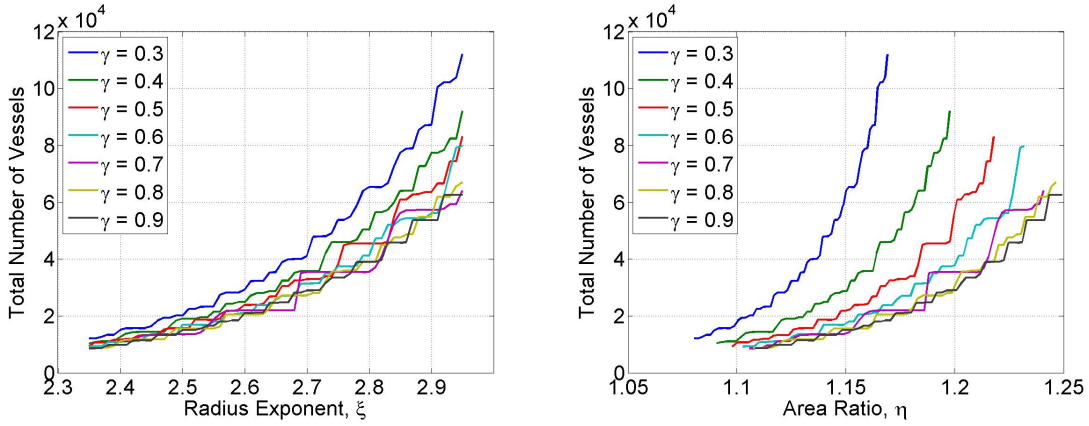

Figure 3.8: Effects of rarefaction on the total number of vessels in a structured tree with root radius $r_{root} = 0.300$cm and minimum radius $r_{min} = 0.010$cm.

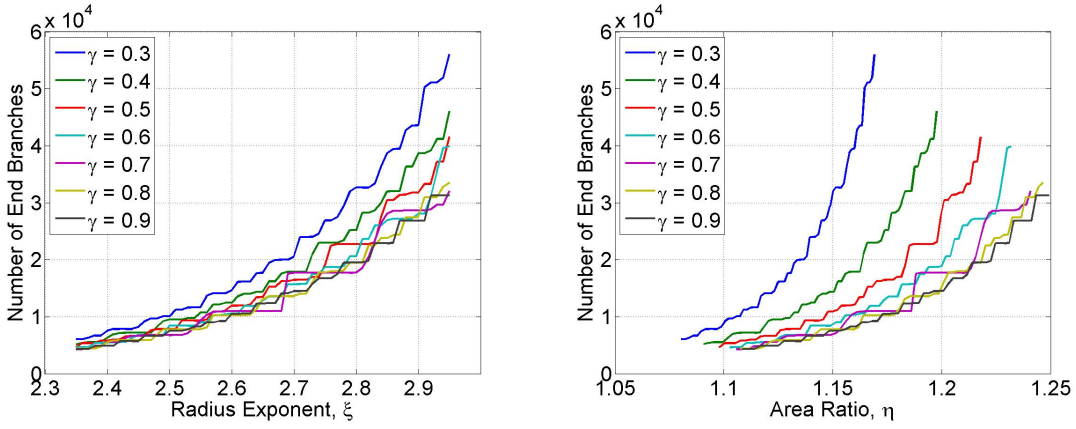

Figure 3.9: Effects of rarefaction on the number of end vessels in a structured tree with root radius $r_{root} = 0.300$cm and minimum radius $r_{min} = 0.010$cm.

Results - Effects on Pressure Pulse

For various degrees of rarefaction, predicted pressure pulse and flow waveforms were generated for the Proximal Aorta (5cm above the aortic valve), Distal Aorta (5cm from the end of the abdominal aorta) and Radial Artery (2cm from the end of the artery).

Figure 3.10 shows the predicted pressure pulse waveforms in the Proximal Aorta. It shows how decreasing the radius exponent and/or asymmetry ratio, and therefore decreasing the area ratio creating rarefied vascular beds, results in shifting the pulse waveform upwards on the pressure scale although little change in the shape of the waveform is observed. This same pattern of shifted waveform is also seen in the predicted pressure pulses of the Distal Aorta (Figure 3.13), and the Radial Artery (Figure 3.16).

The generated flow profiles for each of the Proximal and Distal Aorta, and Radial Artery are shown in Figures 3.11, 3.14 and 3.17 respectively. Almost no change is seen in the flow profile of the Proximal Aorta, while in the Distal Aorta we see small changes in the amplitude and position of the reflected wave component (the later, smaller peak in the flow wave profile) which is smaller and occurs slightly later in rarefied conditions. In the Radial Artery, the amplitude of the flow waveform is notably reduced with rarefaction.

Figures 3.12, 3.15, and 3.18 show the mean pressures and pulse pressures (difference between peak and trough pressure) for the predicted waveforms of the Proximal and Distal Aorta, and Radial Artery. They show how mean pressure increases with increased rarefaction in an almost linear relationship with decreasing radius exponent. Interestingly, however, pulse pressure is seen to decrease in instances of increased rarefaction (and thus increased mean pressure), and further that in the Radial Artery pulse pressure appears to tail off to a maximum of around 33mmHg with increased vessel density.

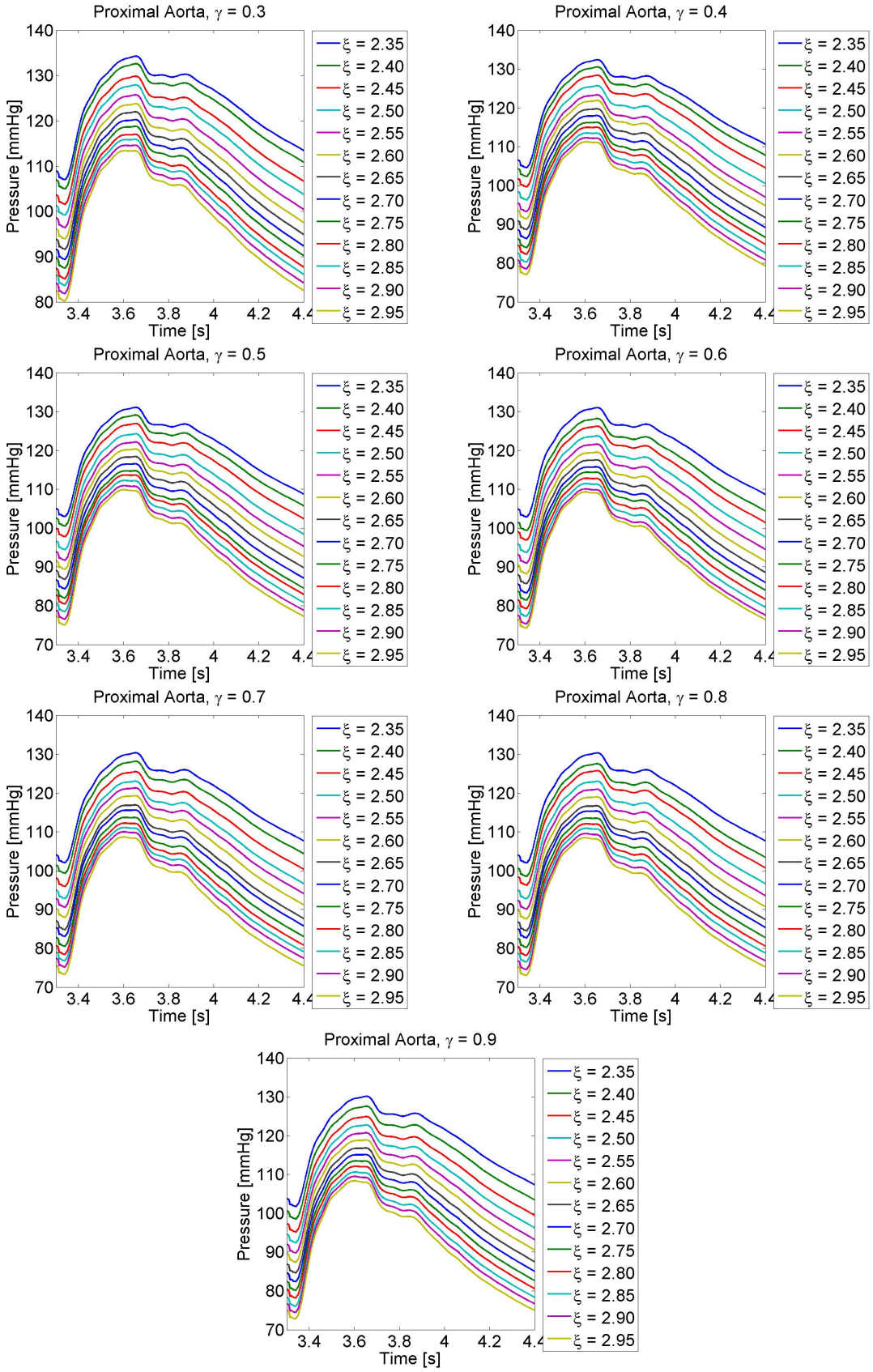

Figure 3.10: Effects of rarefaction on pressure pulse waveform in the Proximal Aorta.

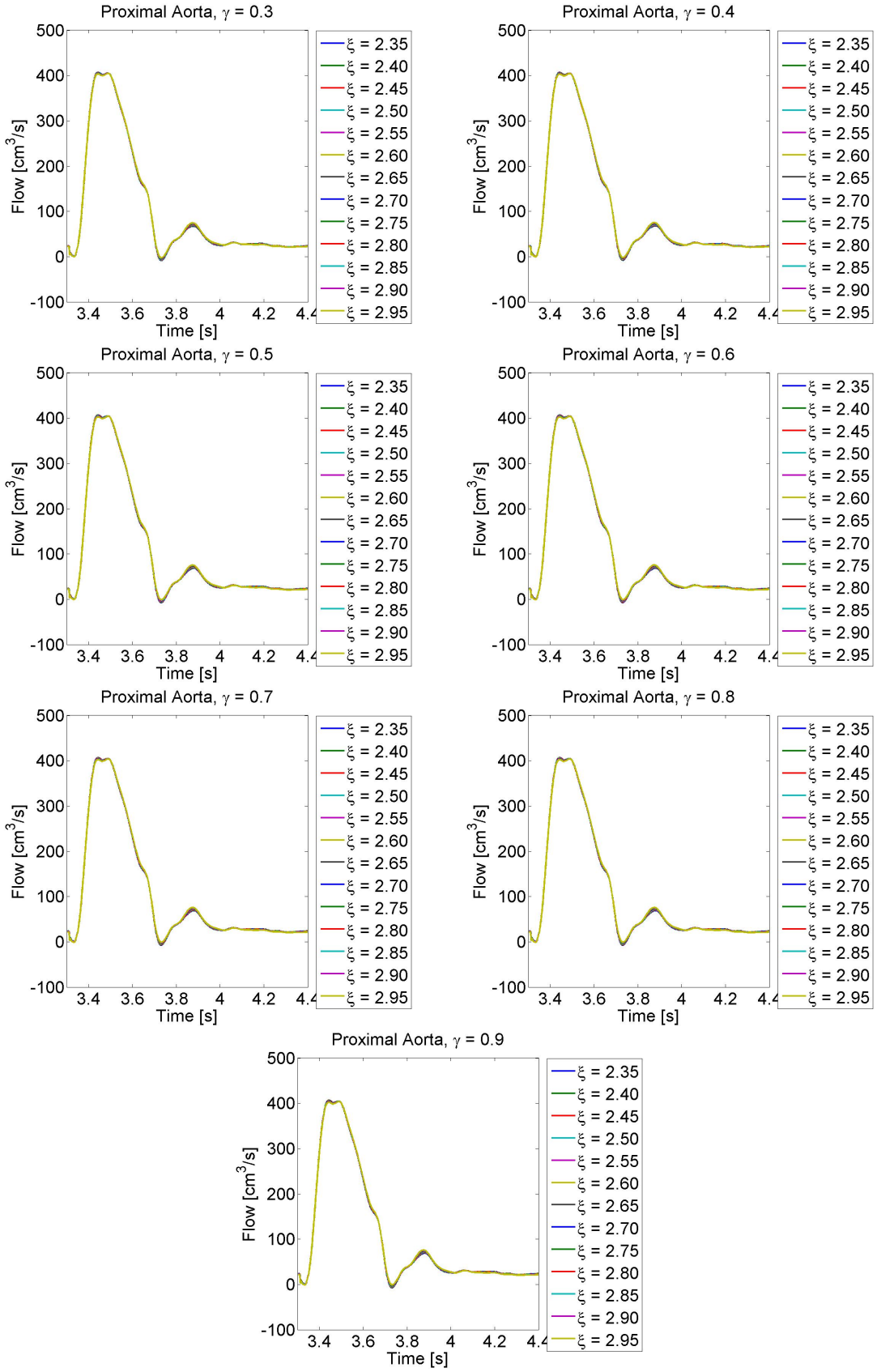

Figure 3.11: Effects of rarefaction on flow waveform in the Proximal Aorta.

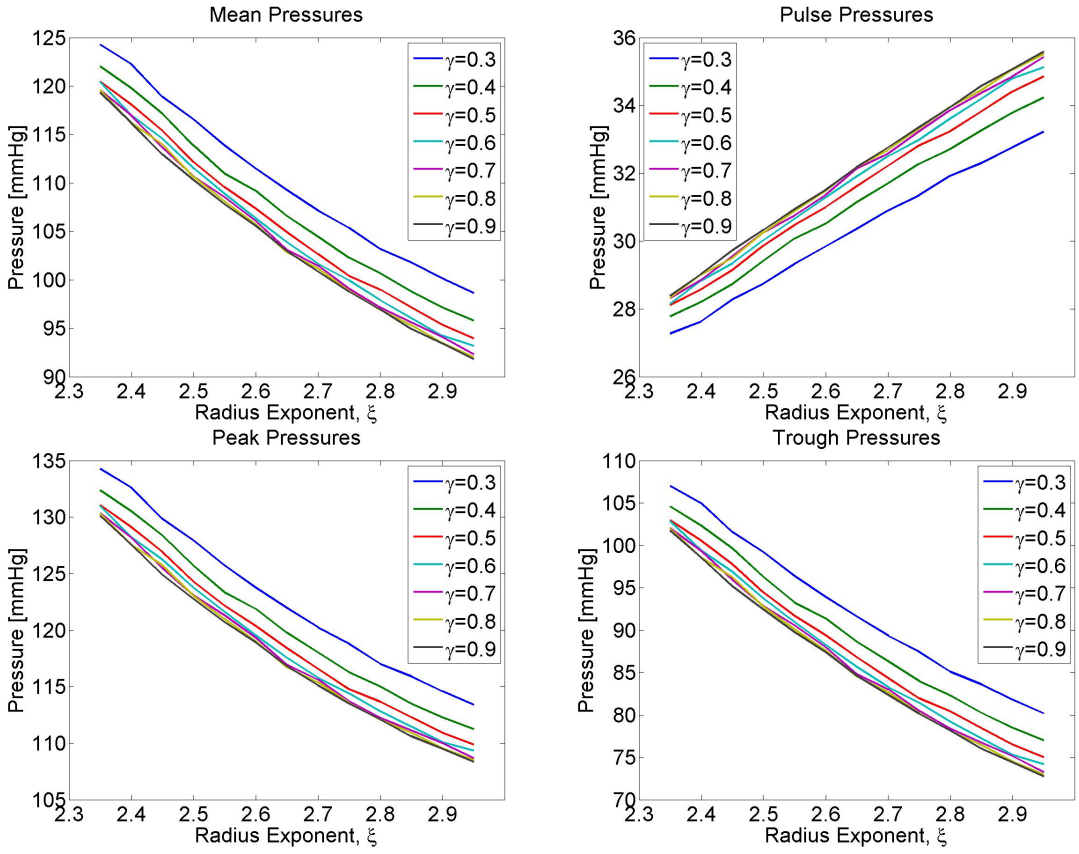

Figure 3.12: Effects of rarefaction on mean, pulse, peak and trough pressure in the Proximal Aorta.

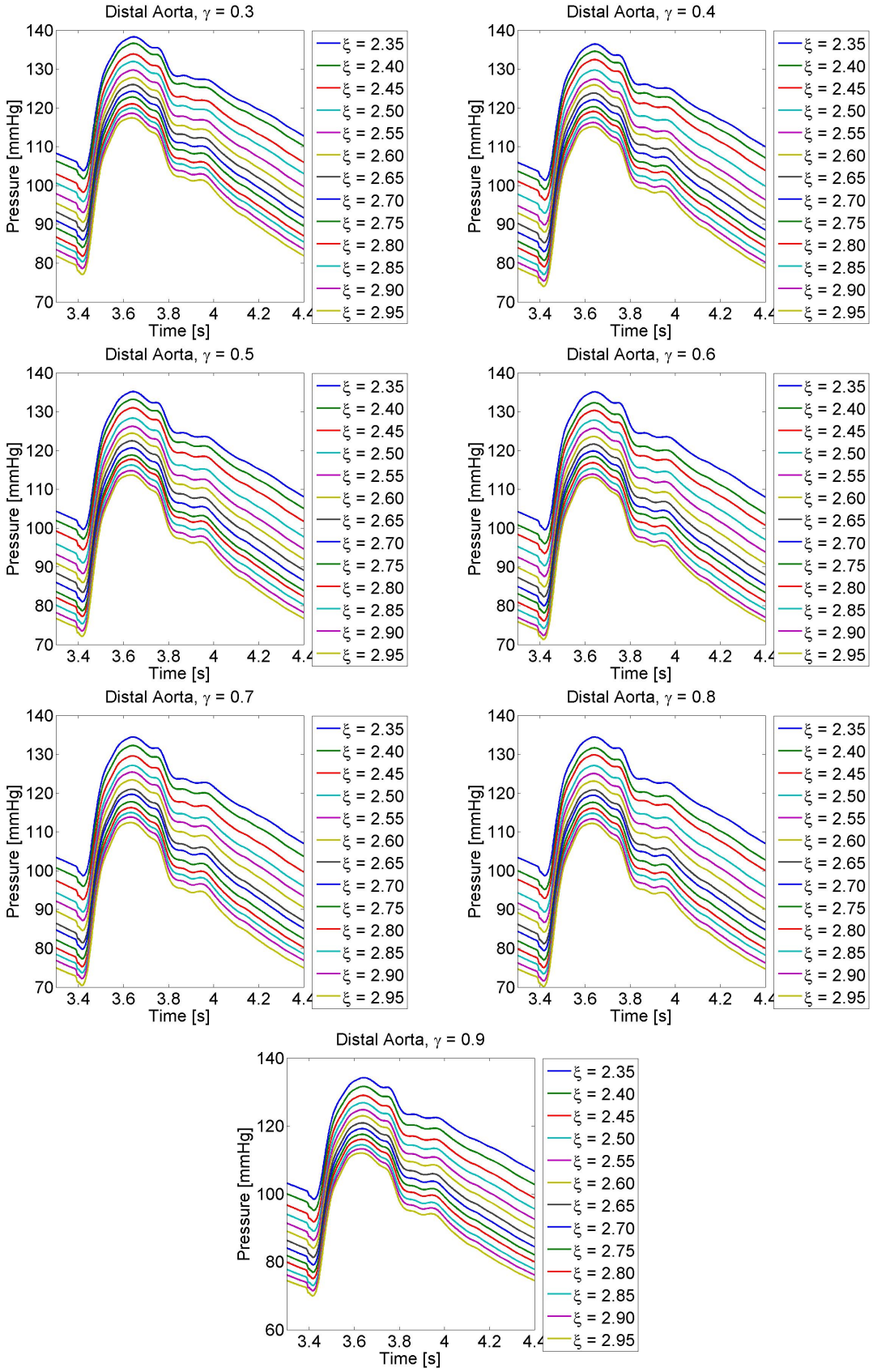

Figure 3.13: Effects of rarefaction on pressure pulse waveform in the Distal Aorta.

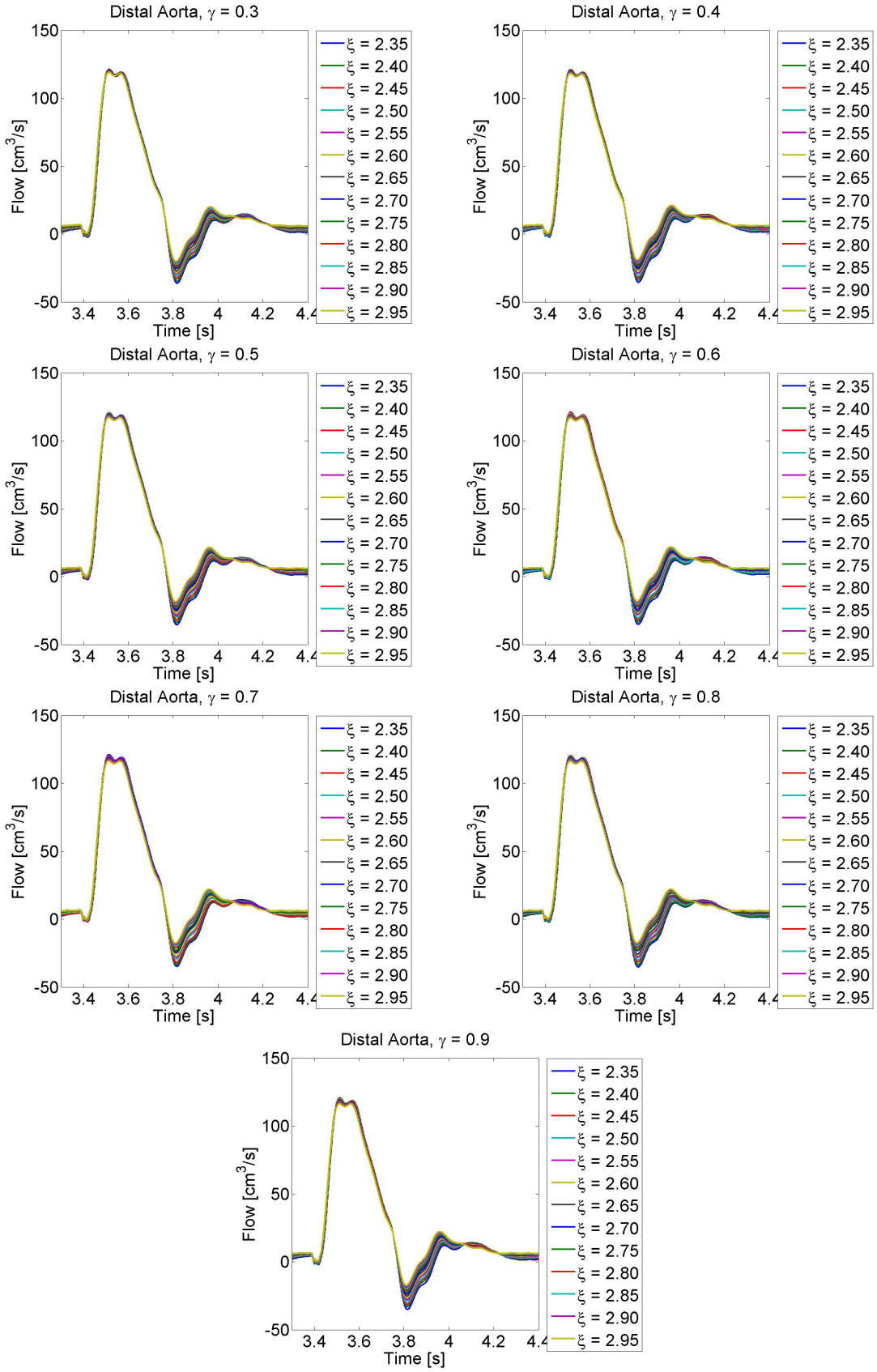

Figure 3.14: Effects of rarefaction on flow waveform in the Distal Aorta.

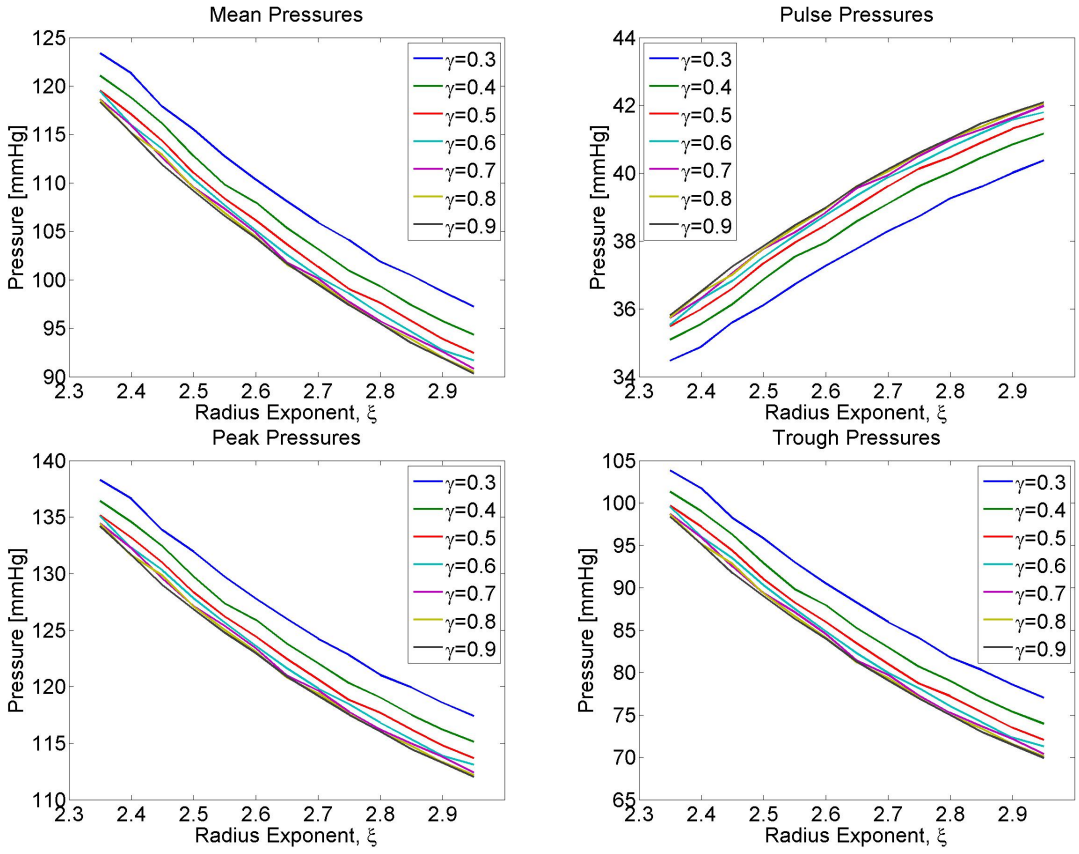

Figure 3.15: Effects of rarefaction on mean, pulse, peak and trough pressure in the Distal Aorta.

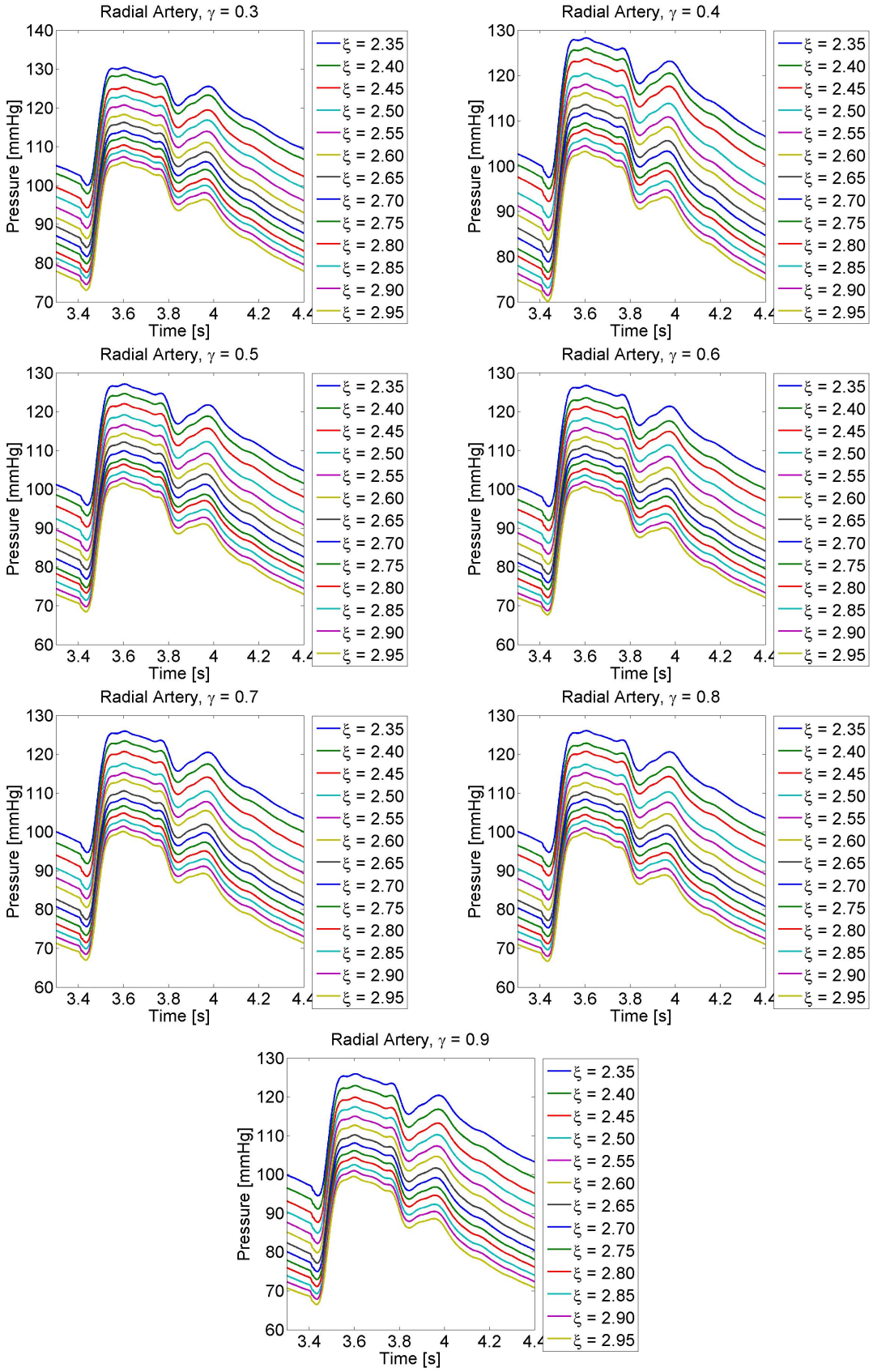

Figure 3.16: Effects of rarefaction on pressure pulse waveform in the Radial Artery.

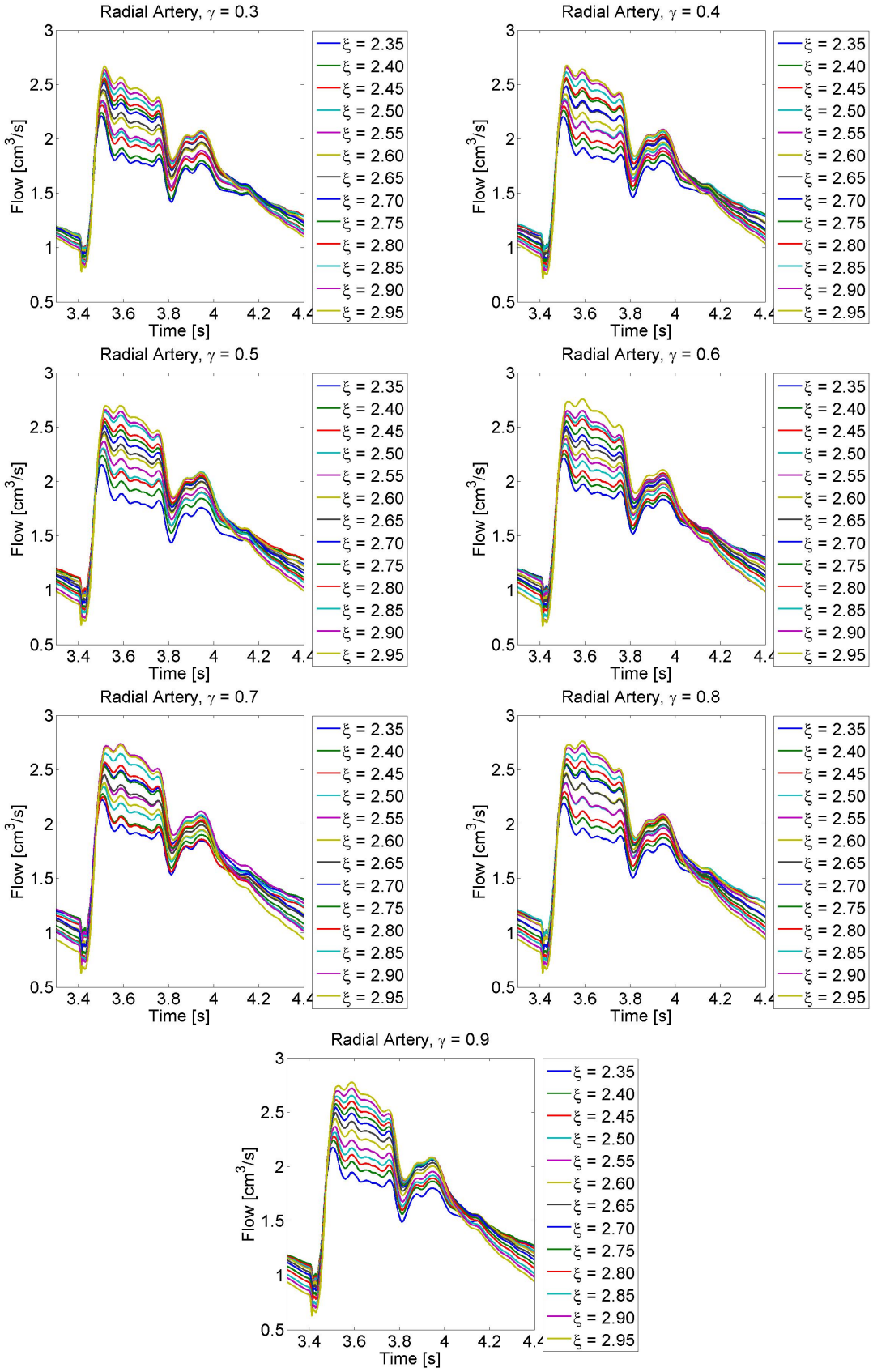

Figure 3.17: Effects of rarefaction on flow waveform in the Radial Artery.

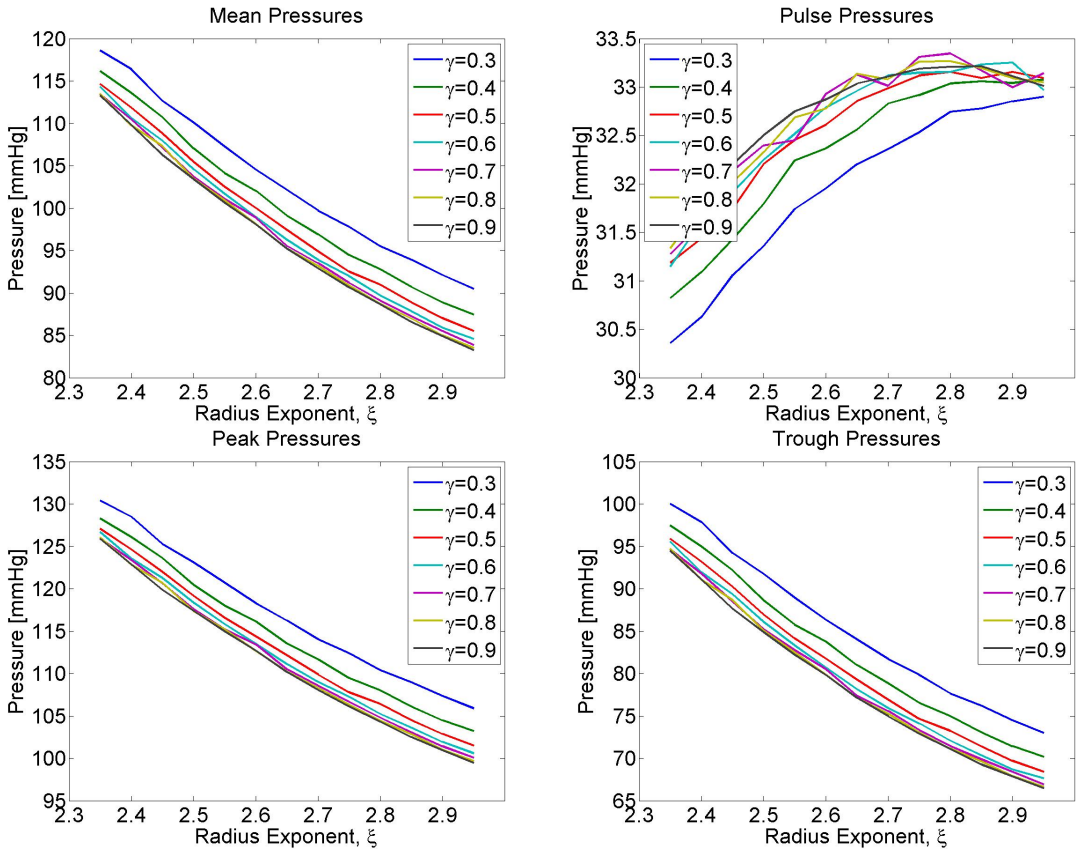

Figure 3.18: Effects of rarefaction on mean, pulse, peak and trough pressure in the Radial Artery.

Interpreting these results

We defined rarefaction previously as a 'reduction of vessels per unit volume within the vascular bed'. Figure 3.8 shows that our method of modelling rarefaction, by reducing the area ratio η of the structured tree, decreases the total number of vessels in the structured tree. Since each vascular bed still has to serve the same area, this can be interpreted as having the desired effect of reducing the overall density of vessels in the vascular bed.

We may further describe rarefaction as an anatomical absence of the smallest calibre of blood vessels, and the terminal vessels of the structured tree are, by their definition, the smallest vessels calibre of vessels in the vascular bed. Figure 3.9 shows again how our modelling of rarefaction simulates this absence of smaller vessels by vastly reducing the number of end vessels in the structured tree.

The effects of this rarefaction of small vessels, as seen in Figures 3.10 - 3.18, are that the simulated pressure waveforms in the large arteries are of higher peak and mean values compared to normal and more densely packed vascular beds. This supports the hypothesis that microcirculatory rarefaction in smaller, distal arteries may indeed be a cause of hypertension in the larger proximal arteries [2], [31].

3.3 Pulse Pressure in Small Arteries.

As mentioned previously, the haemodynamic pressure drop in the systemic arteries occurs mostly across the smaller 'resistance' arteries [28], [41]. While Olufsen's model [32], [34], [35] takes into account the effect of the smaller arteries on the flow and pressure of the larger arteries by means of the overall impedance of the tree of smaller arteries, the flow and pressure in the smaller arteries is not explicitly determined. We have now developed a method to adapt Olufsen's model to provide theoretical calculations of the pressure pulse in the small resistance arteries, without losing the overall efficiency of the original model.

Equations for a single vessel

Olufsen's model for small arteries (see Section 2.2) tells us that at any spatial point, x, along a vessel, the flow and pressure at that point, for frequency ω in the frequency domain, can be found respectively by,

$$Q(x,\omega) = a\cos(\omega x/c) + b\sin(\omega x/c), \text{ and} \tag{3.4}$$

$$P(x,\omega) = i\sqrt{\frac{\rho}{CA_0(1-F_J)}}(-a\sin(\omega x/c) + b\cos(\omega x/c)), \tag{3.5}$$

with wave speed $c = \sqrt{\frac{A_0(1-F_J)}{\rho C}}$, and $g_\omega = cC = \sqrt{CA_0(1-F_J)/\rho}$, and where a and b are constants.

Non-dimensionalising these equations by

$$P(x,\omega) = \rho g l \tilde{P}(x,\omega), \text{ and} \tag{3.6}$$

$$Q(x,\omega) = q_c \tilde{Q}(x,\omega), \tag{3.7}$$

where ρ is the density of blood, g is acceleration due to gravity, l is the characteristic length, and q_c is the characteristic flow, allows for the non-dimensional form of the impedance, $\tilde{Z}(x,\omega)$, to be found from its dimensional form $Z(x,\omega)$ by,

$$Z(x,\omega) = \frac{P(x,\omega)}{Q(x,\omega)} = \frac{\rho g l}{q_c}\frac{\tilde{P}(x,\omega)}{\tilde{Q}(x,\omega)} = \frac{\rho g l}{q_c}\tilde{Z}(x,\omega). \tag{3.8}$$

Vessel boundaries

At the start of a vessel, i.e. where $x = 0$, inlet flow and pressure can be written as,

$$Q(0,\omega) = a, \text{ and} \tag{3.9}$$

$$P(0,\omega) = ib/g_\omega, \tag{3.10}$$

allowing constants a and b to be represented in terms of the non-dimensional flow and pressure at the start of a vessel, i.e.,

$$a = q_c\tilde{Q}(0,\omega), \text{ and} \tag{3.11}$$

$$b = -ig_\omega\rho gl\tilde{P}(0,\omega). \tag{3.12}$$

At the end of a vessel, i.e. when $x = L$, outlet pressure can be written as,

$$P(L,\omega) = (i/g_\omega)(-a\sin(\omega L/c) + b\cos(\omega L/c)), \tag{3.13}$$

meaning that, by substituting for constants a and b, the non-dimensional pressure at the end of a vessel can be determined in terms of the non-dimensional flow and pressure at the beginning of the vessel,

$$\rho gl \cdot \tilde{P}(L,\omega) = (i/g_\omega)(-q_c\tilde{Q}(0,\omega)\sin(\omega L/c) - ig_\omega\rho gl\tilde{P}(0,\omega)\cos(\omega L/c)), \tag{3.14}$$

$$\text{i.e. } \tilde{P}(L,\omega) = \tilde{P}(0,\omega)\cos(\omega L/c) - \frac{iq_c}{g_\omega\rho gl}\tilde{Q}(0,\omega)\sin(\omega L/c). \tag{3.15}$$

Also, the non-dimensional flow at the end of a vessel can be determined via its relationship with pressure and impedance,

$$\tilde{Q}(L,\omega) = \frac{\tilde{P}(L,\omega)}{\tilde{Z}(L,\omega)}. \tag{3.16}$$

The Structured Tree

In Olufsen's model, the smaller arteries are treated as an asymmetric binary structured tree of non-tapering one-dimensional vessels. At each bifurcation in the structured tree, the left and right daughter vessel lengths and radii are determined by scaling the length and radius of the parent vessel by scaling factors α and β respectively, as shown in Figure 2.4.

Given this description, we shall from here on notationally refer to pressure, flow and impedance at the end of the root vessel as

$$\tilde{P}(L,\omega) = P_L^0,$$

$$\tilde{Q}(L,\omega) = Q_L^0,$$

$$\tilde{Z}(L,\omega) = Z_L^0,$$

and the pressure, flow and impedance at the start and end of a generic vessel of the structured tree, that has been scaled by a factor $\alpha^n\beta^m$ with respect to the root vessel, as,

$$\tilde{P}(0,\omega) = P_0^{\alpha^n\beta^m},$$

$$\tilde{P}(L,\omega) = P_L^{\alpha^n\beta^m},$$

$$\tilde{Q}(0,\omega) = Q_0^{\alpha^n\beta^m},$$

$$\tilde{Q}(L,\omega) = Q_L^{\alpha^n\beta^m},$$

$$\tilde{Z}(0,\omega) = Z_0^{\alpha^n\beta^m},$$

and

$$\tilde{Z}(L,\omega) = Z_L^{\alpha^n\beta^m}.$$

Vessels α and β

Since pressure is continuous across a bifurcation, the pressure at the beginning of vessel α, P_0^α, is the same as the pressure at the end of its parent vessel, P_L^0. Further, the flow at the beginning of vessel α, Q_0^α, can be found from the pressure, P_0^α, and the impedance, Z_0^α, at that point, from

$$Q_0^\alpha = P_0^\alpha / Z_0^\alpha. \tag{3.17}$$

Knowing the flow and pressure at the beginning of vessel α, equation (3.15) allows us to determine the pressure at the end of that vessel,

$$P_L^\alpha = P_0^\alpha \cos(\omega L^\alpha / c^\alpha) - (iq_c / g_\omega^\alpha \rho g l) Q_0^\alpha \sin(\omega L^\alpha / c^\alpha), \tag{3.18}$$

which further allows us to determine the flow at the end of vessel α from equation (3.16),

$$Q_L^\alpha = P_L^\alpha / Z_L^\alpha. \tag{3.19}$$

An identical argument can be applied to vessel β, the other daughter vessel of the root vessel of the structured tree, giving,

$$P_L^\beta = P_0^\beta \cos(\omega L^\beta / c^\beta) - (iq_c / g_\omega^\beta \rho g l) Q_0^\beta \sin(\omega L^\beta / c^\beta), \tag{3.20}$$

and,

$$Q_L^\beta = P_L^\beta / Z_L^\beta. \tag{3.21}$$

The α branch

The succession of vessels scaled by a factor α from its parent vessel is what we refer to as the α branch of the structured tree, represented graphically by the leftmost branch in Figure 2.4. Since $\alpha > \beta$, the α branch represents the longest possible route from the root to the terminus of the structured tree.

By the argument in the previous section, the pressure at the end of any vessel in the α branch can be found as,

$$P_L^{\alpha^n} = P_0^{\alpha^n} \cos(\omega L^{\alpha^n}/c^{\alpha^n}) - (iq_c/g_\omega^{\alpha^n}\rho gl)Q_0^{\alpha^n} \sin(\omega L^{\alpha^n}/c^{\alpha^n}), \tag{3.22}$$

where the pressure at the start of the vessel is the same as the pressure at the end of its parent vessel, i.e.,

$$P_0^{\alpha^n} = P_L^{\alpha^{n-1}}. \tag{3.23}$$

and the flow at either the start or end of the vessel can be determined from the pressure and the impedance, e.g.,

$$Q_0^{\alpha^n} = P_0^{\alpha^n}/Z_0^{\alpha^n}. \tag{3.24}$$

This means that for any vessel in the α branch,

$$P_L^{\alpha^n} = P_L^{\alpha^{n-1}} \cos(\omega L^{\alpha^n}/c^{\alpha^n}) - (iq_c/g_\omega^{\alpha^n}\rho gl)(P_L^{\alpha^{n-1}}/Z_0^{\alpha^n}) \sin(\omega L^{\alpha^n}/c^{\alpha^n}), \tag{3.25}$$

so that the pressure at the end of any vessel can be found from the pressure at the beginning of the root vessel, and the impedances at the beginning of each vessel in the structured tree - both of which are pre-determined in Olufsen's model. This allows us to calculate the pressure (and, through its relation with the impedance, the flow) in any vessel of the α branch, without losing the numerical efficiency of Olufsen's original model.

An algorithm for determining pressures in the α branch

- Read $p_L^0(t)$ from file (in time domain).
- Transform $p_L^0(t)$ to $P_L^0(\omega)$ (frequency domain) by $P_L^0(\omega) = FFT(p_L^0(t))$.
- For each frequency,
  - Compute impedances for the tree.
  - For each vessel in Computed$(i, 0)$,
    - Get $P_0^{\alpha^i}$ from parent vessel using (3.23) and store.
    - Compute $P_L^{\alpha^i}$ using (3.22).
  - End For.
- End For.
- Transform $P_0^{\alpha^i}(\omega)$ to $p_0(t)$ (time domain) by $p_0(t) = IFFT(P_0(\omega))$.
- Convert $p_0(t)$ to mmHg by $p_0(t) = \tilde{p}_0(t) \cdot \rho gl/1332.20$

The β branch

By an identical argument as for the α branch, we can determine the pressures (and flows) in any generation of the β branch by,

$$P_L^{\beta^n} = P_L^{\beta^{n-1}} \cos(\omega L^{\beta^n}/c^{\beta^n}) - (iq_c/g_\omega^{\beta^n} \rho gl)(P_L^{\beta^{n-1}}/Z_0^{\beta^n}) \sin(\omega L^{\beta^n}/c^{\beta^n}). \tag{3.26}$$

The β branch represents the shortest possible route from the root to the terminus of the structured tree.

Self similarity in the Structured Tree

The composition of the structured tree is such that it is possible to have more than one vessel that has been scaled by the same factor, with respect to the root vessel, but have different parent vessels. For example, vessel $\alpha\beta$ (parent vessel α) and vessel $\alpha\beta$ (parent vessel β) will have identical physical characteristics (length, radius), but because they have different parentage, the pressures in these vessels will be different. Despite this, it is still possible to find a relation between the pressures in these vessels. For vessel $\alpha\beta$,

$$P_L^{\alpha\beta} = P_0^{\alpha\beta}\cos(\omega L^{\alpha\beta}/c^{\alpha\beta}) - (iq_c/g_\omega^{\alpha\beta}\rho gl)Q_0^{\alpha\beta}\sin(\omega L^{\alpha\beta}/c^{\alpha\beta}) \tag{3.27}$$

$$= P_L^{\alpha}\cos(\omega L^{\alpha\beta}/c^{\alpha\beta}) - (iq_c/g_\omega^{\alpha\beta}\rho gl)(P_L^{\alpha}/Z_0^{\alpha\beta})\sin(\omega L^{\alpha\beta}/c^{\alpha\beta}), \tag{3.28}$$

and for vessel $\beta\alpha$,

$$P_L^{\beta\alpha} = P_L^{\beta}\cos(\omega L^{\alpha\beta}/c^{\alpha\beta}) - (iq_c/g_\omega^{\alpha\beta}\rho gl)(P_L^{\beta}/Z_0^{\alpha\beta})\sin(\omega L^{\alpha\beta}/c^{\alpha\beta}), \tag{3.29}$$

so that,

$$\frac{P_L^{\beta\alpha}}{P_L^{\alpha\beta}} = \frac{P_L^{\beta}\cos(\omega L^{\alpha\beta}/c^{\alpha\beta}) - P_L^{\beta}(iq_c/Z_0^{\alpha\beta}g_\omega^{\alpha\beta}\rho gl)\sin(\omega L^{\alpha\beta}/c^{\alpha\beta})}{P_L^{\alpha}\cos(\omega L^{\alpha\beta}/c^{\alpha\beta}) - P_L^{\alpha}(iq_c/Z_0^{\alpha\beta}g_\omega^{\alpha\beta}\rho gl)\sin(\omega L^{\alpha\beta}/c^{\alpha\beta})} \tag{3.30}$$

$$= \frac{P_L^{\beta}}{P_L^{\alpha}}. \tag{3.31}$$

This gives us the similarity relations,

$$P_L^{\beta\alpha} = \left(\frac{P_L^{\beta}}{P_L^{\alpha}}\right) P_L^{\alpha\beta}, \tag{3.32}$$

and,

$$Q_L^{\beta\alpha} = \left(\frac{P_L^{\beta}}{P_L^{\alpha}}\right) Q_L^{\alpha\beta}, \tag{3.33}$$

since $Z_0^{\alpha\beta} = Z_0^{\beta\alpha}$, $L^{\alpha\beta} = L^{\beta\alpha}$, $c^{\alpha\beta} = c^{\beta\alpha}$, and $g_\omega^{\alpha\beta} = g_\omega^{\beta\alpha}$.

Results

Using the algorithm described earlier, Figure 3.19 shows the overlayed pressure profiles from successive vessels of the α branch of the vascular bed at the termination of the Femoral artery (vessel 24 in Figure 2.5), as well as the mean pressure with radius along the branch. The forward propagation of the pressure pulse, and pressure drop along the branch is clearly visible.

Figure 3.20 shows the mean pressures for all vessels in the Femoral arterial bed, as well as the number of vessels of each size, with the region relating to the microcirculation expanded on the right hand side. These are found by creating a number of bins of radius ranges, and calculating the mean pressure of-, and number of-, vessels in each bin. Since there are far more smaller arteries than there are larger arteries, some of the bins in the regions of the large arteries contain no vessels.

Figures 3.21 - 3.24 show the same results for each of the Renal arterial bed (at the terminal of vessel 14 in Figure 2.5), and the Carotid arterial bed (at the terminal of vessel 4 in Figure 2.5).

Interpreting these results

In each of the three regions we investigated, but most visible in the femoral arterial bed, the steepest drop in blood pressure occurs over arteries of less than 0.050cm radius, suggesting these as the location of the 'resistance arteries'. A limitation of our model, however, is that any vessel of less than 0.010cm radius is automatically denoted as a terminal vessel of the structured tree due to the minimum radius parameter, forcing our predictions of the pre-capillary pressure drop to occur over vessels larger than this value. This could be improved by reducing our minimum radius parameter, and sectioning the structured tree to allow for different physical properties of very small vessels down to the level of capillaries (which are currently ignored). Until then, the true location of the 'resistance arteries' remains unclear [10].

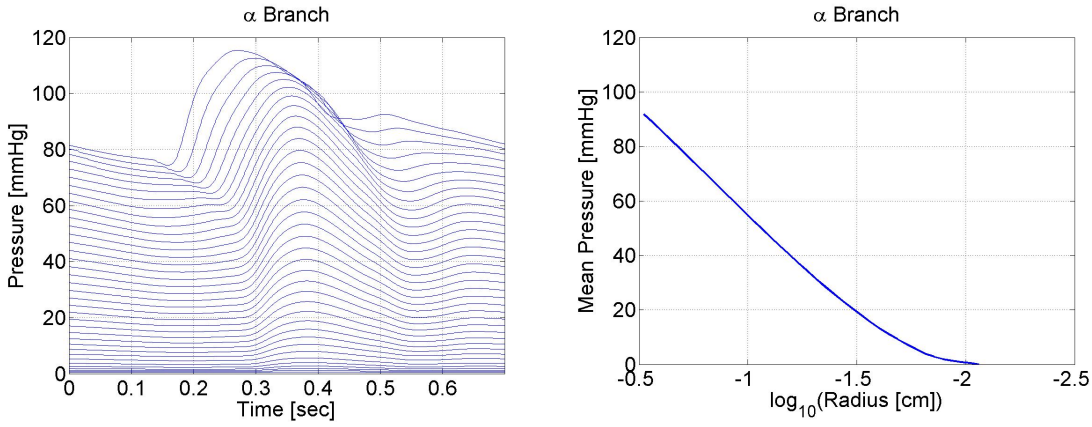

Figure 3.19: Pressure in the Femoral Arterial vascular bed.

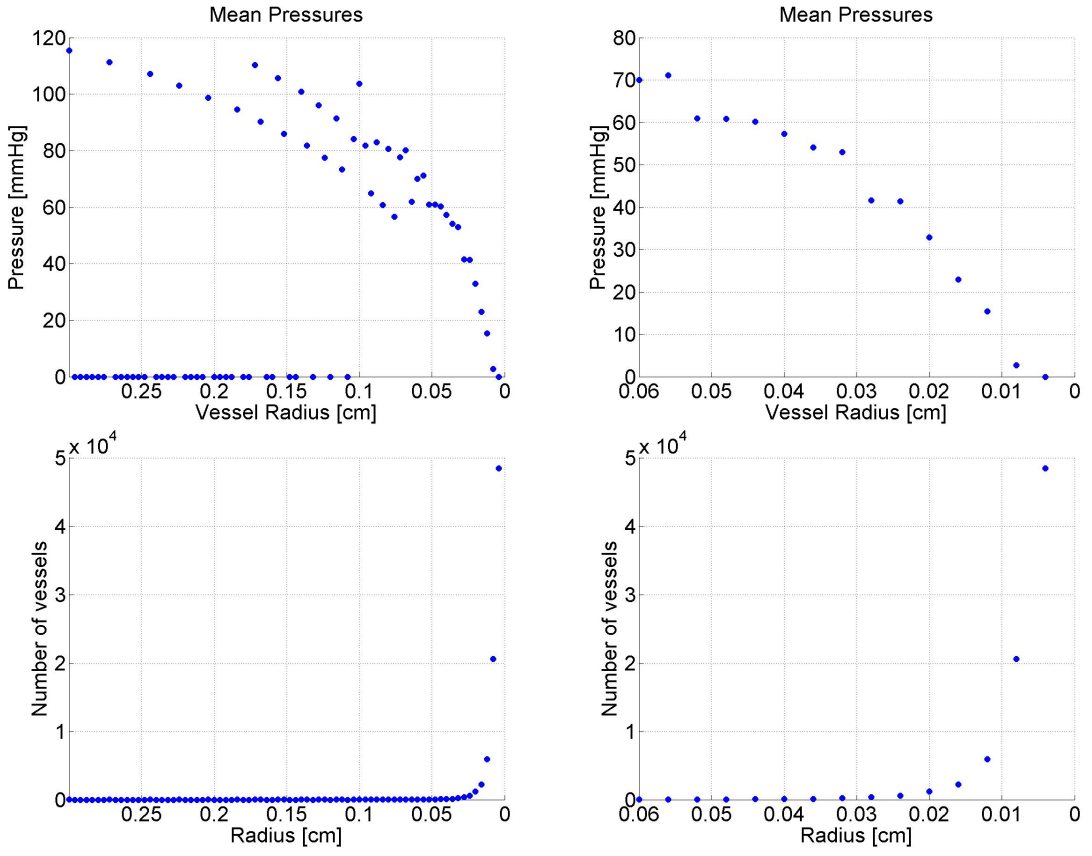

Figure 3.20: Mean pressures and number of vessels versus radius in the Femoral Arterial vascular bed.

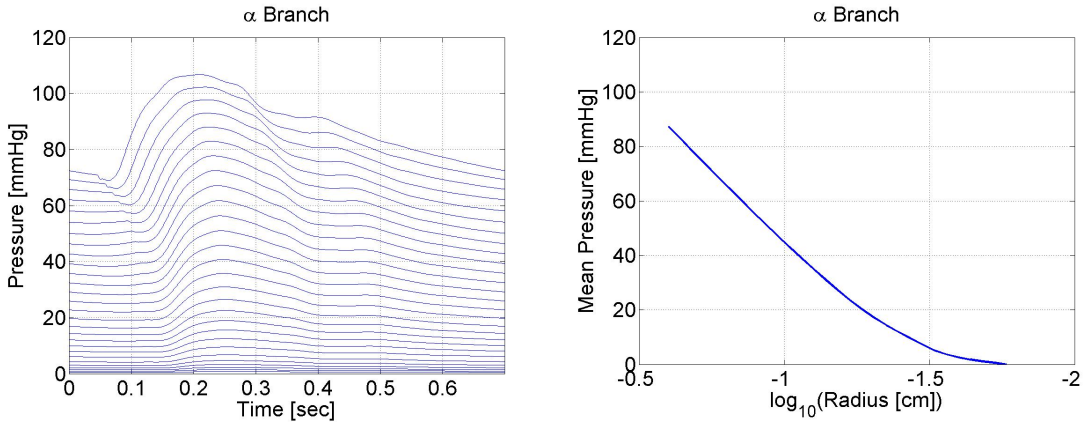

Figure 3.21: Pressure in the Renal Arterial vascular bed.

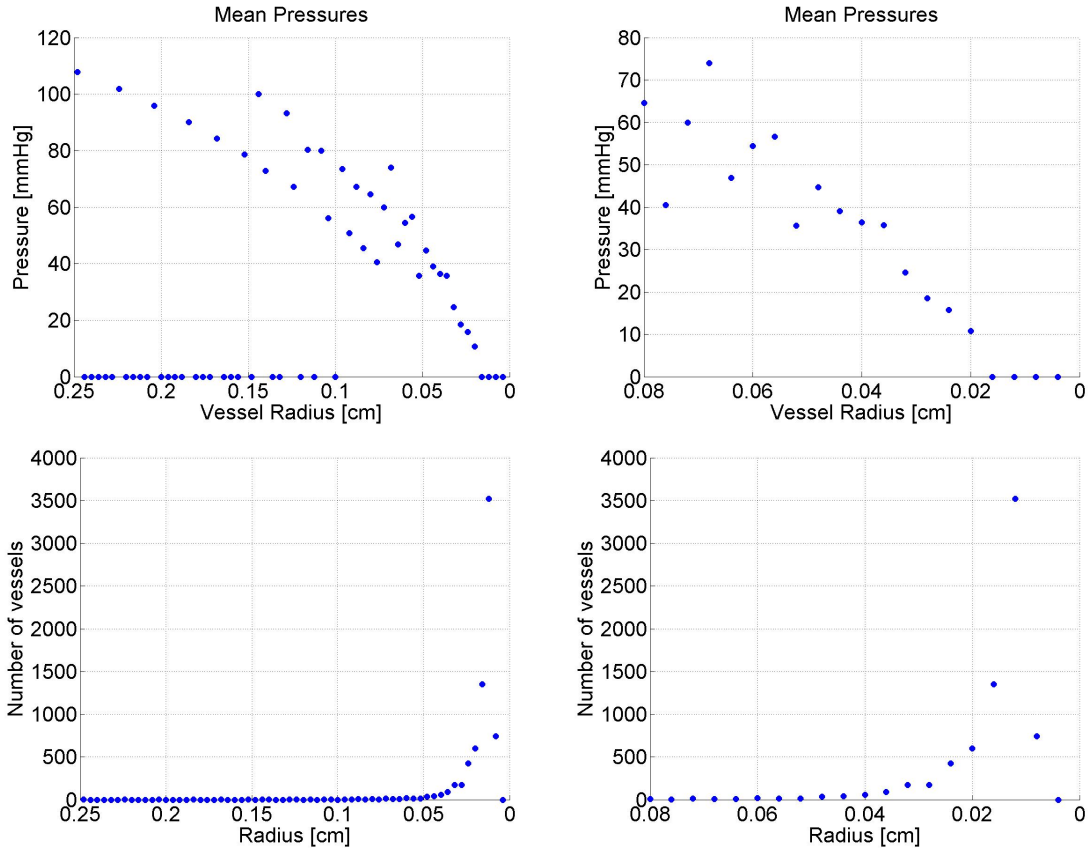

Figure 3.22: Mean pressures and number of vessels versus radius in the Renal Arterial vascular bed.

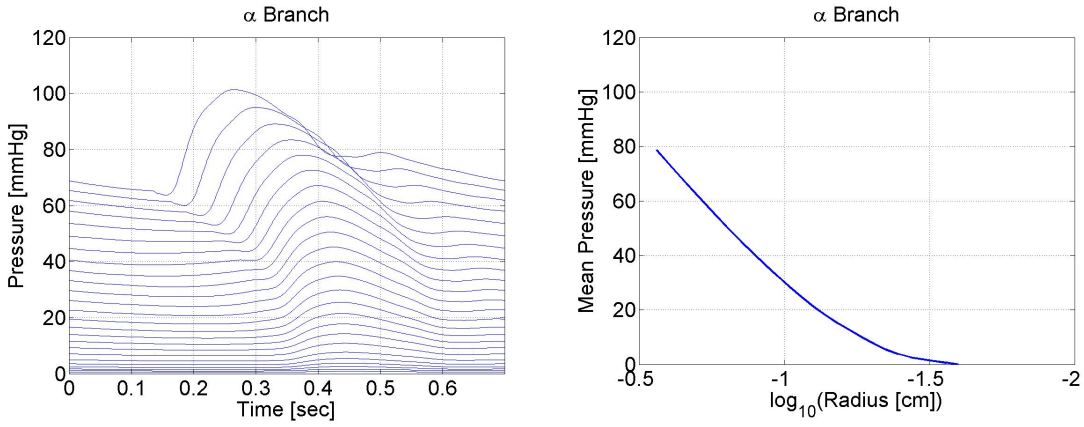

Figure 3.23: Pressure in the Carotid Arterial vascular bed.

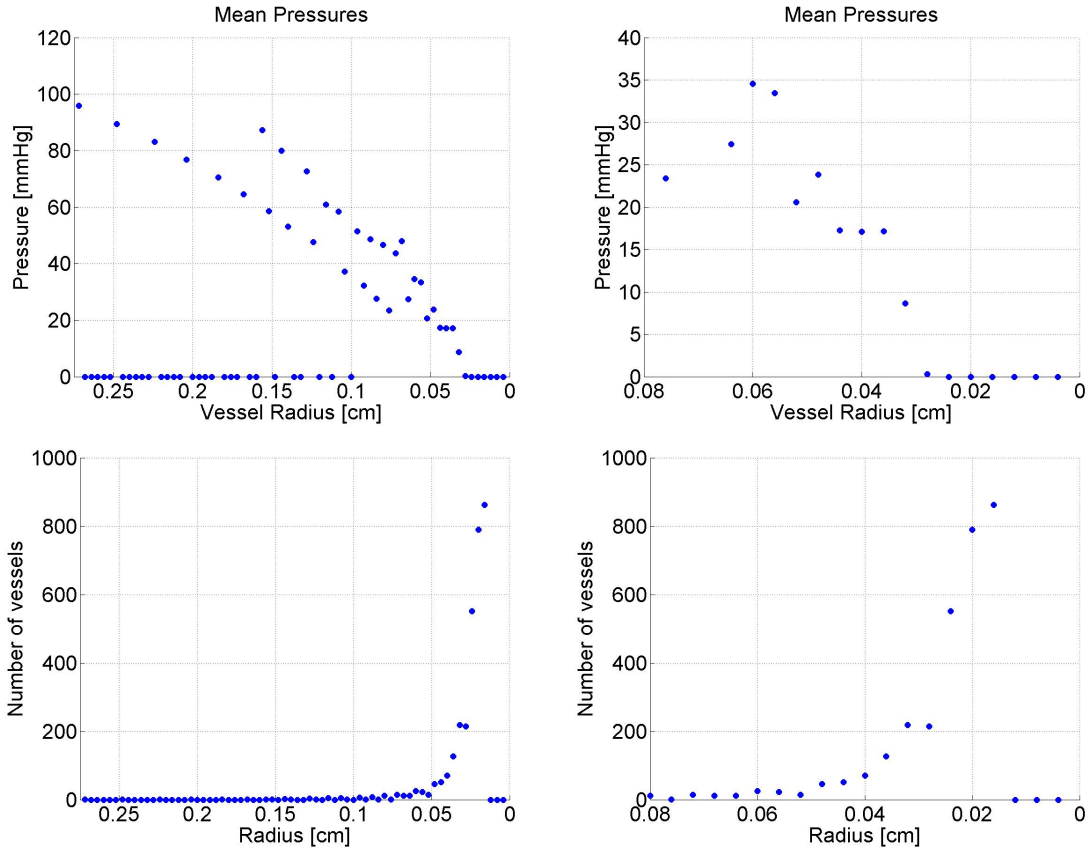

Figure 3.24: Mean pressures and number of vessels versus radius in the Carotid Arterial vascular bed.

3.4 A Pulmonary Arterial Model

By changing the description of the large systemic arteries in Olufsen's model to instead describe the the geometry and structure of the large pulmonary arteries, but still utilising the structured tree outflow condition, we can produce a first attempt at a pulmonary arterial model.

Since this model describes only the arterial side of the pulmonary circulation, and since the terminal condition for the structured tree outflow condition is one of zero impedance (and hence zero pressure), we know that this description can not be entirely accurate as it is known that there is a noticeable pressure pulse measurable in the pulmonary veins. However, by constructing this model we can show both the requirement for, and later the improved accuracy of, our full pulmonary circulation model.

Large Vessel Structure

Thanks to our collaborators in the Scottish Pulmonary Vascular Unit, we have obtained detailed measurements of the structure of the largest pulmonary arteries of a healthy volunteer through magnetic resonance imaging (MRI). Figure 3.25 shows a schematic of the measured arteries (the first three generations of the pulmonary arterial tree), indicating the lengths and diameters that were measured, and how the measured vessels were indexed, with the measured values summarised in Table 3.1. Two vessels - numbered 4 and 6 in Figure 3.25 and Table 3.1 - were too short to determine their inlet diameters and length, however their outlet diameters were measured and so these vessels were assumed to be short and non-tapering. Further, the lengths of all vessels measured have been rounded to the nearest 0.250cm to match the spatial resolution used in the numerical computation.

Vessel 0, the main pulmonary artery, is the initial vessel of the pulmonary circulation, so the inlet of this vessel is where we attach our inflow condition representing the flow emerging from the right ventricle. Vessels 3, 4, 5, and 6 are the terminal vessels of the large pulmonary arterial model, and it is to the outlet of these vessels that we attach the structured tree outflow conditions.

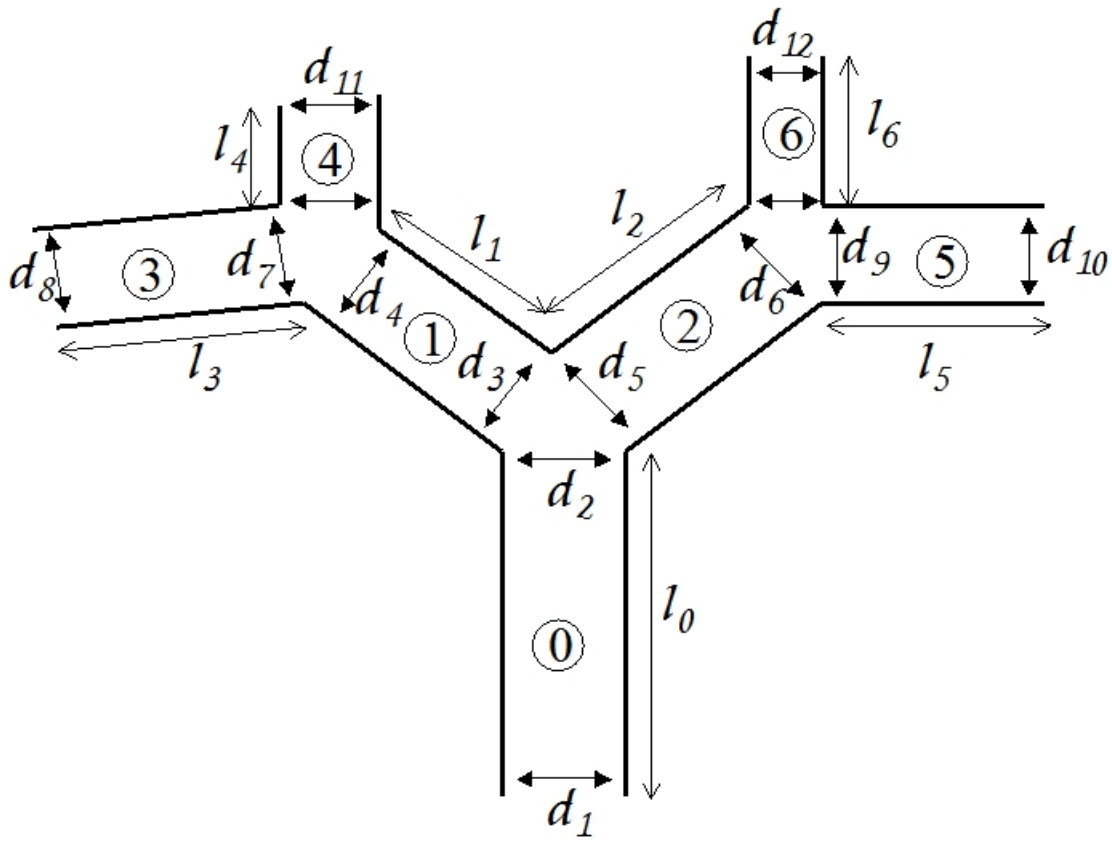

Figure 3.25: Schematic of the large Pulmonary arteries, as measured by MRI.

Vessel No.	Vessel Name	Inlet diameter (cm)	Outlet diameter (cm)	Vessel Length (cm)	Notes
0	Main Pulmonary Artery	2.720	2.600	4.500	Measured length 4.46cm
1	Right Pulmonary Artery	1.850	1.210	5.750	Measured length 5.79cm
2	Left Pulmonary Artery	2.210	2.160	2.500	Measured length 2.48cm
3	Left Interlobal Artery	1.140	1.100	1.250	Measured length 1.24cm
4	-	0.930	0.930	0.500	Estimated length, no taper
5	Right Interlobal Artery	2.080	1.810	2.250	Measured length 2.18cm
6	-	1.160	1.160	0.500	Estimated length, no taper

Table 3.1: Dimensions of the large vessels of the Pulmonary arterial model. These fall within the typical values suggested by the data of Singhal et al. [46] and Huang et al. [21].

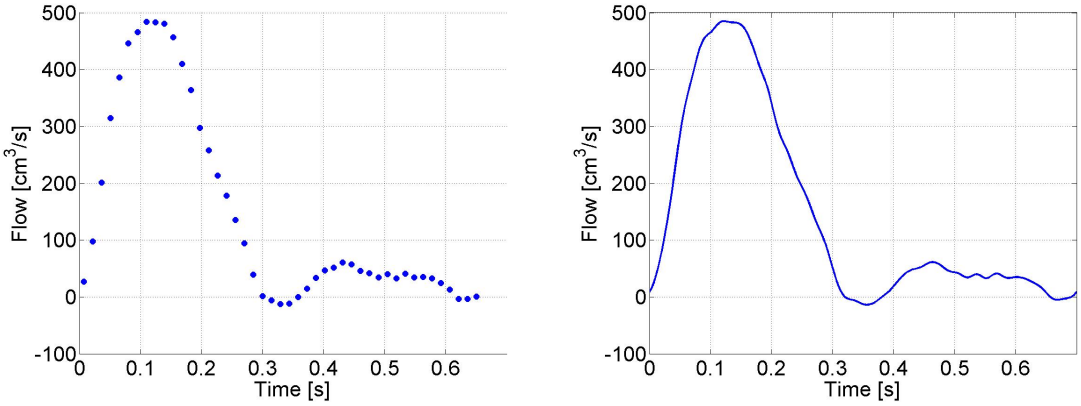

Figure 3.26: Pulmonary inflow profile (flow into the main pulmonary artery from the right ventricle), as determined by MRI (left image, 45 points per period) and after interpolation (right image, 8192 points per period). The shape of this waveform is typical, however the cardiac output is slightly higher than in the measurements of Cheng et al. [8], [9].

Inflow Condition

During the MRI scans to measure the the structure of the pulmonary arteries, it was also possible to measure the flow through these vessels. This allowed us to measure the inflow into the pulmonary system at the inlet of the main pulmonary artery. The flow rate was measured at 45 equally spaced time points over the period of one heart beat, as shown in the left graph of Figure 3.26, but by using a numerical spline we can interpolate this to 8192 points per period, the resulting periodic profile shown in the right graph in Figure 3.26. This increased temporal resolution matches that of our numerical model, and allows us to use the flow profile described in Figure 3.26 as our inflow condition to the model.

Outflow Condition - Structured Tree

For our first attempt at a Pulmonary arterial model we continue to use the structured tree outflow condition as described by Olufsen and in the previous chapter. Since the data used to evaluate the parameters which determine the branching structure of the systemic structured tree (the branching exponent, ξ, the asymmetry ratio γ and the area ratio, η) were found by considering the data from many studies, including those of the pulmonary system [44], we believe it is reasonable to assume that these values, $\xi = 2.70$, $\gamma = 0.9$ and $\eta = 1.16$, are still relevant in describing the branching structure of the smaller pulmonary arteries.

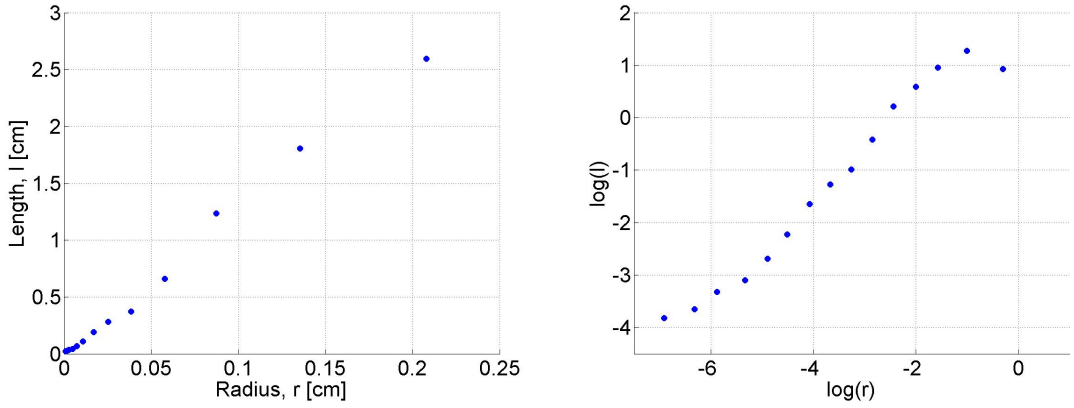

Figure 3.27: Vessel radius vs length for pulmonary arteries, data from Huang et. al. [21].

One parameter, however, which is significantly different in the pulmonary arteries when compared with the systemic arteries is the length to radius ratio, l_{rr} of the vessel segments of the structured tree. Data collated by Fung [14] (based on studies by Singhal et. al. [46]) and most recently data collected by Huang et. al. [21] show that arterial vessel segment lengths, when compared with their radii, are considerably shorter in the pulmonary circulation ($l_{rr} \sim 10 - 20$) than in the systemic circulation ($l_{rr} \sim 50$) [22].

The left graph of Figure 3.27 shows a plot of radius versus length of vessels of the pulmonary arterial tree, as given by the most recent study of Huang et. al., 1996 [21], with the right graph showing a log-log plot of the same values. The 15 points represent the averaged lengths and radii for each of the 15 orders of the pulmonary tree, as described by the diameter-defined Strahler ordering model (see Appendix B).

The largest orders in Figure 3.27 represent the first few generations of the pulmonary arterial tree - order 15 being the main pulmonary artery, order 14 the left and right pulmonary arteries etc. - which are of course defined explicitly in our pulmonary arterial model. As such, the data for these points is not relevant when determining the parameters for our structured tree.

Ignoring the largest three data points in Figure 3.27, the remaining data can be reasonably approximated by two straight line fits - one for the 4 smallest orders (orders 1 - 4), as shown in the left graph of Figure 3.28, and one for the remaining 8 orders plus the largest order of the other fit (orders 4 - 12), as shown in the right graph in Figure 3.28. These fits lead to length to radius relations of

$$l = e^{2.76} r^{1.10} = 15.75 r^{1.10} \tag{3.34}$$

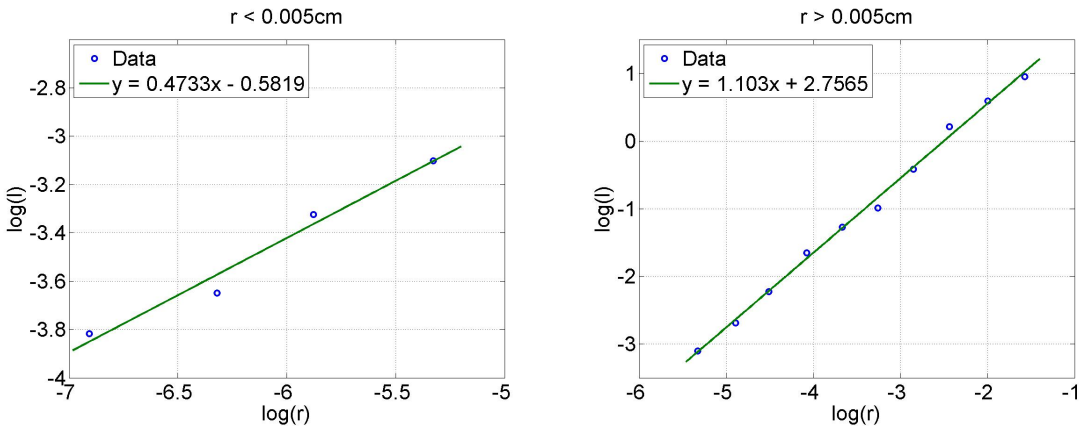

Figure 3.28: Logarithmic plot of radius vs length for vessels of radius $r < 0.005$cm (order 1 - 4) and vessels of radius $r > 0.005$cm (order 4 - 12) respectively.

for vessels of radius $r \geq 0.005$cm, and

$$l = e^{-0.58} r^{0.47} = 0.56 r^{0.47} \tag{3.35}$$

for vessels of radius $r \leq 0.005$cm.

Elastic Properties

The 2003 paper by Krenz and Dawson [24] contains a summary of 26 studies on the distensibility of arteries in pulmonary networks in 6 different species, including humans. They described the distensibility of the vessels in terms of the distensibility parameter, α, defined by

$$D/D_0 = 1 + \alpha P, \tag{3.36}$$

where P is transmural pressure, D is vessel diameter at pressure P, and D_0 is vessel diameter at $P = 0$.

They showed that, across all of the studies they considered, a constant value of $\alpha = 0.02$/mmHg reflected the tendency of all data reasonably well (see Figure 3.29).

Olufsen's model incorporated the elastic properties of vessels through the state equation, (2.6), which can be re-written as,

$$P = \frac{4}{3} \frac{Eh}{r_0} \left(1 - \sqrt{\frac{A_0}{A}} \right), \tag{3.37}$$

where P is again transmural pressure, as in (3.36), A is the cross-sectional area of a vessel at pressure P, and A_0 is this area when $P = 0$. Eh/r_0 is Young's modulus times wall

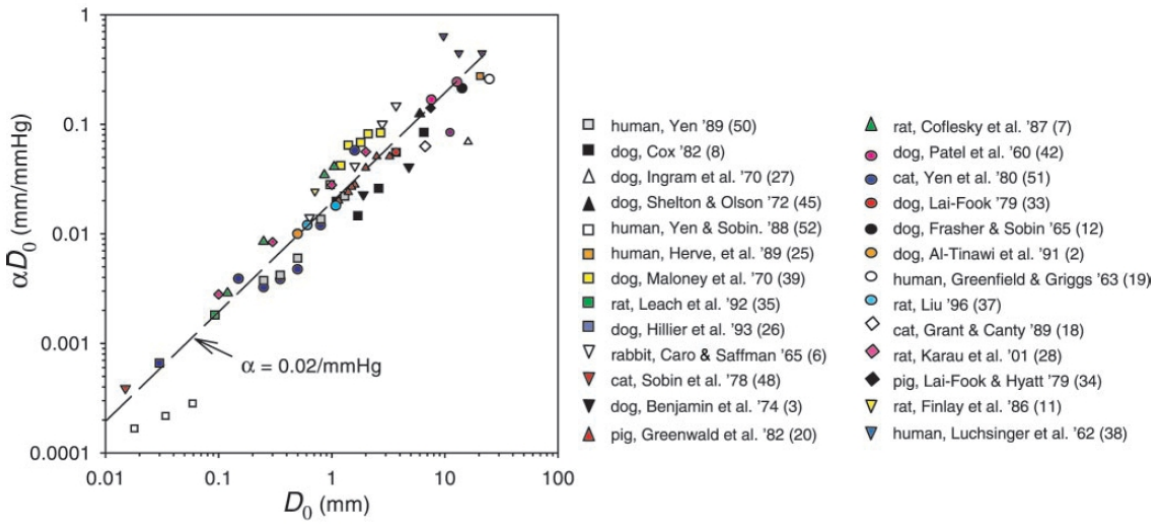

Figure 3.29: Pulmonary arterial distensibilities, from Krenz and Dawson, 2003 [24].

thickness, divided by vessel radius when $P = 0$, and is the parameter we use to represent the elastic properties of blood vessels.

It is this quantity, Eh/r_0, that we wish to relate to the value of α determined by Krenz and Dawson and described above, and we do this by means of the vessel distensibility, defined as,

$$D = \frac{1}{A}\frac{dA}{dP}\bigg|_{P=0}. \tag{3.38}$$

First, we differentiate (3.37) with respect to A to find,

$$\frac{dP}{dA} = \frac{4}{3}\frac{Eh}{r_0}\frac{\sqrt{A_0}}{2A\sqrt{A}}, \tag{3.39}$$

so that

$$\frac{1}{A}\frac{dA}{dP} = \frac{3}{2}\frac{r_0}{Eh}\sqrt{\frac{A}{A_0}} \tag{3.40}$$

and

$$D = \frac{1}{A}\frac{dA}{dP}\bigg|_{P=0} = \frac{3}{2}\frac{r_0}{Eh}, \tag{3.41}$$

since $A = A_0$ when $P = 0$.

Now, by rewriting (3.36) in terms of radius rather than diameter, we can find from it,

$$\frac{1}{A}\frac{dA}{dP} = \frac{1}{\pi r^2}\frac{d(\pi r^2)}{dP} = \frac{2\alpha r_0^2 + 2\alpha^2 r_0^2 P}{r^2}, \tag{3.42}$$

so that

$$D = \frac{1}{A}\frac{dA}{dP}\bigg|_{P=0} = 2\alpha, \tag{3.43}$$

since $r = r_0$ when $P = 0$.

By equating these two expressions for distensibility - equations (3.41) and (3.43) - we can now write Olufsen's stiffness parameter, Eh/r_0, in terms of Krenz and Dawson's distensibility parameter, α, as,

$$\frac{Eh}{r_0} = \frac{3}{4\alpha}. \tag{3.44}$$

Further, whereas Olufsen's model for Eh/r_0 in the systemic arteris varied with vessel radius (see equation (2.3) and Figure 2.2) the value of $\alpha = 0.02$/mmHg derived from Figure 3.29, when substituted into (3.44), suggests a constant value of $Eh/r_0 = 50000\text{g/s}^2\text{cm}$ for the pulmonary arteries, irrespective of vessel radius.

Results

Using the description of the pulmonary arterial structure and properties given in this chapter, the predicted flow and pressure profiles for the Main Pulmonary Artery are shown in the first two graphs in Figure 3.30. The simulation suggests a mean pressure $P_{mean} =$ 7.7mmHg at the inlet of the pulmonary artery, peak pressure of $P_{peak} =$ 13.2mmHg, a trough pressure of around $P_{trough} =$ 2.0mmHg, and thus a pulse pressure $P_{pulse} =$ 11.2mmHg. Although the shape of the predicted pressure pulse and flow waveforms look qualitatively good, these pressure values are noticeably lower than typical pulmonary artery mean pressures of around 14.7mmHg [14], [56].

The remaining graphs of Figure 3.30 show the predicted waveforms in the Right and Left Pulmonary Arteries respectively. While flow is divided up between arteries of each generation, very little change is seen in the pressure profile along each artery. This is further backed up in Figure 3.31 which shows the flow and pressure profiles at the outlet of each of the large terminal arteries (Vessels 3 - 6 in Figure 3.25).

Using the same method as described in the previous section, Figure 3.32 shows the propagation of the pressure pulse and mean pressure along the α branch of the structured tree attached to the terminal of Vessel 3 in Figure 3.25. Figure 3.33 further shows the mean pressures against radius across the entirety of the same vascular bed, with the number of vessel with radius shown in the right graph.

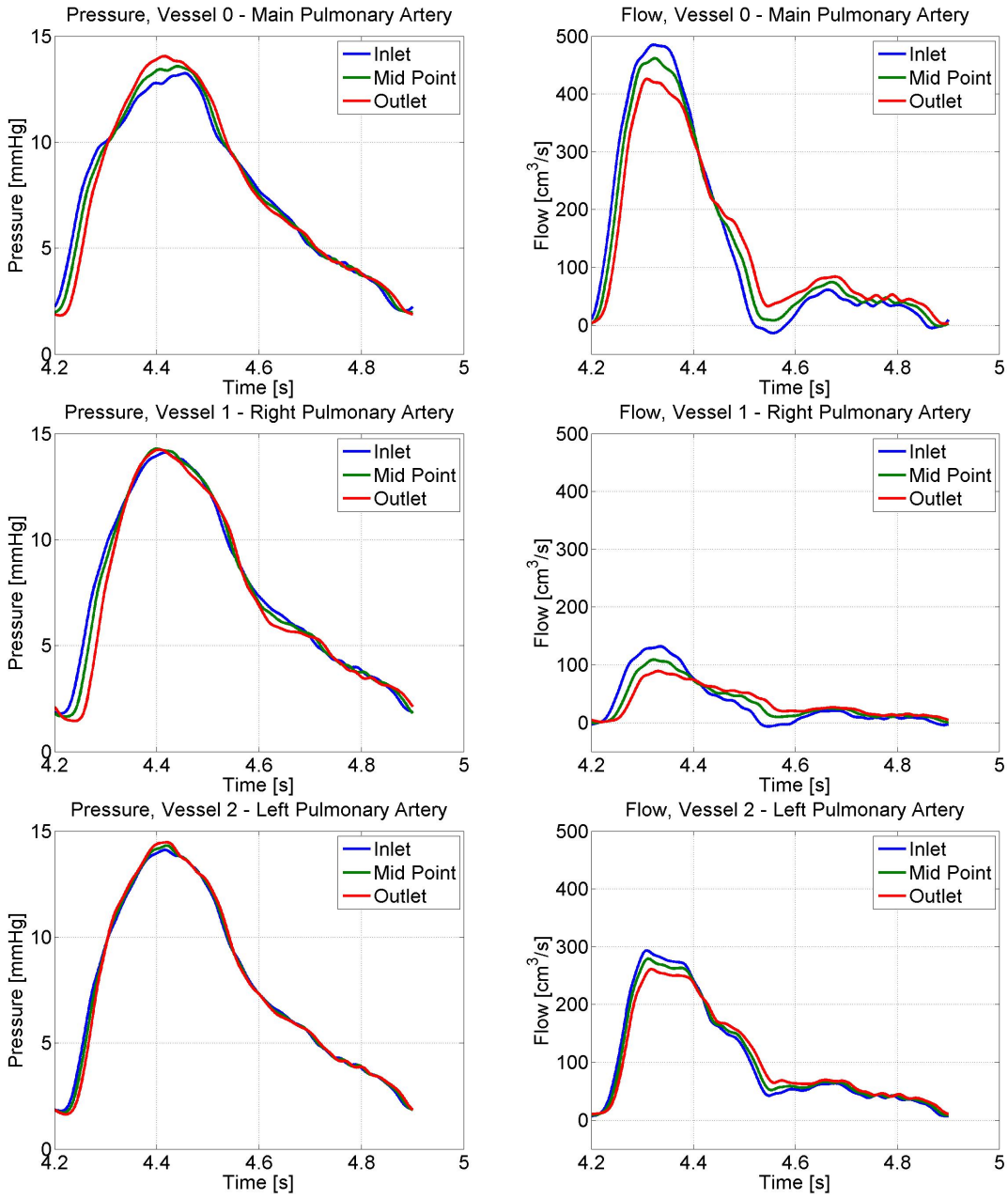

Figure 3.30: Predicted pressure and flow profiles in the Main Pulmonary Artery (Vessel 0 of Figure 3.25), the Right Pulmonary Artery (Vessel 1 of Figure 3.25), and the Left Pulmonary Artery (Vessel 2 of Figure 3.25). The flow split between Left and Right Pulmonary Arteries, with more flow to the larger vessel, is in agreement with observations by MRI [8], [9].

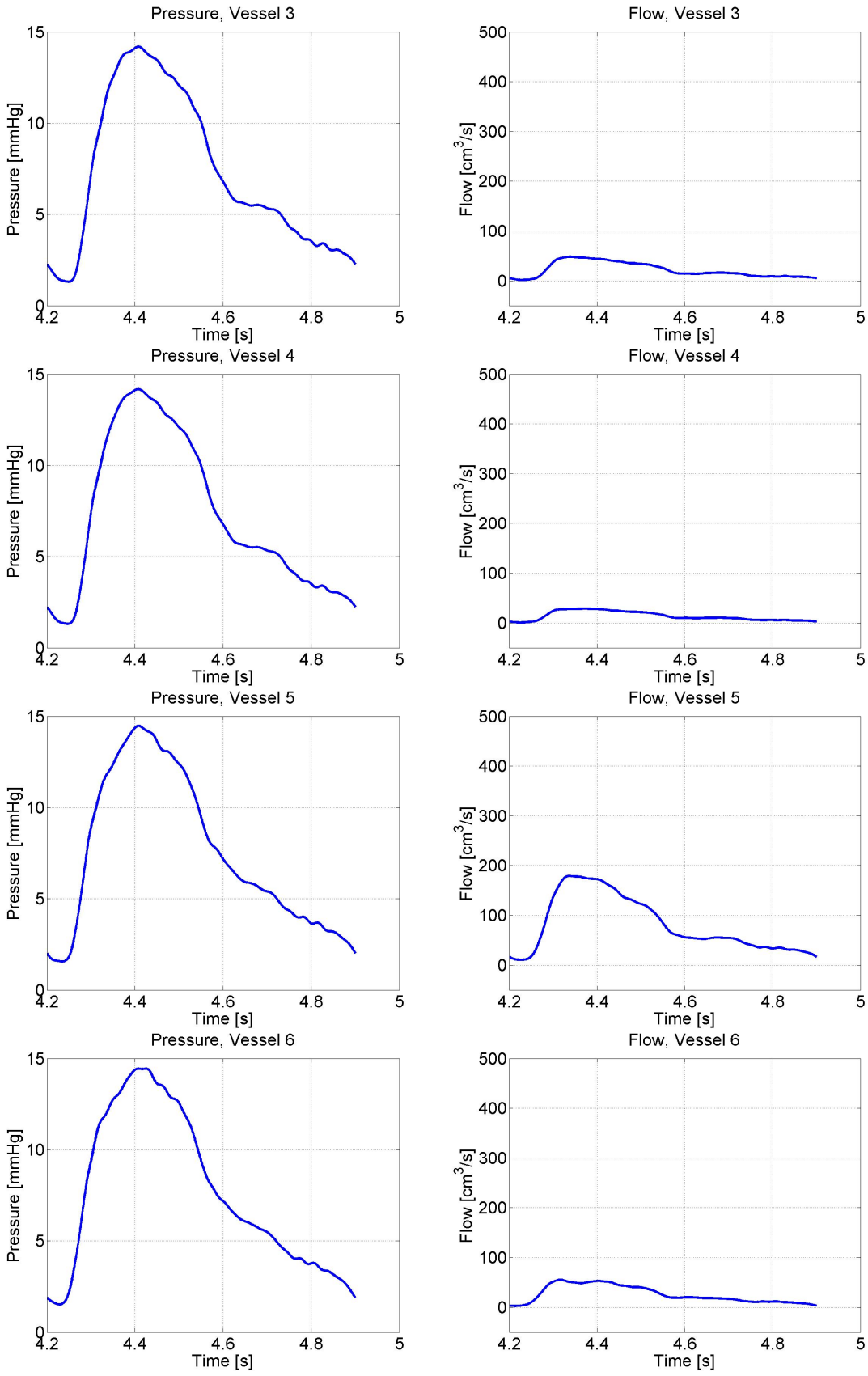

Figure 3.31: Flow and pressure profiles at outlets of terminal large arteries.

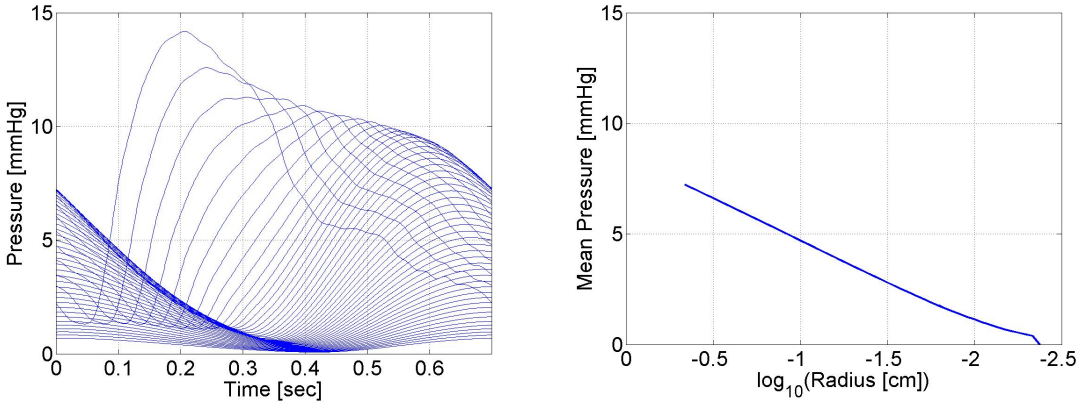

Figure 3.32: Pressure profiles and mean pressure with radius in the α branch.

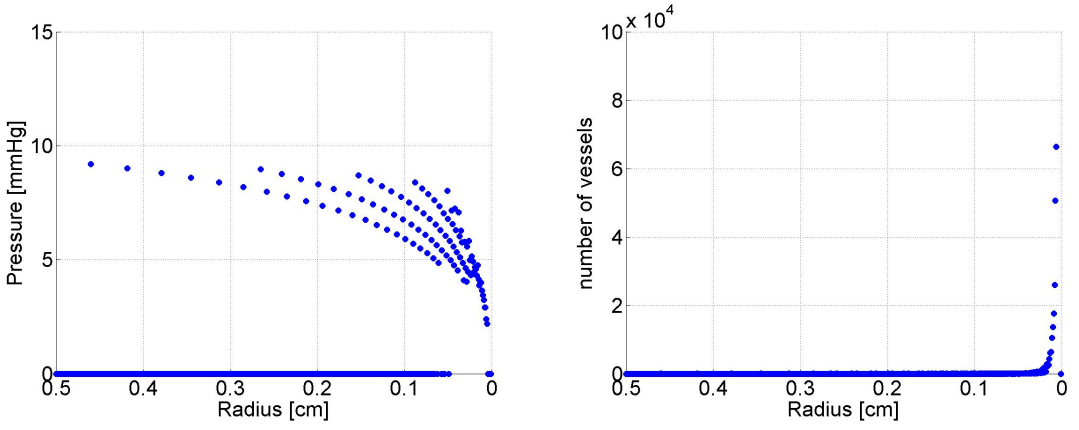

Figure 3.33: Mean pressures and number of vessels with radius in the structured tree of small pulmonary arteries.

Interpreting these results

The pulmonary arterial model provides qualitatively good predictions of the pressure pulse in the larger pulmonary arteries, as demonstrated in Figure 3.30. It is the unrealistically low predicted pressure, and the evidence of Figures 3.32 and 3.33, however, that suggests the inaccuracies of this model. The mean pressure can be seen to drop to zero at the end of the smallest vessels of the structured tree, as is inevitable given the zero-impedance outflow condition, but we will see later (Figure 5.1) that the pressure drop in the pulmonary circulation is more steady and occurs right across the arteries, capillaries and veins. This means that, while the peak and mean pressures predicted by this model seem accurate, it is likely that there is still information absent which would result from the influence of the pulmonary capillaries and veins, and which may have an effect on the shape of the arterial waveform as well as the peak and mean values.

Chapter 4

Joining an Arterial and Venous tree

In order to produce a model of the complete pulmonary circulation, we must first produce a method of joining together an arterial tree and a venous tree. To do this, we intend to replace Olufsen's structured tree outflow condition with a new model that is based on that model, but describe both a divergent, bifurcating arterial tree, and a confluent venous tree, with the two trees connected at their terminal vessels. Instead of providing an impedance as an outflow to a large arterial model, our new model will instead determine the admittance of a connected vascular network, taking the form of a 2×2 matrix, $\mathbf{Y}$, relating the pressure and flow at the outflow of a large artery (the root/inflow to the small arterial tree) to the pressure and flow at the inflow to a large vein (the root/outflow of the small venous tree) as shown in Figure 4.1.

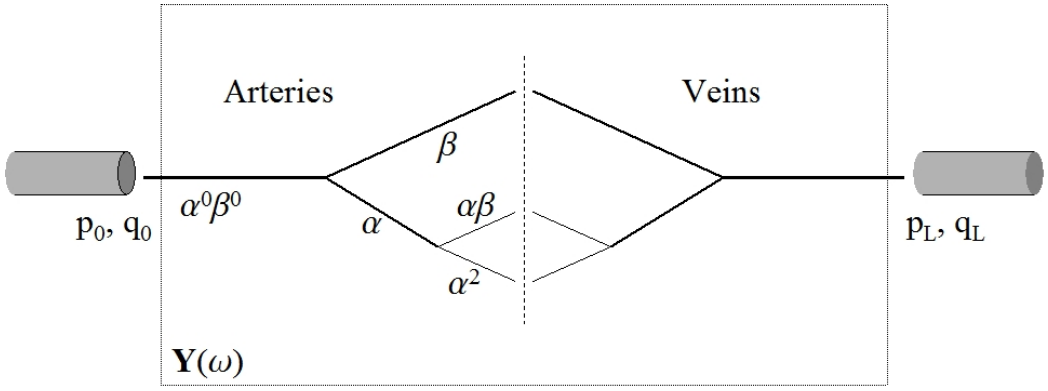

Figure 4.1: Linking an Arterial and Venous tree

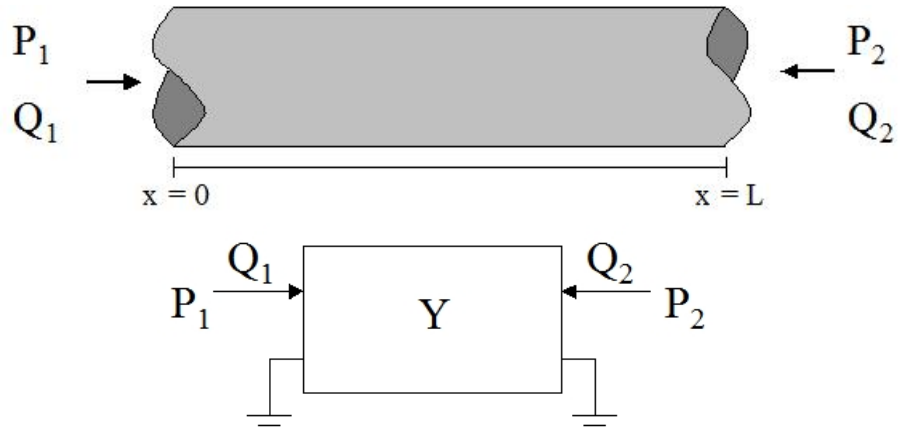

Figure 4.2: Single vessel segment. Flows Q_1 and Q_2 are in opposite directions.

4.1 Admittance matrix for a single vessel

Based on Olufsen's model for small arteries (Section 2.2), and Figure 4.2, the frequency domain flow and pressure at any distance point x along a vessel segment is

$$Q(x,\omega) = a\cos(\omega x/c) + b\sin(\omega x/c), \text{ and} \tag{4.1}$$

$$P(x,\omega) = (i/g_\omega)(-a\sin(\omega x/c) + b\cos(\omega x/c)), \tag{4.2}$$

where a and b are constants, ω is frequency and $g_\omega = \sqrt{CA_0(1-F_J)/\rho}$ (see Section 2.2 for further explanation of terms).

Vessel boundaries

Using the notation described in Figure 4.2, the flow and pressure at the beginning of a vessel segment, i.e. when $x = 0$, can be written as,

$$Q_1 = a, \text{ and} \tag{4.3}$$

$$P_1 = ib/g_\omega, \tag{4.4}$$

and at the end of a vessel segment, i.e.when $x = L$, the flow and pressure is,

$$Q_2 = -(a\cos(\omega L/c) + b\sin(\omega L/c)), \text{ and} \tag{4.5}$$

$$P_2 = (i/g_\omega)(-a\sin(\omega L/c) + b\cos(\omega L/c)). \tag{4.6}$$

So, in matrix form,

$$\begin{pmatrix} P_2 \\ Q_2 \end{pmatrix} = \begin{pmatrix} \cos(\omega L/c) & -(i/g_\omega)\sin(\omega L/c) \\ ig_\omega \sin(\omega L/c) & -\cos(\omega L/c) \end{pmatrix} \begin{pmatrix} P_1 \\ Q_1 \end{pmatrix}, \tag{4.7}$$

since

$$\begin{pmatrix} P_1 \\ Q_1 \end{pmatrix} = \begin{pmatrix} ib/g_\omega \\ a \end{pmatrix}. \tag{4.8}$$

Matrix form

By defining $C_L \equiv \cos(\omega L/c)$ and $S_L \equiv \sin(\omega L/c)$, we can write,

$$\begin{pmatrix} P_2 \\ Q_2 \end{pmatrix} = \begin{pmatrix} C_L & -iS_L/g_\omega \\ ig_\omega S_L & -C_L \end{pmatrix} \begin{pmatrix} P_1 \\ Q_1 \end{pmatrix} \tag{4.9}$$

or,

$$\begin{pmatrix} P_1 \\ Q_1 \end{pmatrix} = \begin{pmatrix} C_L & -iS_L/g_\omega \\ ig_\omega S_L & -C_L \end{pmatrix} \begin{pmatrix} P_2 \\ Q_2 \end{pmatrix}. \tag{4.10}$$

By rearranging, we can find that,

$$\begin{pmatrix} Q_1 \\ Q_2 \end{pmatrix} = \frac{ig_\omega}{S_L} \begin{pmatrix} -C_L & 1 \\ 1 & -C_L \end{pmatrix} \begin{pmatrix} P_1 \\ P_2 \end{pmatrix}, \tag{4.11}$$

meaning that

$$\mathbf{Y}(\omega) = \frac{ig_\omega}{S_L} \begin{pmatrix} -C_L & 1 \\ 1 & -C_L \end{pmatrix} \tag{4.12}$$

is the admittance matrix for $\omega \neq 0$ for any one artery or vein.

When $\omega = 0$ - the Zero frequency/DC component

From the linearised 1D axisymmetric momentum equation, equation (2.8), re-written as,

$$\frac{\partial u}{\partial t} + \frac{1}{\rho}\frac{\partial p}{\partial x} = \frac{\nu}{r}\frac{\partial}{\partial r}\left(r\frac{\partial u}{\partial r}\right), \tag{4.13}$$

we take Fourier expansions of fluid velocity, $u(r,x,t) = U(r,x)e^{i\omega t}$, and pressure, $p(x,t) = P(x)e^{i\omega t}$, so that (4.13) can be expressed as,

$$i\omega U + \frac{1}{\rho}\frac{dP}{dx} = \frac{\nu}{r}\frac{\partial}{\partial r}\left(r\frac{\partial U}{\partial r}\right), \tag{4.14}$$

i.e.

$$\frac{1}{\rho}\frac{dP}{dx} = \frac{\nu}{r}\frac{\partial}{\partial r}\left(r\frac{\partial U}{\partial r}\right) \tag{4.15}$$

since we are dealing with the case when $\omega = 0$, meaning that $i\omega U = 0$.

Now, $\nu = \mu/\rho$ and dP/dx is independent of r, so we can rearrange and integrate (4.15) with respect to r,

$$\frac{r^2}{2\mu}\frac{dP}{dx} + A = r\frac{\partial U}{\partial r} \tag{4.16}$$

$$\Rightarrow \frac{\partial U}{\partial r} = \frac{r}{2\mu}\frac{dP}{dx} + \frac{A}{r}, \tag{4.17}$$

where A is a constant of integration. However, since we know $\partial U/\partial r$ is finite at $r = 0$, $A = 0$ and we can further integrate (4.17) with respect to r again to find,

$$U = \frac{r^2}{4\mu}\frac{dP}{dx} + B, \tag{4.18}$$

where B is a constant. But the no-slip boundary condition tells us that fluid velocity $U = 0$ on the vessel walls $r = r_0$, so

$$U = \frac{r^2 - r_0^2}{4\mu}\frac{dP}{dx}. \tag{4.19}$$

Now we can find an expression for the Fourier expansion of the flow, $q(x,t) = Q(x)e^{i\omega t}$, in relation to the pressure P by integrating (4.19) over the cross-sectional area,

$$Q = 2\pi\int_0^{r_0} Ur\,dr \tag{4.20}$$

$$= \frac{2\pi}{4\mu}\int_0^{r_0} r(r^2 - r_0^2)\frac{dP}{dx}dr \tag{4.21}$$

$$= \frac{\pi}{2\mu}\frac{dP}{dx}\left[\frac{r_0^4}{4} - \frac{r_0^4}{2}\right] \tag{4.22}$$

$$= -\frac{\pi}{8\mu}\frac{dP}{dx}r_0^4. \tag{4.23}$$

Since we are dealing with steady flow, we know that $\partial q/\partial x = 0$, and continuity implies that $\partial q/\partial x = 0 \Leftrightarrow \partial Q/\partial x = 0$, meaning that we can write,

$$Q = \beta, \tag{4.24}$$

where β is a constant.

Therefore, substituting (4.24) into (4.23) and rearranging, we find that,

$$\frac{dP}{dx} = -\frac{8\mu\beta}{\pi r_0^4} \tag{4.25}$$

$$\Rightarrow P = -\frac{8\mu\beta}{\pi r_0^4}x + \gamma, \tag{4.26}$$

where β and γ are constants.

So we have,

$$Q_1 = \beta, \tag{4.27}$$

$$-Q_2 = \beta \text{ (sign convention, see Figure 4.2)}, \tag{4.28}$$

$$P_1 = \gamma, \text{ and} \tag{4.29}$$

$$P_2 = \gamma - 8\mu\beta L/\pi r_0^4. \tag{4.30}$$

Therefore,

$$\begin{pmatrix} P_2 \\ Q_2 \end{pmatrix} = \begin{pmatrix} 1 & -8\mu L/\pi r_0^4 \\ 0 & -1 \end{pmatrix} \begin{pmatrix} P_1 \\ Q_1 \end{pmatrix}, \tag{4.31}$$

and,

$$\begin{pmatrix} P_1 \\ Q_1 \end{pmatrix} = \begin{pmatrix} 1 & -8\mu L/\pi r_0^4 \\ 0 & -1 \end{pmatrix} \begin{pmatrix} P_2 \\ Q_2 \end{pmatrix}. \tag{4.32}$$

So,

$$\begin{pmatrix} Q_1 \\ Q_2 \end{pmatrix} = \frac{\pi r_0^4}{8\mu L} \begin{pmatrix} 1 & -1 \\ -1 & 1 \end{pmatrix} \begin{pmatrix} P_1 \\ P_2 \end{pmatrix}, \tag{4.33}$$

and

$$\mathbf{Y}(0) = \frac{\pi r_0^4}{8\mu L} \begin{pmatrix} 1 & -1 \\ -1 & 1 \end{pmatrix} \tag{4.34}$$

is the admittance matrix for $\omega = 0$ (DC component).

Non-dimensional admittance matrices

The frequency domain pressure and flow can be non-dimensionalised by,

$$P(x,\omega) = \rho g l \tilde{P}(x,\omega), \text{ and} \tag{4.35}$$

$$Q(x,\omega) = q_c \tilde{Q}(x,\omega), \tag{4.36}$$

where ρ is the density of blood, g is acceleration due to gravity, l is the characteristic length, q_c is the characteristic flow and $\tilde{P}$ and $\tilde{Q}$ are the non-dimensional pressure and flow respectively. This allows us to find the non-dimensional form of the admittance, $\tilde{Y}$, from its dimensional form through,

$$Y(x,\omega) = \frac{Q(x,\omega)}{P(x,\omega)} = \frac{q_c}{\rho g l} \frac{\tilde{Q}(x,\omega)}{\tilde{P}(x,\omega)} = \frac{q_c}{\rho g l} \tilde{Y}(x,\omega), \tag{4.37}$$

meaning that for $\omega \neq 0$, (4.11) becomes,

$$\begin{pmatrix} \tilde{Q}_1 \\ \tilde{Q}_2 \end{pmatrix} = \frac{i g_\omega}{S_L} \frac{\rho g l}{q_c} \begin{pmatrix} -C_L & 1 \\ 1 & -C_L \end{pmatrix} \begin{pmatrix} \tilde{P}_1 \\ \tilde{P}_2 \end{pmatrix}, \tag{4.38}$$

and for $\omega = 0$, (4.33) becomes,

$$\begin{pmatrix} \tilde{Q}_1 \\ \tilde{Q}_2 \end{pmatrix} = \frac{\rho g l}{q_c} \frac{\pi r_0^4}{8\mu L} \begin{pmatrix} 1 & -1 \\ -1 & 1 \end{pmatrix} \begin{pmatrix} \tilde{P}_1 \\ \tilde{P}_2 \end{pmatrix}, \tag{4.39}$$

meaning that

$$\tilde{\mathbf{Y}}(\omega) = \frac{i g_\omega}{S_L} \frac{\rho g l}{q_c} \begin{pmatrix} -C_L & 1 \\ 1 & -C_L \end{pmatrix} \tag{4.40}$$

and

$$\tilde{\mathbf{Y}}(0) = \frac{\rho g l}{q_c} \frac{\pi r_0^4}{8\mu L} \begin{pmatrix} 1 & -1 \\ -1 & 1 \end{pmatrix} \tag{4.41}$$

are the non dimensional admittance matrices for a single vessel for $\omega \neq 0$ and $\omega = 0$ respectively.

We shall from here on re-define

$$Q_i = \tilde{Q}_i,$$

$$P_i = \tilde{P}_i,$$

and

$$Y_{ij} = \tilde{Y_{ij}},$$

so that,

$$\begin{pmatrix} Q_1 \\ Q_2 \end{pmatrix} = \begin{pmatrix} Y_{11} & Y_{12} \\ Y_{21} & Y_{22} \end{pmatrix} \begin{pmatrix} P_1 \\ P_2 \end{pmatrix}, \tag{4.42}$$

where

$$\begin{aligned} Y_{11} &= -\frac{i g_\omega C_L}{S_L} \frac{\rho g l}{q_c}, \\ Y_{12} &= \frac{i g_\omega}{S_L} \frac{\rho g l}{q_c}, \\ Y_{21} &= \frac{i g_\omega}{S_L} \frac{\rho g l}{q_c}, \text{ and} \\ Y_{22} &= -\frac{i g_\omega C_L}{S_L} \frac{\rho g l}{q_c} \end{aligned}$$

for $\omega \neq 0$, or

$$\begin{aligned} Y_{11} &= \frac{\pi r_0^4}{8\mu l} \frac{\rho g l}{q_c}, \\ Y_{12} &= -\frac{\pi r_0^4}{8\mu l} \frac{\rho g l}{q_c}, \\ Y_{21} &= -\frac{\pi r_0^4}{8\mu l} \frac{\rho g l}{q_c}, \text{ and} \\ Y_{22} &= \frac{\pi r_0^4}{8\mu l} \frac{\rho g l}{q_c} \end{aligned}$$

for $\omega = 0$.

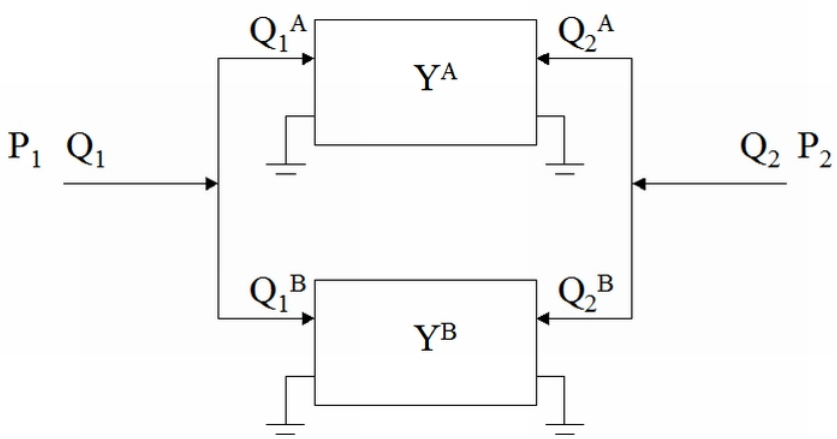

Figure 4.3: Two admittances in parallel.

4.2 Admittance Matrix for two vessels in parallel

We consider here two vessels, A and B, in parallel joined to a common inflow and outflow, as described in Figure 4.3. Since we know pressure is continuous across a bifurcation, the pressure at the inlet of vessel A is the same as the pressure at the inlet of vessel B, and the pressure at the outlet of vessel A is the same as the pressure at the outlet of vessel B. We call these inlet and outlet pressures P_1 and P_2 respectively, so that,

$$\begin{pmatrix} Q_1^A \\ Q_2^A \end{pmatrix} = \mathbf{Y}^A \begin{pmatrix} P_1 \\ P_2 \end{pmatrix}, \tag{4.43}$$

where Q_1^A and Q_2^A are, respectively, the inflow and outflow of vessel A, and $\mathbf{Y}^A$ is the admittance matrix for vessel A, and similarly

$$\begin{pmatrix} Q_1^B \\ Q_2^B \end{pmatrix} = \mathbf{Y}^B \begin{pmatrix} P_1 \\ P_2 \end{pmatrix}, \tag{4.44}$$

where Q_1^B, Q_2^B and $\mathbf{Y}^B$ are the inflow, outflow and admittance matrix for vessel B.

We further know that flow is conserved across a bifurcation, so for our two vessels connected in parallel, the total inflow $Q_1 = Q_1^A + Q_1^B$ and the total outflow $Q_2 = Q_2^A + Q_2^B$, meaning we can add the above equations to get,

$$\begin{pmatrix} Q_1 \\ Q_2 \end{pmatrix} = \begin{pmatrix} Q_1^A + Q_1^B \\ Q_2^A + Q_2^B \end{pmatrix} = \left(\mathbf{Y}^A + \mathbf{Y}^B\right) \begin{pmatrix} P_1 \\ P_2 \end{pmatrix}. \tag{4.45}$$

Thus

$$\mathbf{Y} = \mathbf{Y}^A + \mathbf{Y}^B \tag{4.46}$$

is the total admittance matrix for two vessels in parallel.

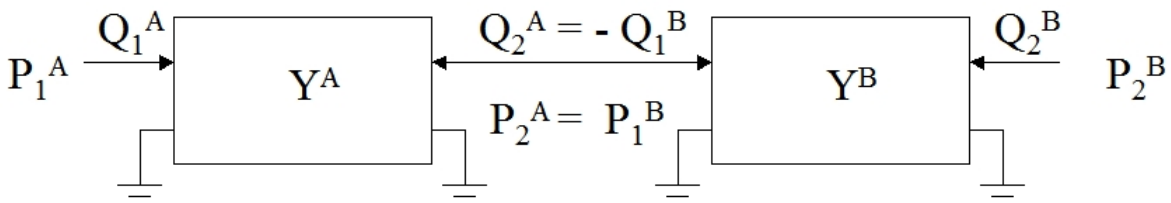

Figure 4.4: Two admittances connected in series.

4.3 Admittance matrix for two vessels in series

We shall now consider two vessels connected in series, as described in Figure 4.4. Using the notation in Figure 4.4,

$$Q_1^A = Y_{11}^A P_1^A + Y_{12}^A P_2^A, \tag{4.47}$$

$$Q_2^A = Y_{21}^A P_1^A + Y_{22}^A P_2^A, \tag{4.48}$$

$$Q_1^B = Y_{11}^B P_1^B + Y_{12}^B P_2^B, \text{ and} \tag{4.49}$$

$$Q_2^B = Y_{21}^B P_1^B + Y_{22}^B P_2^B. \tag{4.50}$$

Let $P = P_2^A = P_1^B$. Then we may solve for P from equations (4.48) and (4.49). Since $Q_2^A = -Q_1^B$,

$$Y_{21}^A P_1^A + Y_{22}^A P + Y_{11}^B P + Y_{12}^B P_2^B = 0, \tag{4.51}$$

so, by rearranging,

$$P = -\frac{Y_{21}^A P_1^A + Y_{12}^B P_2^B}{Y_{22}^A + Y_{11}^B}. \tag{4.52}$$

Substituting this result into equations (4.47) and (4.50), we get,

$$Q_1^A = \left(Y_{11}^A - \frac{Y_{21}^A Y_{12}^A}{Y_{22}^A + Y_{11}^B}\right) P_1^A - \frac{Y_{12}^A Y_{12}^B}{Y_{22}^A + Y_{11}^B} P_2^B, \text{ and} \tag{4.53}$$

$$Q_2^B = -\frac{Y_{21}^B Y_{21}^A}{Y_{22}^A + Y_{11}^B} P_1^A + \left(Y_{22}^B - \frac{Y_{21}^B Y_{12}^B}{Y_{22}^A + Y_{11}^B}\right) P_2^B. \tag{4.54}$$

Therefore,

$$\begin{pmatrix} Q_1^A \\ Q_2^B \end{pmatrix} = \mathbf{Y} \begin{pmatrix} P_1^A \\ P_2^A \end{pmatrix}, \tag{4.55}$$

where

$$\mathbf{Y} = \frac{1}{Y_{22}^A + Y_{11}^B} \begin{pmatrix} det(\mathbf{Y}^A) + Y_{11}^A Y_{11}^B & -Y_{12}^A Y_{12}^B \\ -Y_{21}^A Y_{21}^B & det(\mathbf{Y}^B) + Y_{22}^A Y_{22}^B \end{pmatrix} \tag{4.56}$$

is the admittance matrix for two vessels connected in series.

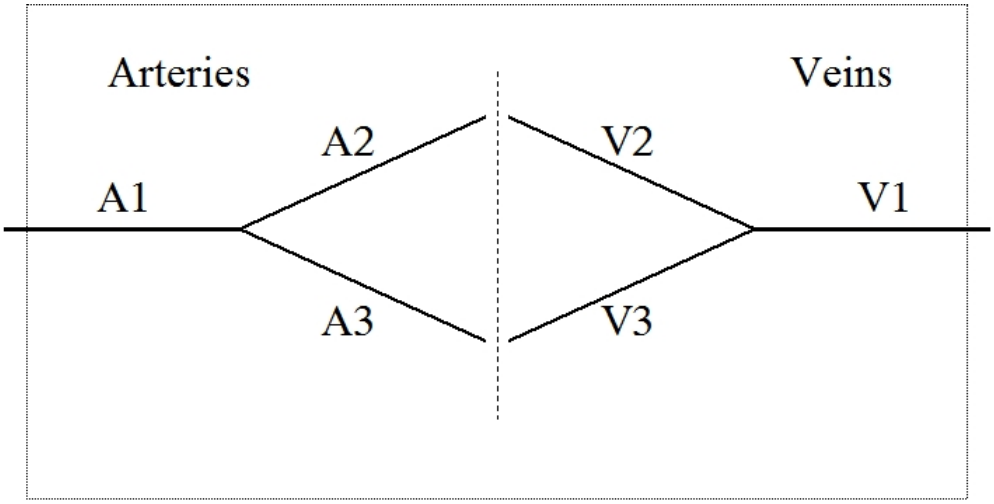

Figure 4.5: Simple example of back to back arterial and venous trees.

4.4 Linking an Arterial and Venous tree

We now have everything we need to compute the total admittance of a pair of back-to-back arterial and venous trees of any size. As with the original structured tree model, each tree is binary but generally asymmetric - the number of generations required to reach the terminal vessels varies with different paths. Topologically, the two trees are mirror images of each other - this is a requirement to ensure both trees have the same number of terminal vessels - but each vessel is allowed to have different properties from its image vessel in the other tree. This is important as arteries and veins generally have very different properties.

Every vessel in either tree is indexed with corresponding image vessels having the same index, but labelled as 'artery' or 'vein' as appropriate. For each indexed (pair of) vessel(s), two arrays are stored containing the indexes of said vessel's daughter vessels (one for left daughter vessels, one for right daughter vessels), or if it is a terminal vessel its entries in the arrays of daughter vessels are set to zero. Every terminal vessel in either tree connects to its image vessel in the other tree.

The admittance matrix for each individual vessel may be determined by (4.42), and the total admittance of the two connected trees can be found recursively by adding the admittance matrices of vessels and subtrees in series (using (4.56)) and in parallel (using (4.46)) as appropriate.

A simple example

To find the total admittance of the simple back-to-back arterial and venous trees described in Figure 4.5, one would begin by calculating the individual admittance matrices for each of the six individual vessels using (4.42). We then add the admittance matrix of each terminal vessel in series with that of its corresponding vessel in the other tree using (4.56), in this case vessels A2 and V2 are added in series, and vessels A3 and V3 are added in series to give a single admittance for each of the A2-V2 and A3-V3 branches.

Now, the A2-V2 and A3-V3 branches share parent vessels, and so the combined A2-V2 admittance can be added in parallel (using (4.46)) with the A3-V3 admittance to find the admittance matrix of the A2-V2-A3-V3 sub-tree.

Finally, by twice using (4.56), we add in series the admittance of vessel A1 with the A2-V2-A3-V3 sub-tree admittance, and this combined admittance is then added in series with the admittance of vessel V1 to find the total admittance of the system described in Figure 4.5.

Chapter 5

The Pulmonary Circulation Model

The pulmonary circulation differs from the systemic circulation in a number of ways, most notably in that the pulmonary circulation, unlike the systemic circulation, has a relatively pressurised venous system (see Figure 5.1) - that is flow through the pulmonary veins is driven by a pressure gradient, and there are no valves like there are in the systemic veins. This means that, whereas Olufsen's systemic model considered only the arterial side of the systemic circulation, for our model of the complete pulmonary circulation we wish to consider the venous side of the system, where there is still a measurable pressure pulse, and also the capillary network in between.

In Section 3.4, we adapted Olufsen's model to describe the arterial tree of the pulmonary circulation, and we will use the same description again to describe the large pulmonary arteries in our new model. It is also necessary to produce a description of the large pulmonary veins to describe the outflow of the pulmonary circulation draining into the left atrium of the heart. Finally, we will develop a new model to describe the connected network of both small arteries and small veins.

5.1 Large Pulmonary Arteries

The structural and elastic properties of the large pulmonary arteries, as well as the inflow into the main pulmonary artery, that were described in the production of the pulmonary arterial model in Section 3.4 will again be used to describe the large arterial section of our new pulmonary circulation model.

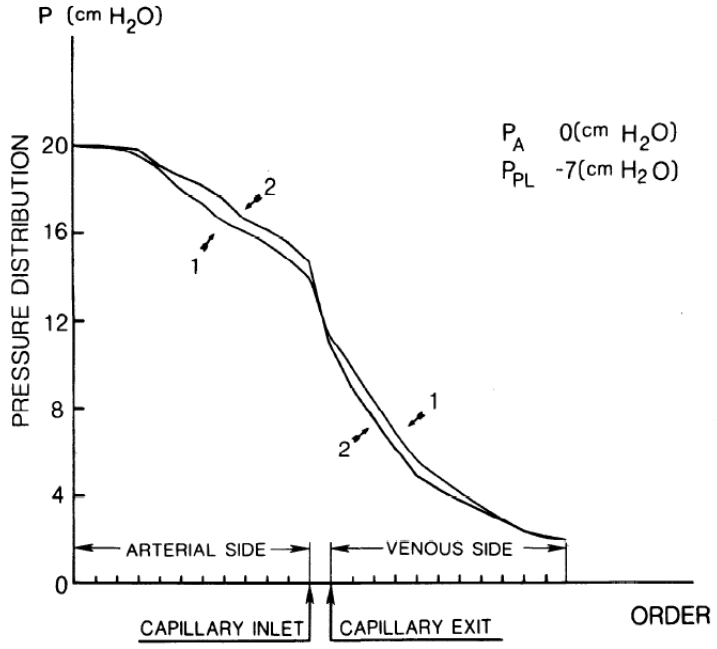

Figure 5.1: Longitudinal pressure distribution in pulmonary blood vessels, from Zhuang et al. [56], where P_A is airway pressure, P_{PL} is pleural pressure, and the numbers 1 and 2 refer to order numbering by generation, and by a Strahler method respectively (see Appendix B).

5.2 Large Pulmonary Veins

The large pulmonary veins will be described in an identical manner to the large arteries - a tree of large vessels with an 'outflow' condition at the opening of the largest vein (equivalent to the inflow condition to the large arteries), 'inflow' conditions at the ends of the terminal vessels (equivalent to the outflow conditions of the large arteries), and identical bifurcation conditions as for the arterial tree. Since the pulmonary veins are known to follow closely the course of the pulmonary arteries, we have described the large pulmonary venous tree simply as a mirror image of the arterial tree described in Figure 3.25. The diameters and lengths of these vessels also fall within the range suggested by the data of Huang et al. [21].

Outflow Condition

The outflow condition to our large pulmonary veins, applied at the opening of the largest pulmonary vein, is also the outflow condition of our full pulmonary circulation model, and describes the return flow of blood from the pulmonary veins to the left atrium of the heart.

Whereas at the inflow to the pulmonary arteries we prescribed an imposed flow profile condition, at the outflow of the pulmonary veins we shall prescribe an imposed pressure condition. Since this condition is imposed at a position immediately above where blood drains relatively freely into the left atrium, we believe that setting the pressure to be a very low value, or zero at this point is a reasonable outflow condition for our model (as suggested in Figure 5.1). This also ensures a pressure gradient right across the pulmonary circulation to drive the flow of blood.

Elastic Properties

In the absence of extensive data on the elastic properties of the pulmonary veins, it has been suggested to us by our clinical collaborators that the compliance of the pulmonary veins need not differ much from that of the systemic veins, on which there has been collected suitable data [26], [49]. The justification for this is that the blood passing through both the systemic and pulmonary veins do so at similarly low pressures.

Figure 5.2 summarises a fit to data collected by Stooker at al in 2003 [49] on pressure-diameter relationships in the human greater saphenous vein, which is often used in bypass

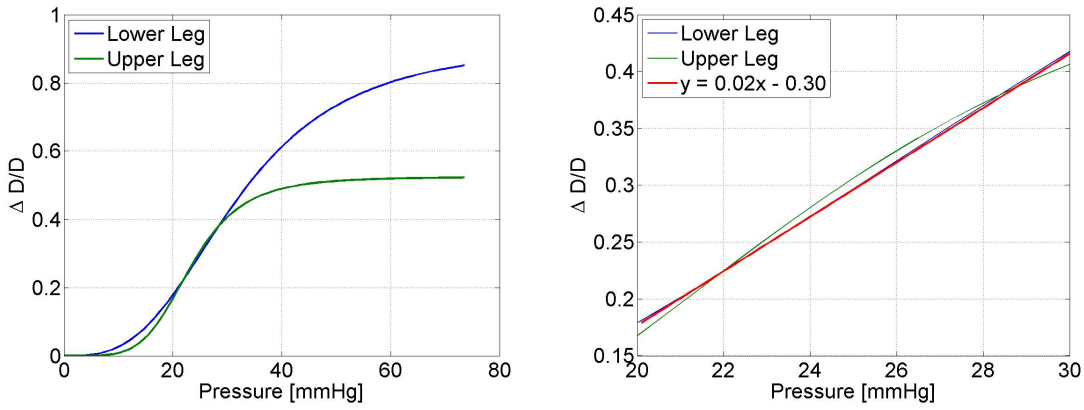

Figure 5.2: Pressure vs fractional change in diameter. Data from Stooker et al [49].

surgery. They plotted the fractional change in diameter against pressure for two regions of the greater saphenous vein - in the lower leg and in the upper leg respectively - and this plot is recreated in the left graph of Figure 5.2. The gradient of the pressure-diameter relations plotted in Figure 5.2 is equivalent to the distensibility parameter α described in Section 3.4 for the pulmonary arteries.

The diameter of the greater saphenous vein is generally larger than that of the pulmonary veins, and we believe it is reasonable to assume that in regions of low pressure ($p < 10 - 20$mmHg) in Figure 5.2 the vein may be deformed due to collapsing, and in regions of high pressure ($p > 30 - 40$mmHg) the vein may be deformed by being over stretched. The intermediate region of interest, where we believe the vein is undeformed, is what we use to derive our stiffness properties for the pulmonary veins.

The $p \sim 20 - 30$mmHg region of interest is expanded in the right graph of Figure 5.2, and it can be seen that in both the upper and lower leg the pressure-diameter relations coincide and are roughly linear. Fitting a straight line to this region yields a gradient, and thus distensibility parameter, of 0.02/mmHg - exactly the same as was found for the pulmonary arteries in Section 3.4. This is perhaps not surprising as the region of interest of pressure we derived this from - $p \sim 20 - 30$mmHg - is approximately the same as the peak pressures seen in the pulmonary arteries.

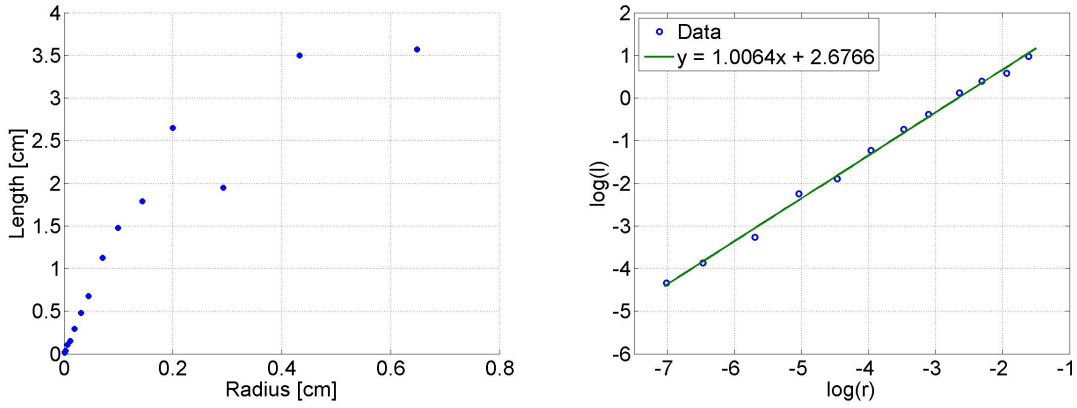

Figure 5.3: Vessel radius vs length for pulmonary veins, data from Huang et. al. [21].

5.3 Small Vessel Structure

The small vessels of the pulmonary circulation will be modelled as a back-to-back pair of arterial and venous structured trees, as described in the previous chapter. This provides us with an admittance matrix relating pressure an flow at the outflow points of the large arterial model to the pressure and flow at the inflow points of the large venous model.

The properties of the small pulmonary arteries (lengths, radii, stiffness) were described in the production of the pulmonary arterial model in Section 3.4, and the same description will be used here. The small pulmonary veins, however, have different properties to the arteries, and so further description is required.

It is a requirement of our algorithm for joining arterial and venous trees that the two back-to-back trees be topologically mirror images of each other. This means that the parameters which govern the branching nature of the structured tree - the branching exponent, and area and asymmetry ratios - must be identical for the arterial and venous trees. Further, the top and bottom radii of each vessel in each tree must match that of its image in the other tree. The vessel length (as a function of its radius) and wall stiffness, however, can be varied for the different trees.

Huang et al, 1996 [21] provide data on the average lengths and radii of vessels across the 15 orders of the pulmonary venous tree, as summarised in the left graph of Figure 5.3. As we did with the pulmonary arteries in Section 3.4, we ignore the data for the largest three orders of the pulmonary venous trees, as these three largest generations are described explicitly in our model of the large pulmonary veins. A log-log fit of the data for the remaining 12 orders, as seen in the right graph of Figure 5.3, suggests a length-to-radius

relation of

$$l = e^{2.68} r^{1.00} = 14.54r \tag{5.1}$$

for all pulmonary veins of radius $r < 0.200$cm.

5.4 Incorporating into the numerical scheme

We continue to use the two-step Lax-Wendroff scheme to solve for flow and pressure in our new pulmonary model. We again use a prescribed flow profile, given by Figure 3.26, as our inflow condition, and similarly now use a prescribed pressure profile as our outflow condition. This outflow pressure is set to be zero for all time for this model, but could be set to any prescribed pressure-time profile. Details of how these are incorporated into the numerical scheme are given in A.1 and A.4 of Appendix A respectively.

The bifurcation conditions are identical as for the systemic arterial model, but we now require a new matching boundary condition at the terminals of the large pulmonary arteries and veins respectively. This condition is derived from the admittance matrix described in Chapter 4 which states that,

$$\begin{pmatrix} Q_A(L,\omega) \\ Q_V(0,\omega) \end{pmatrix} = \begin{pmatrix} Y_{11}(\omega) & Y_{12}(\omega) \\ Y_{21}(\omega) & Y_{22}(\omega) \end{pmatrix} \begin{pmatrix} P_A(L,\omega) \\ P_V(0,\omega) \end{pmatrix},$$

where $Q_A(L,\omega)$ and $P_A(L,\omega)$, and $Q_V(0,\omega)$ and $P_V(0,\omega)$ are the frequency domain flows and pressures at the ends of the terminal arteries and veins respectively.

Transforming this to the time domain using convolutions gives,

$$q_A(L,t) = \int_0^T \left(p_A(L,t-\tau)y_{11}(\tau) + p_V(0,t-\tau)y_{12}(\tau)\right) d\tau, \text{ and} \tag{5.2}$$

$$q_V(0,t) = \int_0^T \left(p_A(L,t-\tau)y_{21}(\tau) + p_V(0,t-\tau)y_{22}(\tau)\right) d\tau, \tag{5.3}$$

which are the matching boundary conditions to be applied at the end of terminal arteries and veins respectively. Details of how this is incorporated into the numerical scheme are given in A.3 of Appendix A.

Chapter 6

Validation and Applications of the Pulmonary Circulation Model

Figure 6.1 shows predicted pressure profiles, as well as peak, trough, pulse and mean pressures in the main pulmonary artery (Vessel 0 of Figure 3.25) for a range of values of the minimum radius, r_{min}, in arterial and venous structured trees. Figure 6.2 shows the predicted pressures profiles for the right and left pulmonary arteries for the same range of values of r_{min}.

A minimum radius value of $r_{min} = 0.001$cm, as used in the pulmonary arterial model in Section 3.4, results in the highest pressure predictions in Figures 6.1 and 6.2, with peak pressures around 70mmHg. Clearly this is much higher than realistic values that would be expected in the large pulmonary arteries, and so we choose $r_{min} = 0.005$cm, which predicts more realistic pressures, for what we consider 'normal' conditions in our model.

The justification for choosing $r_{min} = 0.005$cm comes from equations (3.34) and (3.35), and Figure 3.27 of Section 3.4. These suggest that the length-to-radius relation of vessels in the small pulmonary arteries changes at this point, implying that vessels smaller than this value are arterioles with different properties to the larger arteries (that control the flow of blood into the pulmonary capillaries), or the pulmonary capillaries themselves. In the absence of a capillary model (see Chapter 7), we therefore choose to terminate our structured tree above this level.

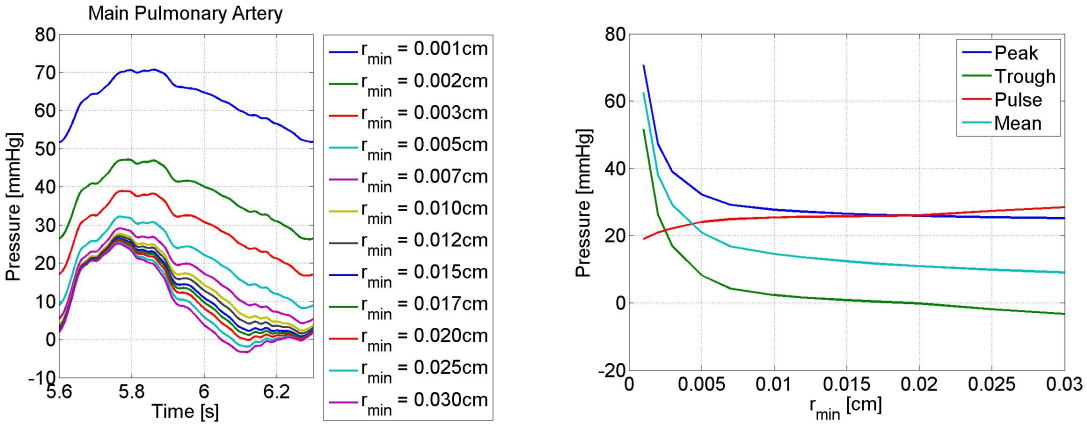

Figure 6.1: Predicted pressures in the Main Pulmonary Artery.

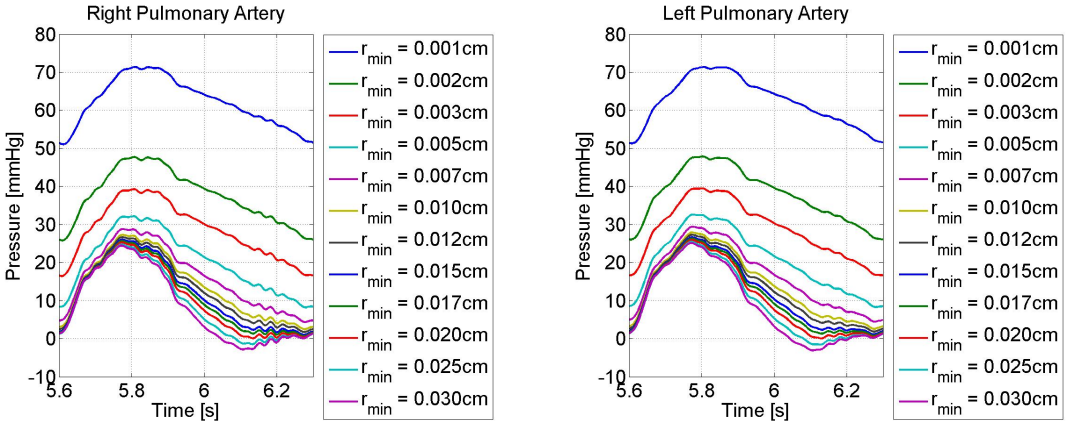

Figure 6.2: Predicted pressures in the Right and Left Pulmonary Arteries.

6.1 Normal Physiological Conditions

Having determined what constitutes normal conditions in our model, Figure 6.3 shows the predicted flows and pressure in the main, left and right pulmonary arteries under these conditions. Similarly, Figure 6.4 shows the predicted flows and pressures in the main, left and right pulmonary veins (i.e. the veins that are the image of the three largest pulmonary arteries, see Chapters 5 and 7).

The magnitude and shape of the predicted pulmonary artery pressure and flow waveforms are in good agreement with clinical measurements [27] (left hand graphs of Figure 6.5).

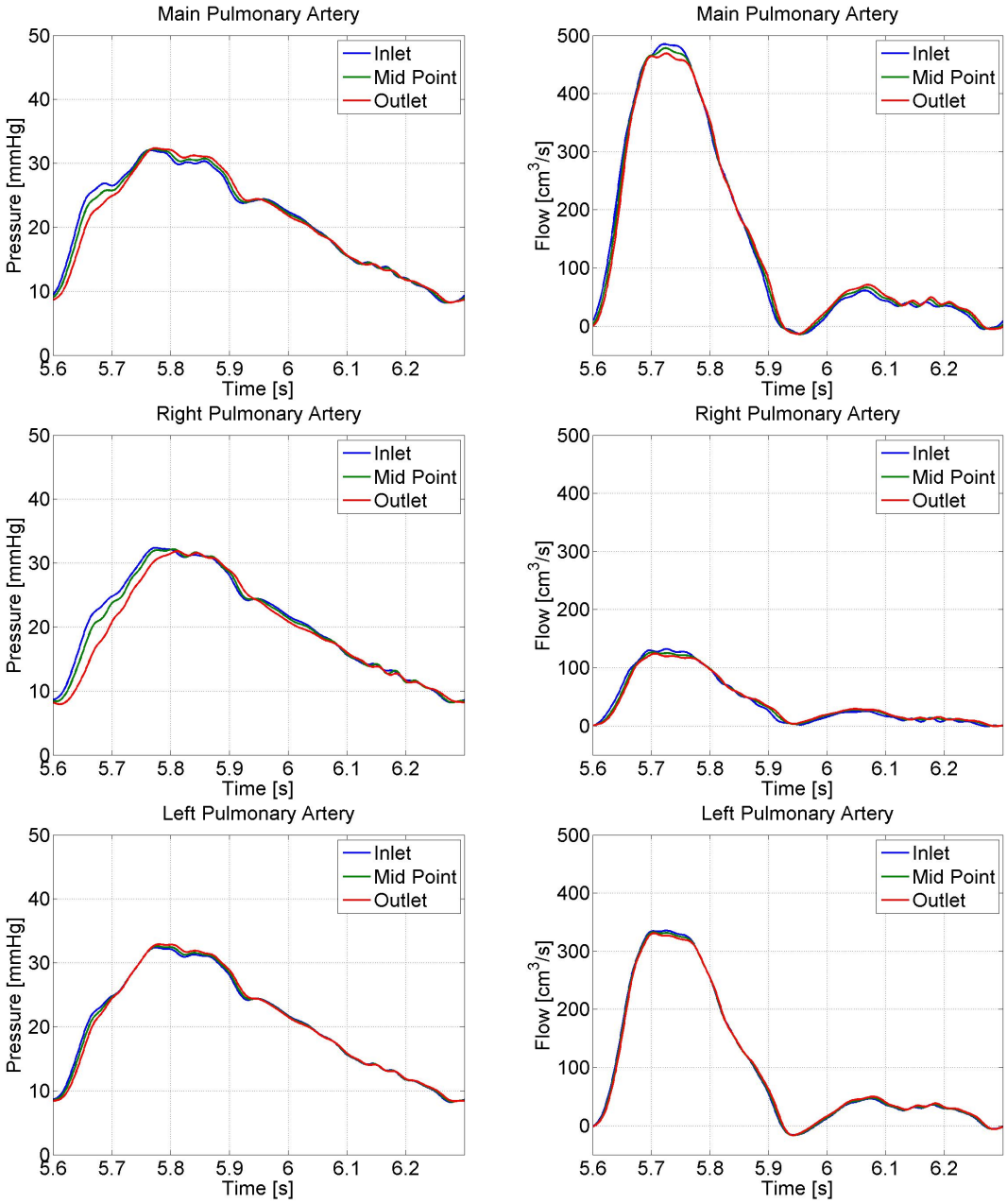

Figure 6.3: Predicted pressure and flow profiles in Main, Right and Left Pulmonary Arteries.

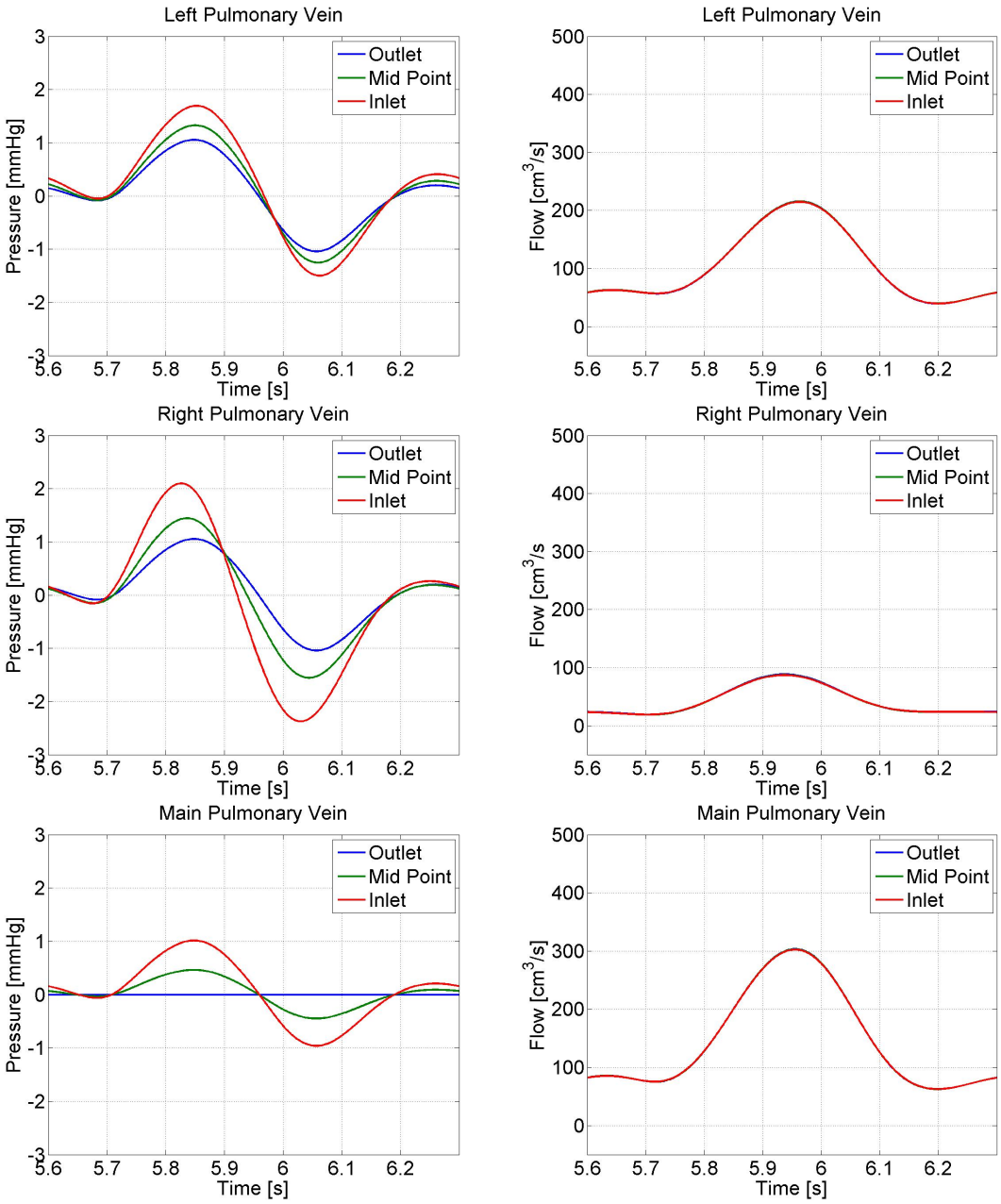

Figure 6.4: Predicted pressure and flow profiles in Left, Right and Main Pulmonary Veins.

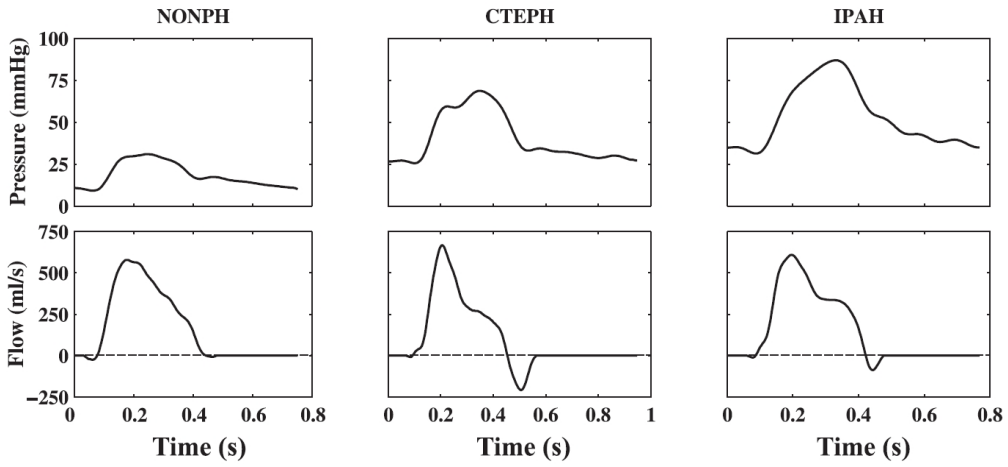

Figure 6.5: Measured pulmonary artery pressure and flow waveforms. NONPH - Normal Physiological Conditions, CTEPH - Chronic Thromboembolic Pulmonary Hypertension, IPAH - Idiopathic Pulmonary Arterial Hypertension. From Lankhaar et al. [27].

6.2 Pulmonary Hypertension

Pulmonary hypertension is a rare condition which can have grave consequences for those affected. The condition may arise as the result of multiple mechanisms, and as a result can be divided into a number of clinical classifications [36], [45],

- **Group I - Pulmonary Arterial Hypertension** - in this group of conditions, the pathophysiology is located in pulmonary arteries and arterioles of less than 0.050cm diameter, with increased stiffness and resistance in the smaller vessels [27], [43].
- **Group II - Pulmonary Venous Hypertension** - here, the pulmonary arteries are normal, but failure of the left heart to pump blood efficiently leads high pressure in the left atrium, pooling of blood in the lungs and distended pulmonary veins [45]
- **Group III - Pulmonary Hypertension in association with hypoxic lung disease** - this group includes conditions that involve pulmonary vascular remodelling (typically affecting vessels of less than 0.050cm diameter) and loss of the pulmonary vascular bed (vascular rarefaction) due to underlying respiratory disease [51].
- **Group IV - Chronic Thromboembolic Pulmonary Hypertension** - here, the problem is initially located in larger vessels with increased stiffness and decreased cross-sectional area. Eventually there may be involvement of the small vessels in the same way as Pulmonary Arterial Hypertension [7], [11].

6.2.1 Pulmonary Arterial Hypertension

Pulmonary arterial hypertension may have a variety of causes [4], but an underlying feature of the condition is the stiffening of the smaller pulmonary arteries [43]. Reeves et. al. [43] showed that the distensibility parameter α (see Section 3.4) decreased in chronic hypoxia and with ageing, resulting in the stiffening of vessels.

As we did in Section 3.1 for the systemic arteries, we model this reduction in distensibility by increasing the stiffness parameter Eh/r_0, which is inversely proportional to the distensibility parameter α (see equation (3.44)).

Results

Figure 6.6 shows the effects of increased small vessel stiffness on predicted pressures in the three largest pulmonary arteries. We see that increasing the stiffness parameter leads to an increase in peak and pulse pressure. We also see that peaking of the pressure wave occurs slightly later in instances of stiffer small arteries, and that a local minimum visible shortly after the main peak disappears when the small vessels are stiffened. This is in good agreement with the observations of Lankhaar et. al. [27] (right hand graphs of Figure 6.5) in cases of idiopathic pulmonary hypertension compared to no pulmonary hypertension (control).

Figures 6.7, 6.8 and 6.9 show the effects of stiffening the small pulmonary arteries (and thus mimicking the hypothesis behind pulmonary arterial hypertension) on pulmonary arterial flow, pulmonary venous pressure and pulmonary venous flow respectively. Little effect is seen on the pulmonary arterial flow, while the stiffening of the small arteries causes an increase in the amplitude of oscillation of the pulmonary venous pressure and flow waveforms.

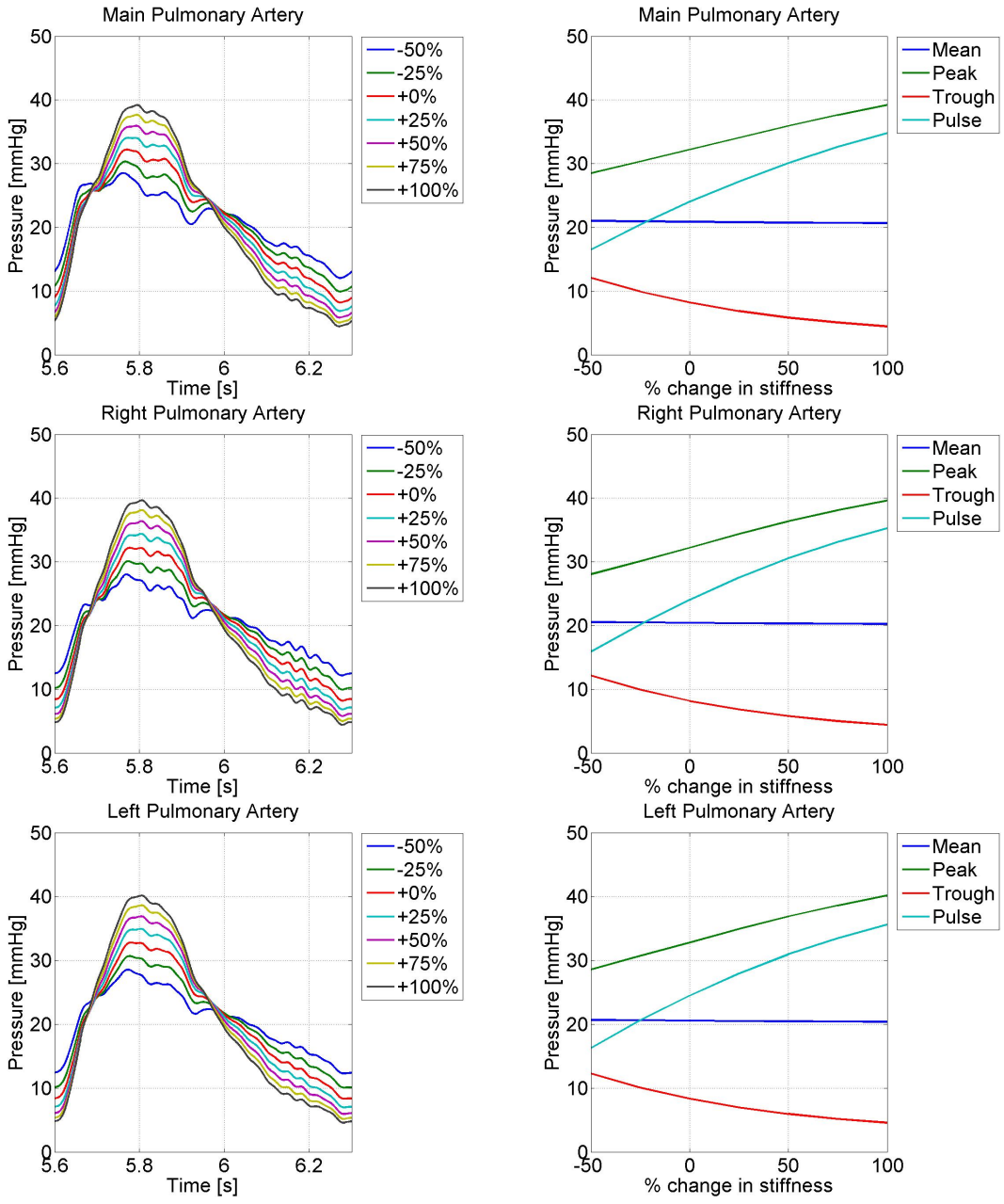

Figure 6.6: Effects of changing small vessel compliance on Pulmonary Artery Pressure.

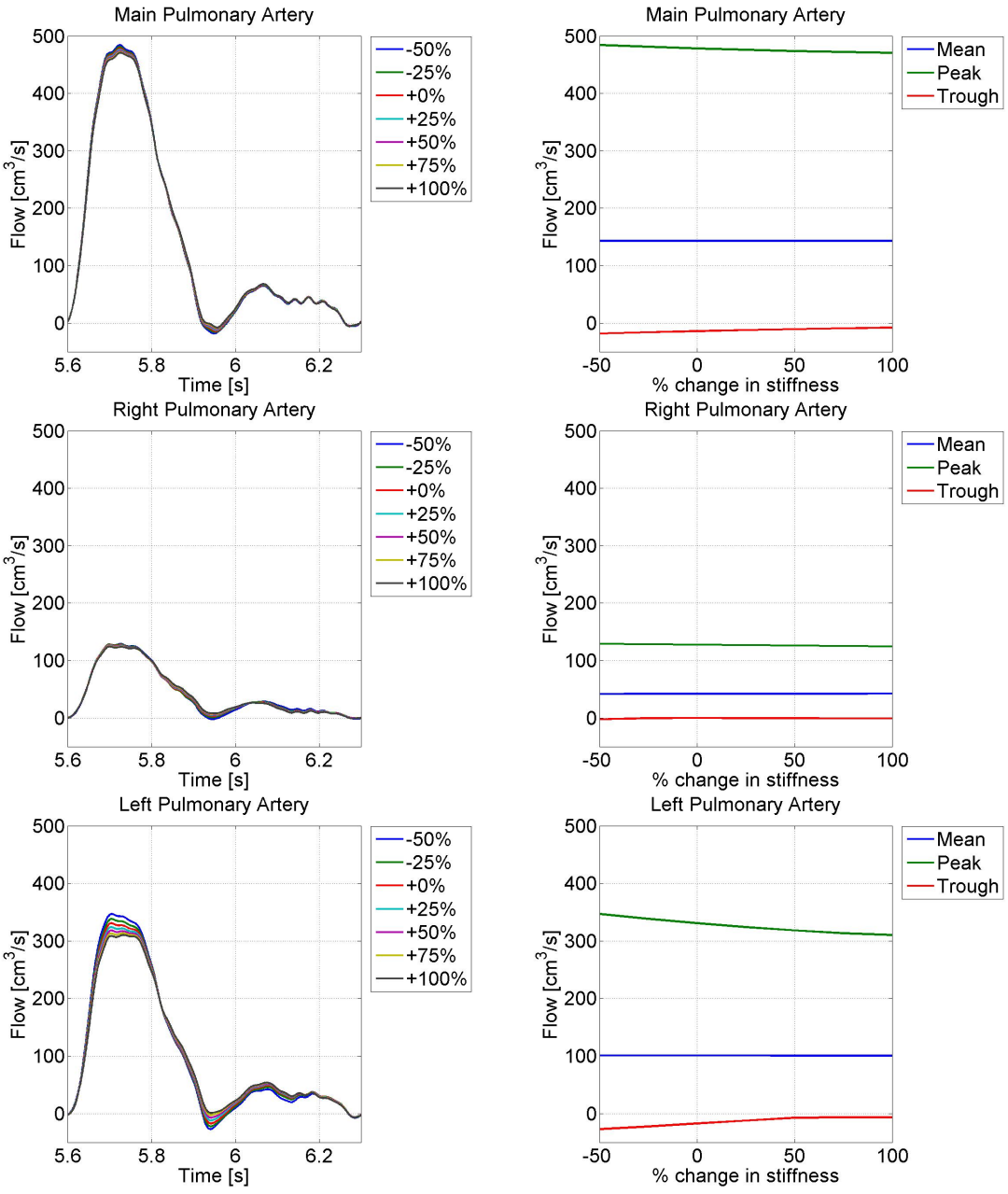

Figure 6.7: Effects of changing small vessel compliance on Pulmonary Artery Flow.

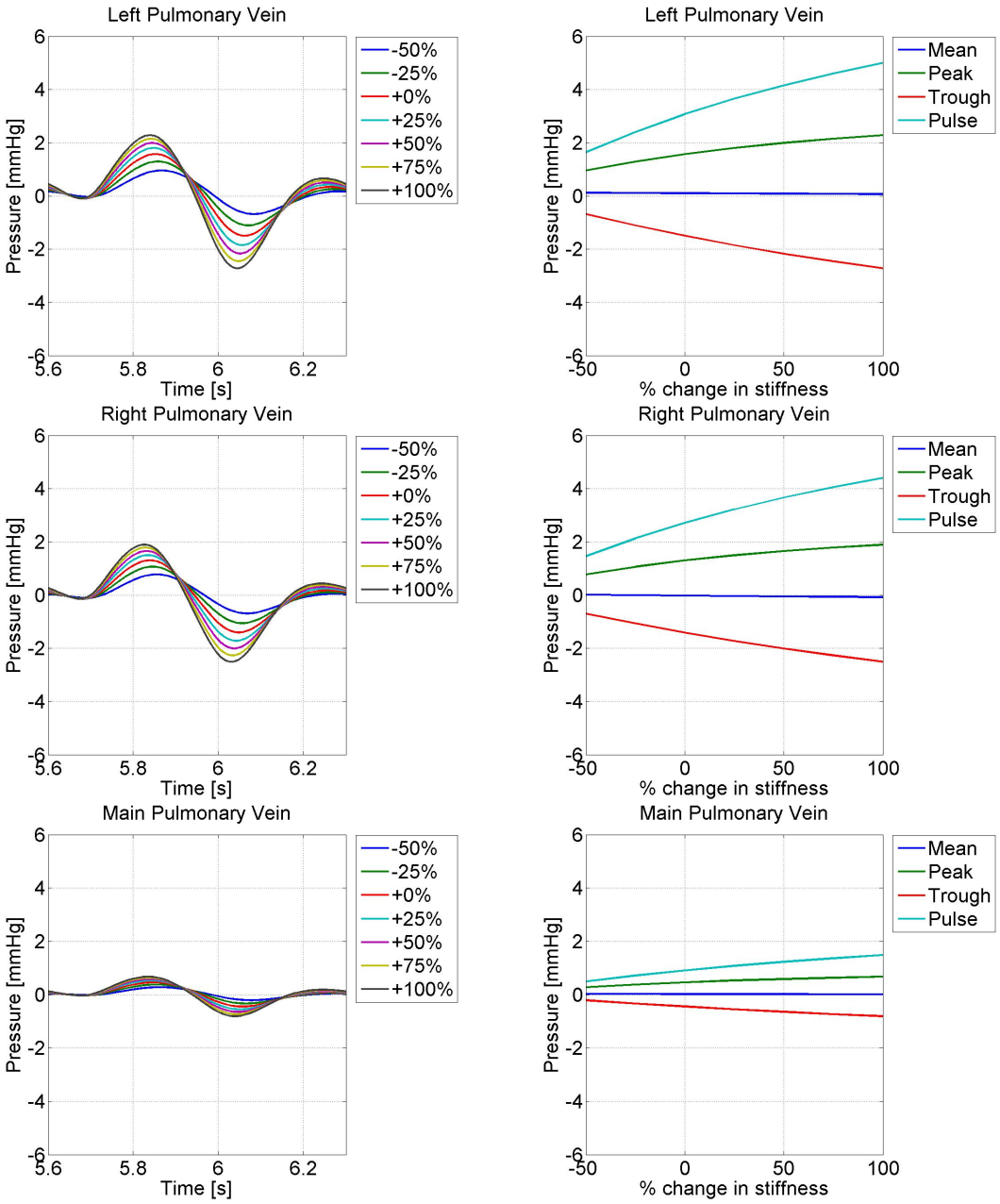

Figure 6.8: Effects of changing small vessel compliance on Pulmonary Venous Pressure.

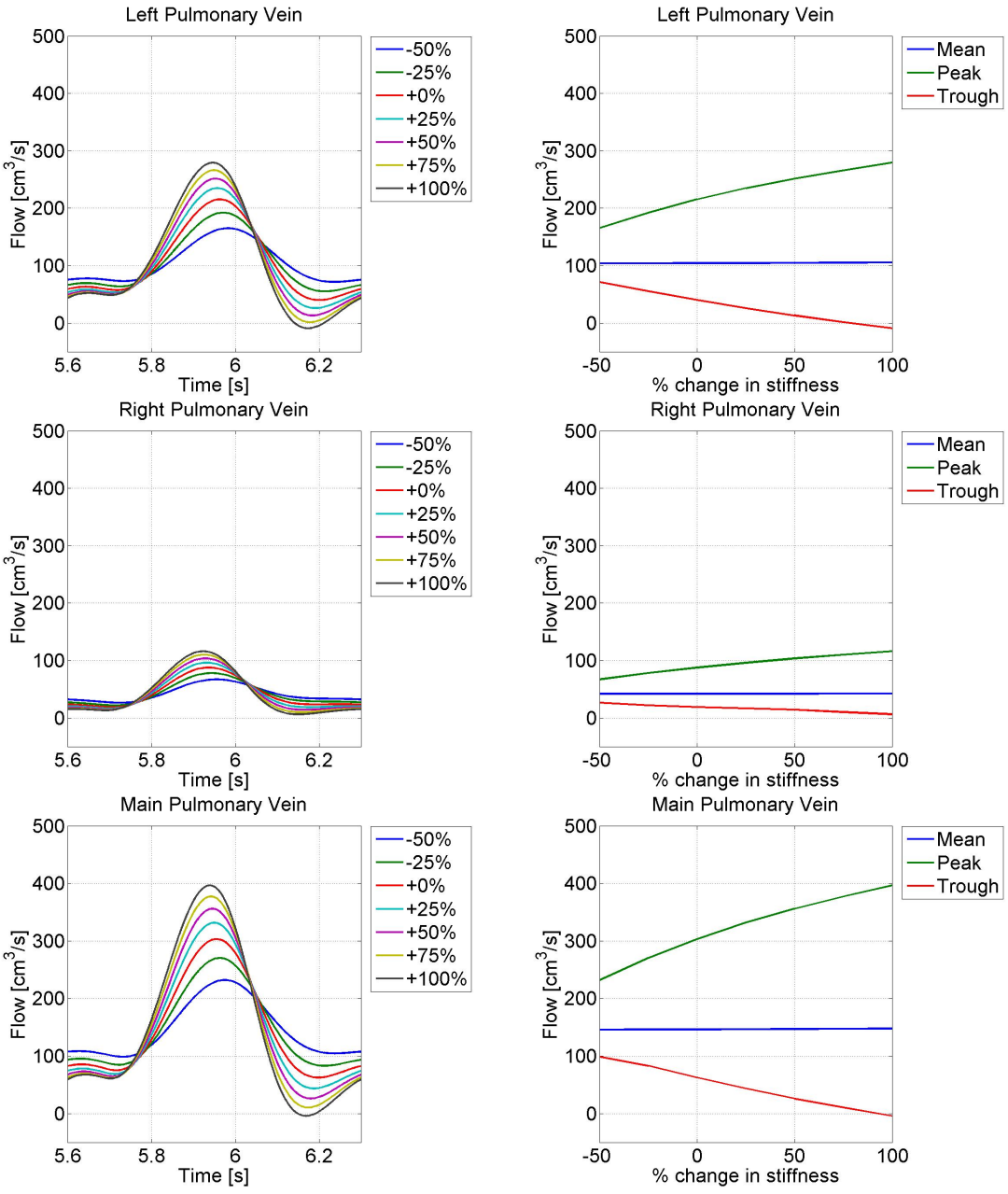

Figure 6.9: Effects of changing small vessel compliance on Pulmonary Venous Flow.

6.2.2 Pulmonary Venous Hypertension

Pulmonary venous hypertension may be more a condition of the left heart than of the lungs [45]. The inability of the left heart to pump blood efficiently results in a build up in pressure in the pulmonary veins. Since our outflow condition describing venous return to the left atrium in our pulmonary model is a prescribed pressure condition, we may simulate this build up in pressure by simply increasing our prescribed pressure value at the outlet of the largest pulmonary vein.

Results

Figure 6.10 shows predicted pressure profiles in the largest pulmonary arteries, for venous boundary pressures ranging from -5mmHg to +35mmHg. Almost no effect is seen on the shape of the pressure profile, it is simply shifted up the pressure axis with increased venous boundary pressure. Similarly, mean pressure increases in proportion with the increase in venous boundary pressure, while pulse pressure drops very slightly at higher pressures. The same results are seen in Figure 6.12 for pulmonary venous pressure - shifting of the pressure profile and an increase in mean pressure in proportion with the increase in boundary pressure.

Figure 6.11 shows little or no effect of changing venous pressure on pulmonary arterial flow, while Figure 6.13 shows a slight reduction in amplitude of the pulmonary venous flow with increased venous pressure.

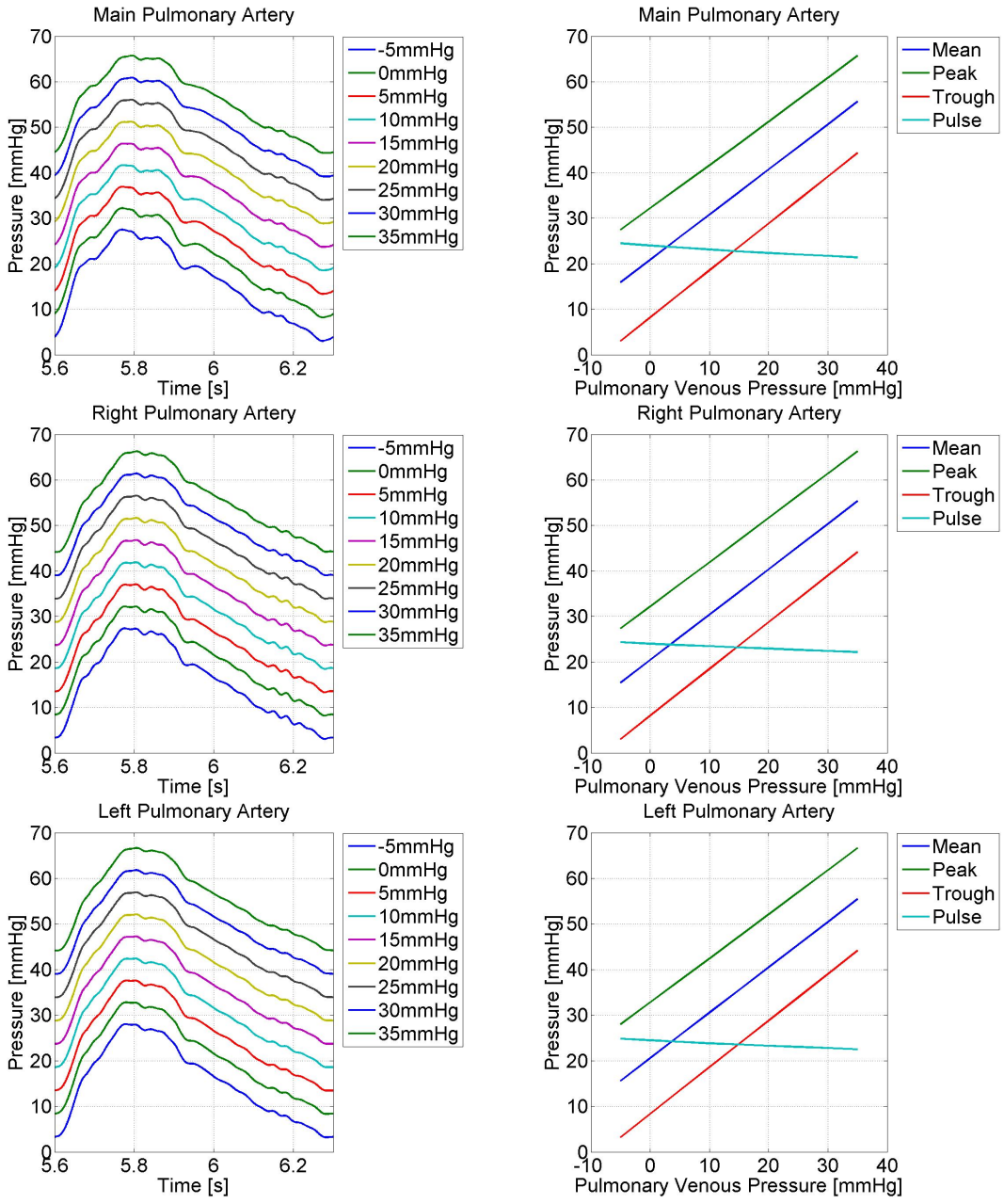

Figure 6.10: Effects of pulmonary venous hypertension on pulmonary arterial pressure.

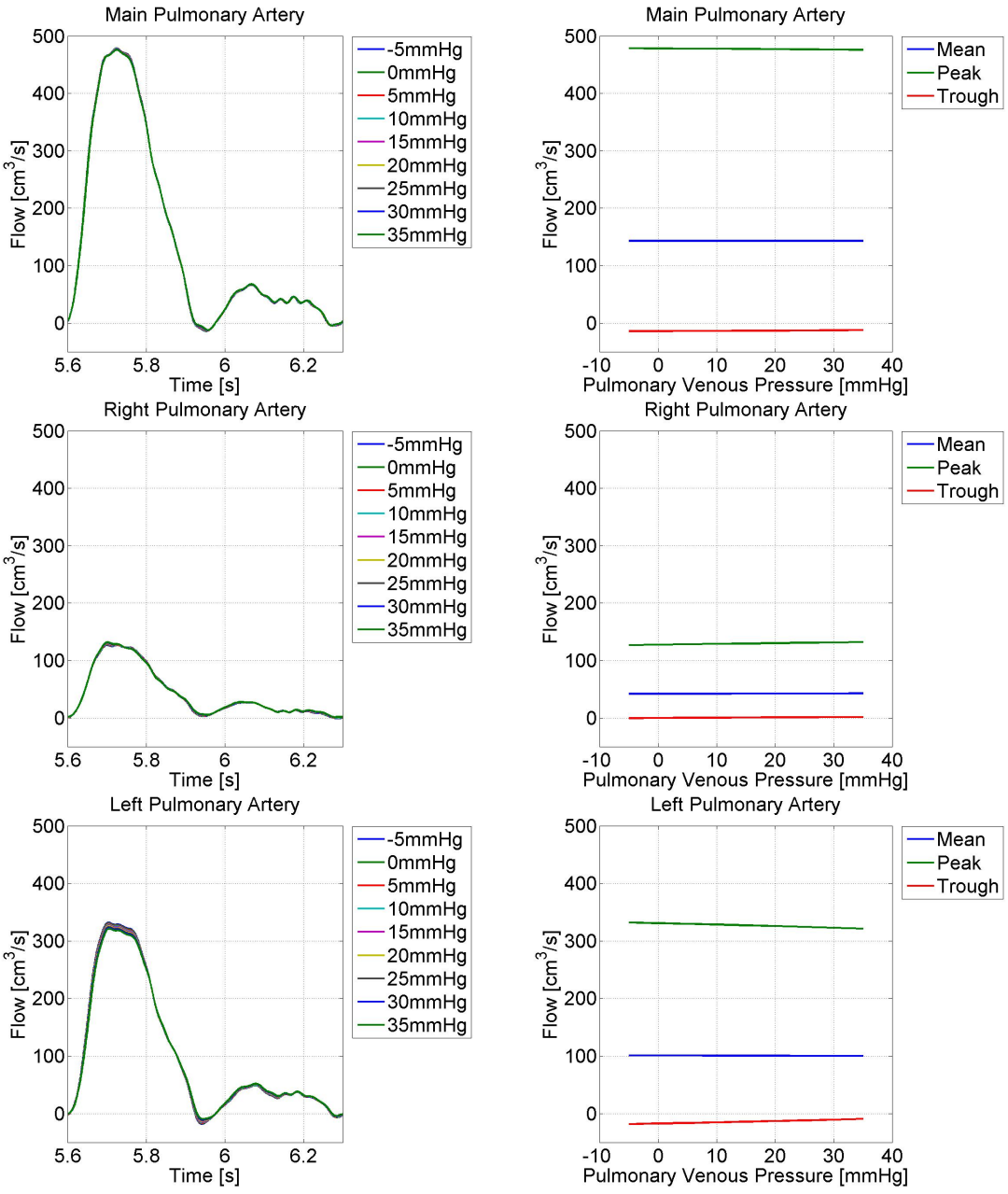

Figure 6.11: Effects of pulmonary venous hypertension on pulmonary arterial flow.

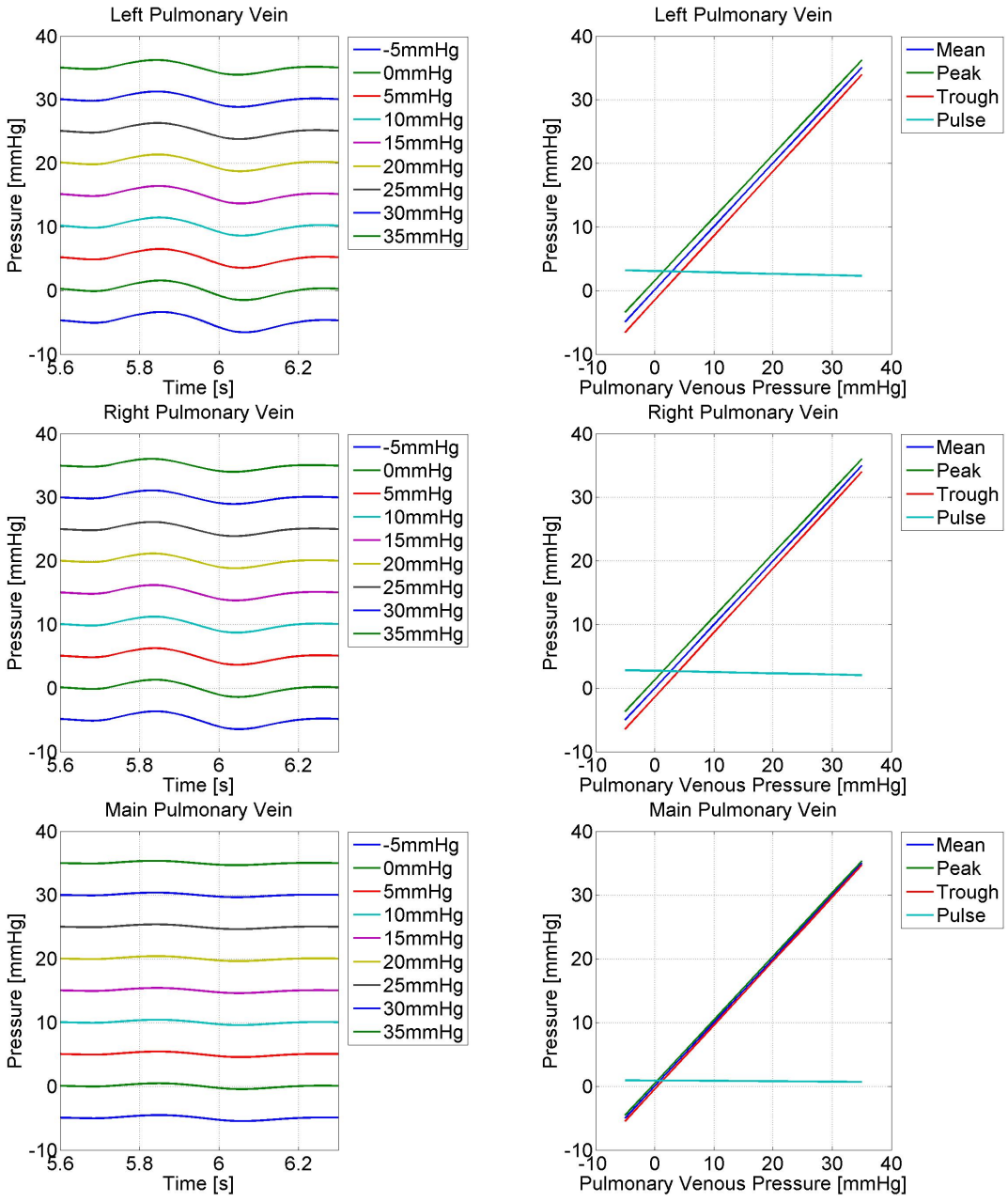

Figure 6.12: Effects of pulmonary venous hypertension on pulmonary venous pressure.

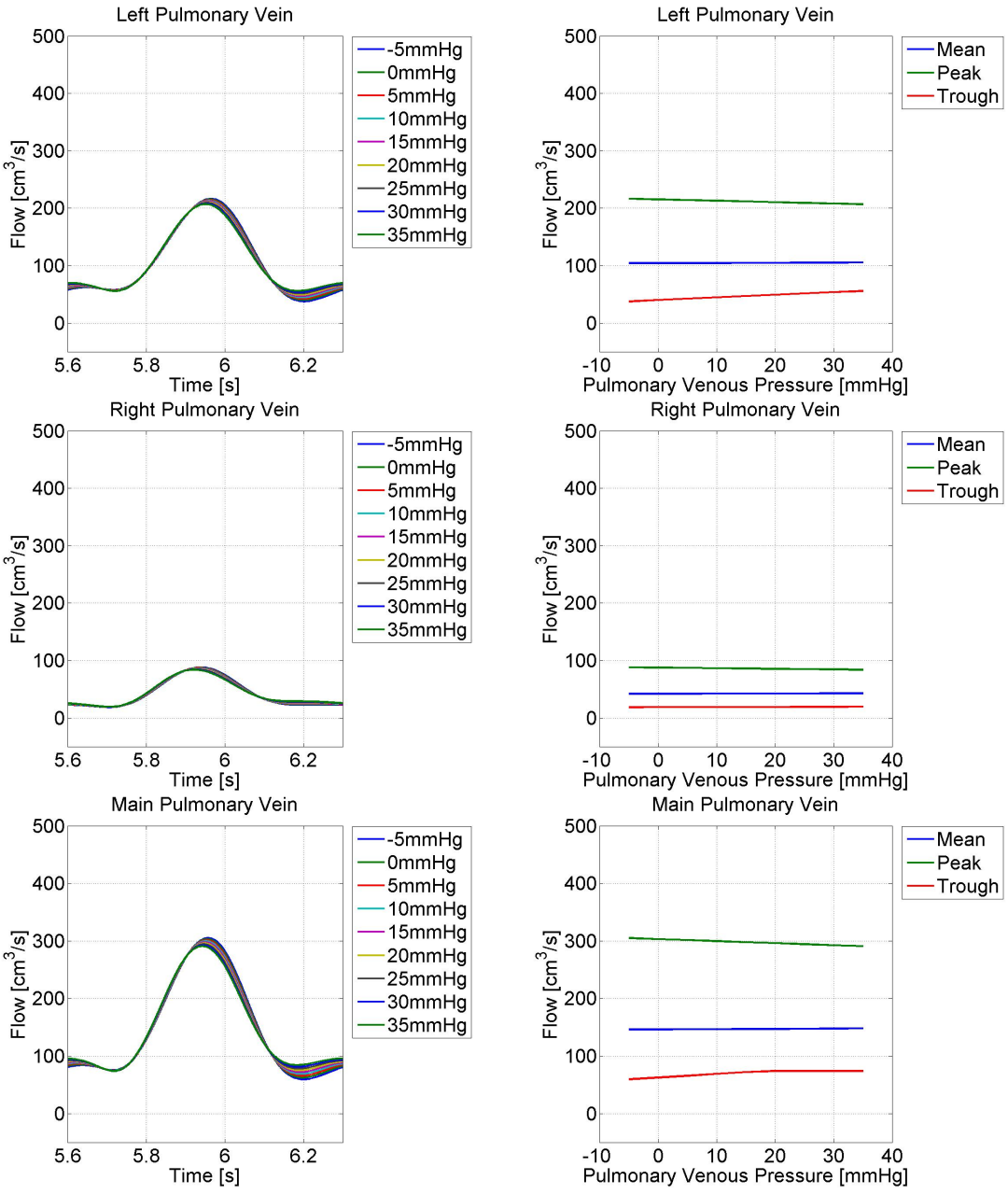

Figure 6.13: Effects of pulmonary venous hypertension on pulmonary venous flow.

6.2.3 Pulmonary Hypertension in association with hypoxic lung disease

Vascular remodelling associated with hypoxic lung disease results in an inhibition of oxygen absorption into the bloodstream [51]. Further, the loss of vascular beds due to vascular rarefaction may result in pulmonary hypertension.

In Section 3.2, we described the rarefaction of the systemic microcirculation by reducing the radius exponent ξ and the asymmetry ratio γ, thus reducing the area ratio η, of the structured tree (see Figure 3.7 for how ξ and γ affect η). We shall again use this approach to model rarefaction in the pulmonary circulation, however, whereas the systemic rarefaction model affected only an arterial tree, in our pulmonary model both the tree of small arteries and of small veins will be rarefied.

Results

Figure 6.14 shows predicted pressure pulse waveforms in the main pulmonary artery. It shows how rarefied vascular beds result in a significant increase in peak, trough and mean arterial pressure, as reinforced in Figure 6.16. Further, as the degree of rarefaction is increased, the separate peaks from the incident and reflected pressure pulses merge to form a single, more featureless, peak in the pressure waveform. This coinciding of the incident and reflected pressure may also explain the point of inflection in the relation between rarefaction and pulse pressure that can be seen in Figure 6.16.

Little change can be seen in the predicted main pulmonary artery flow waveforms in Figure 6.15 apart from a slight decrease in peak flow with increased rarefaction.

The same effects can be seen in the right (Figures 6.17 - 6.19) and left (Figures 6.20 - 6.22) pulmonary arteries, although the scale of reduction in flow is greater in the larger left pulmonary artery, than in the right.

Figures 6.23 - 6.31 show the effects of rarefaction on the pulmonary veins. Rarefaction can be seen to generally cause a reduction in the amplitude of both the venous pressure and flow waveforms. Interestingly, however, a reduction in amplitude is also seen when the parameters controlling rarefaction (particularly ξ) are increased above what is considered normal physiological values. Rarefaction also causes a phase shift in the venous pulse waves, with both venous pressure and flow waveforms peaking earlier under rarefied conditions.

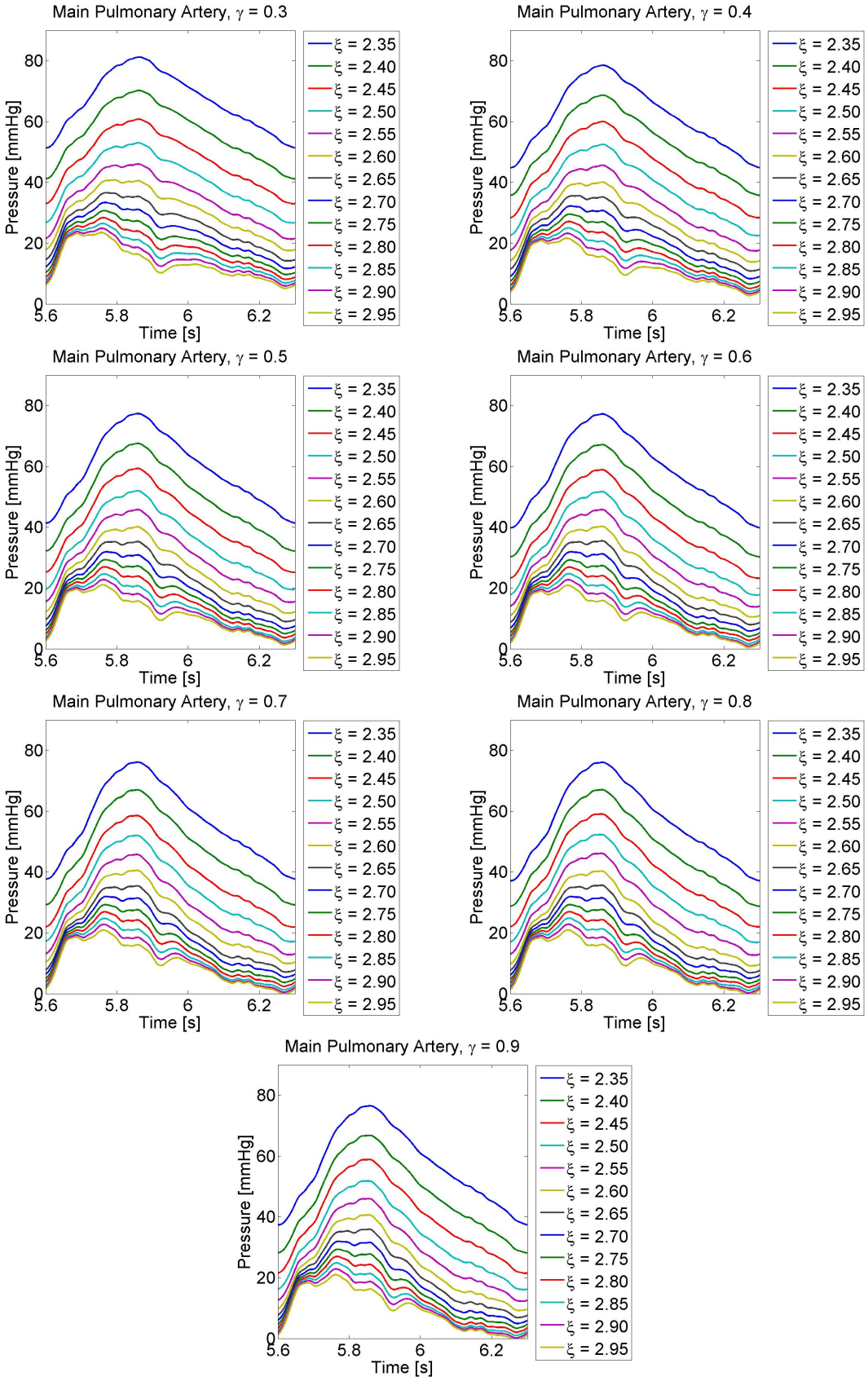

Figure 6.14: Effects of rarefaction on pressure pulse waveform in the Main Pulmonary Artery.

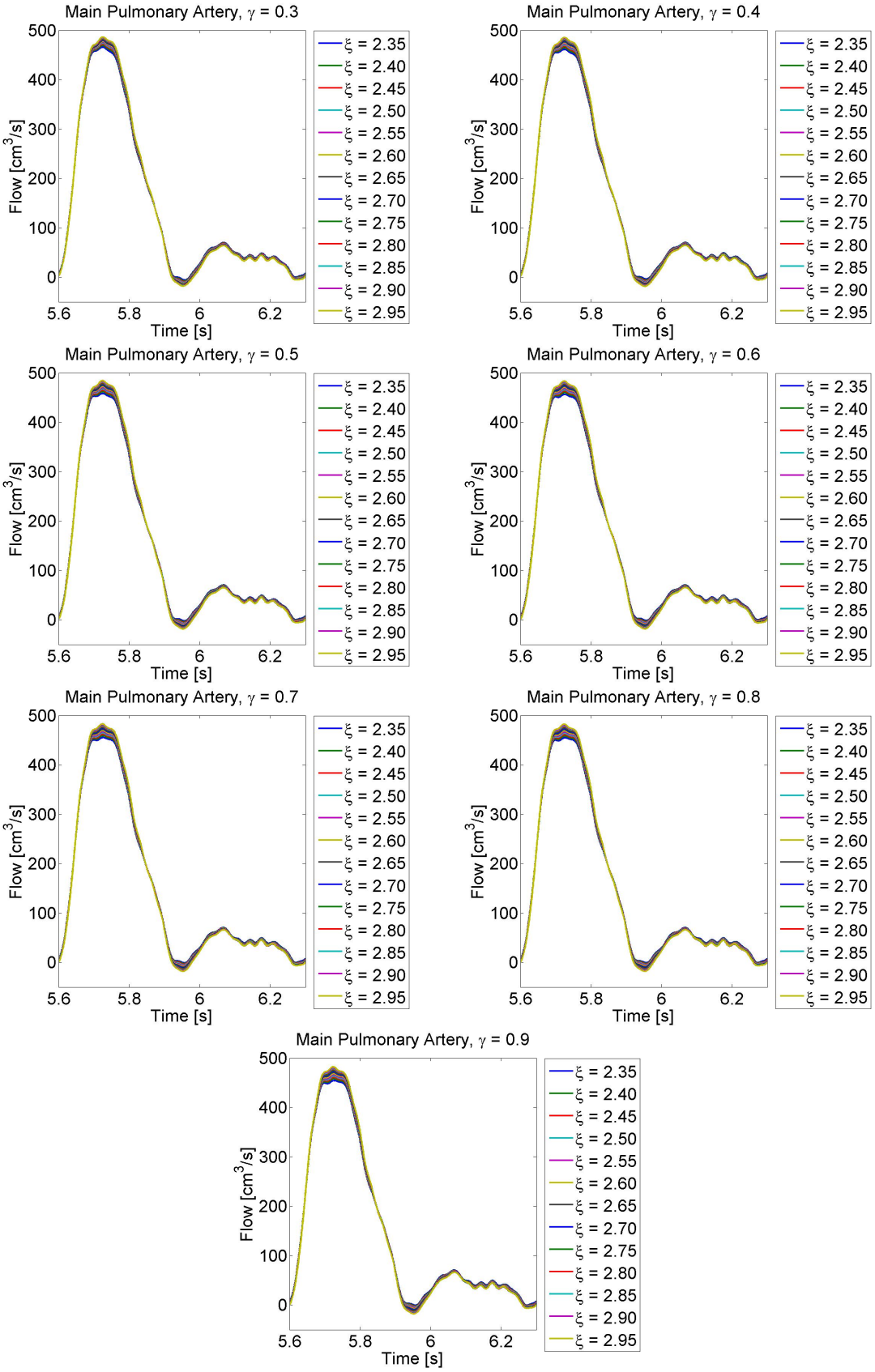

Figure 6.15: Effects of rarefaction on flow waveform in the Main Pulmonary Artery.

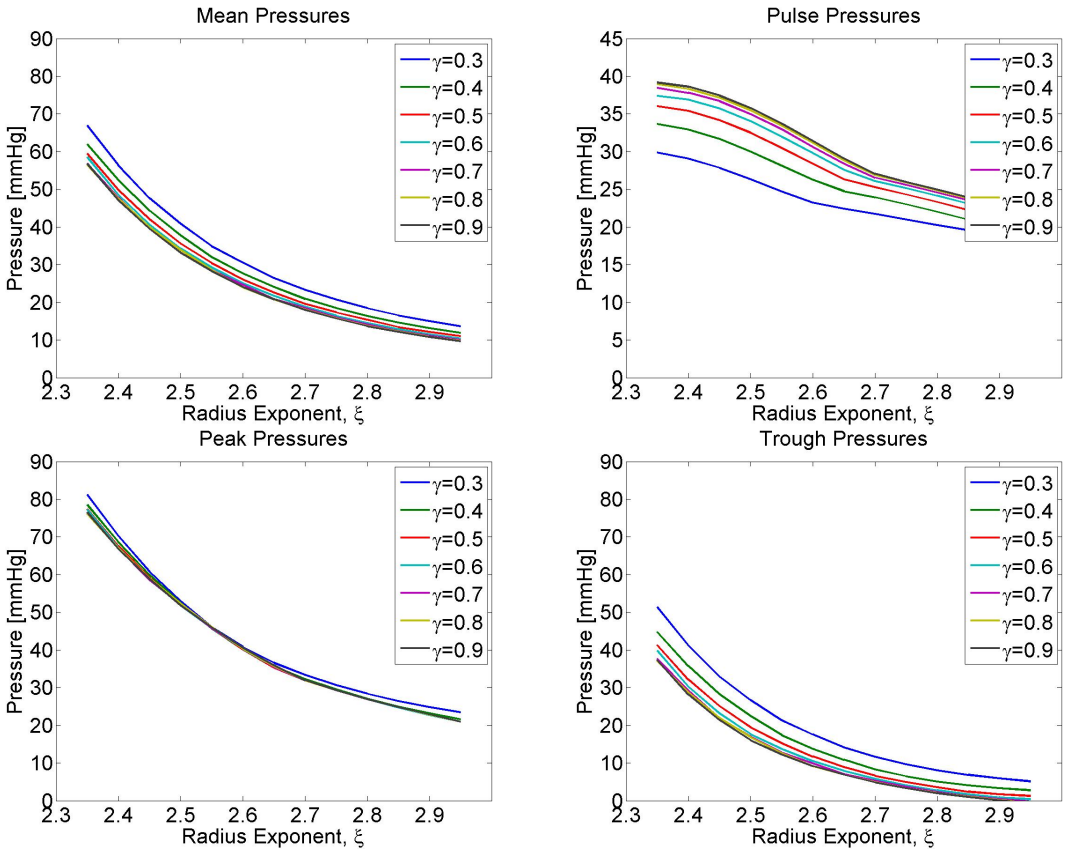

Figure 6.16: Effects of rarefaction on mean, pulse, peak and trough pressure in the Main Pulmonary Artery.

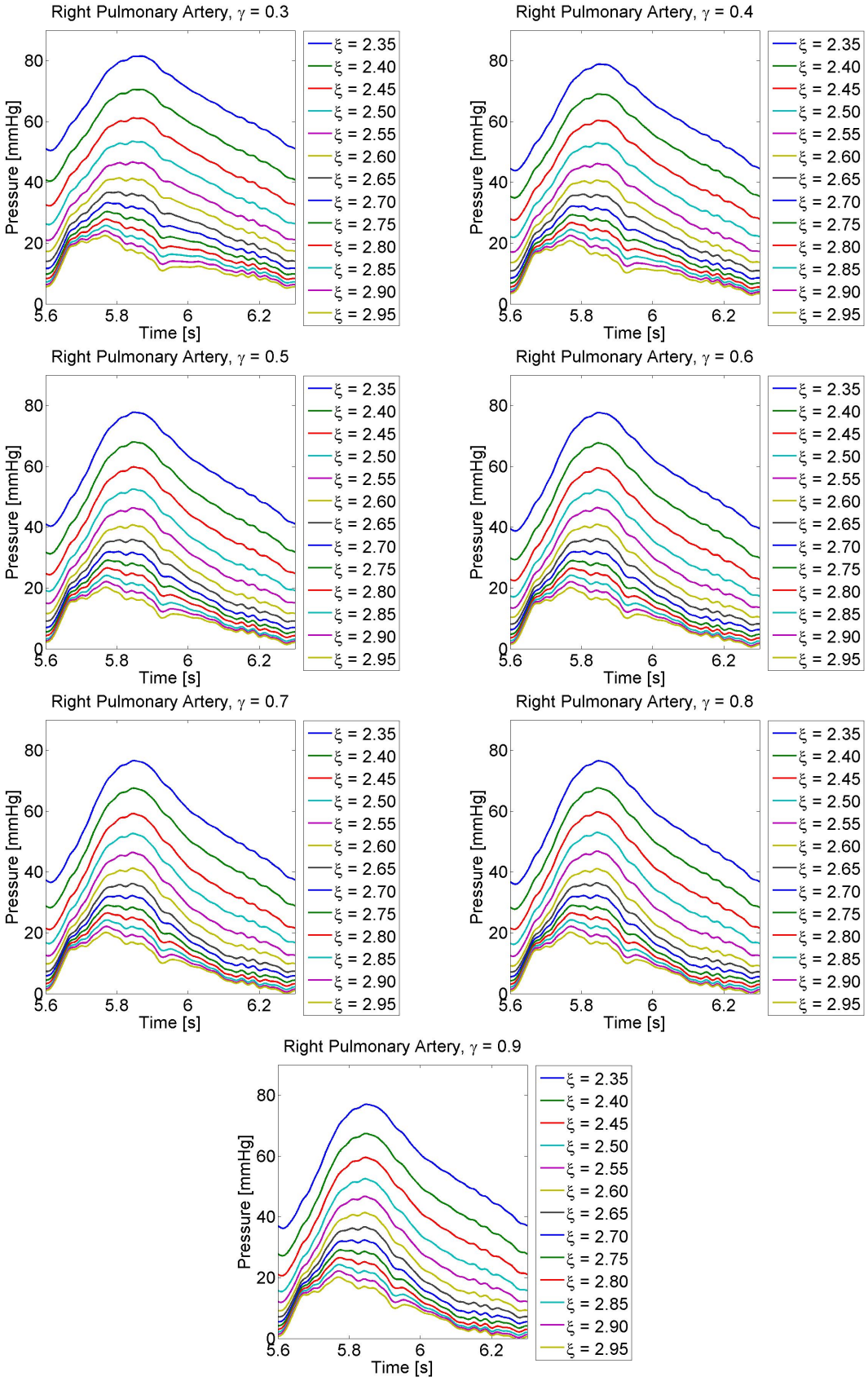

Figure 6.17: Effects of rarefaction on pressure pulse waveform in the Right Pulmonary Artery.

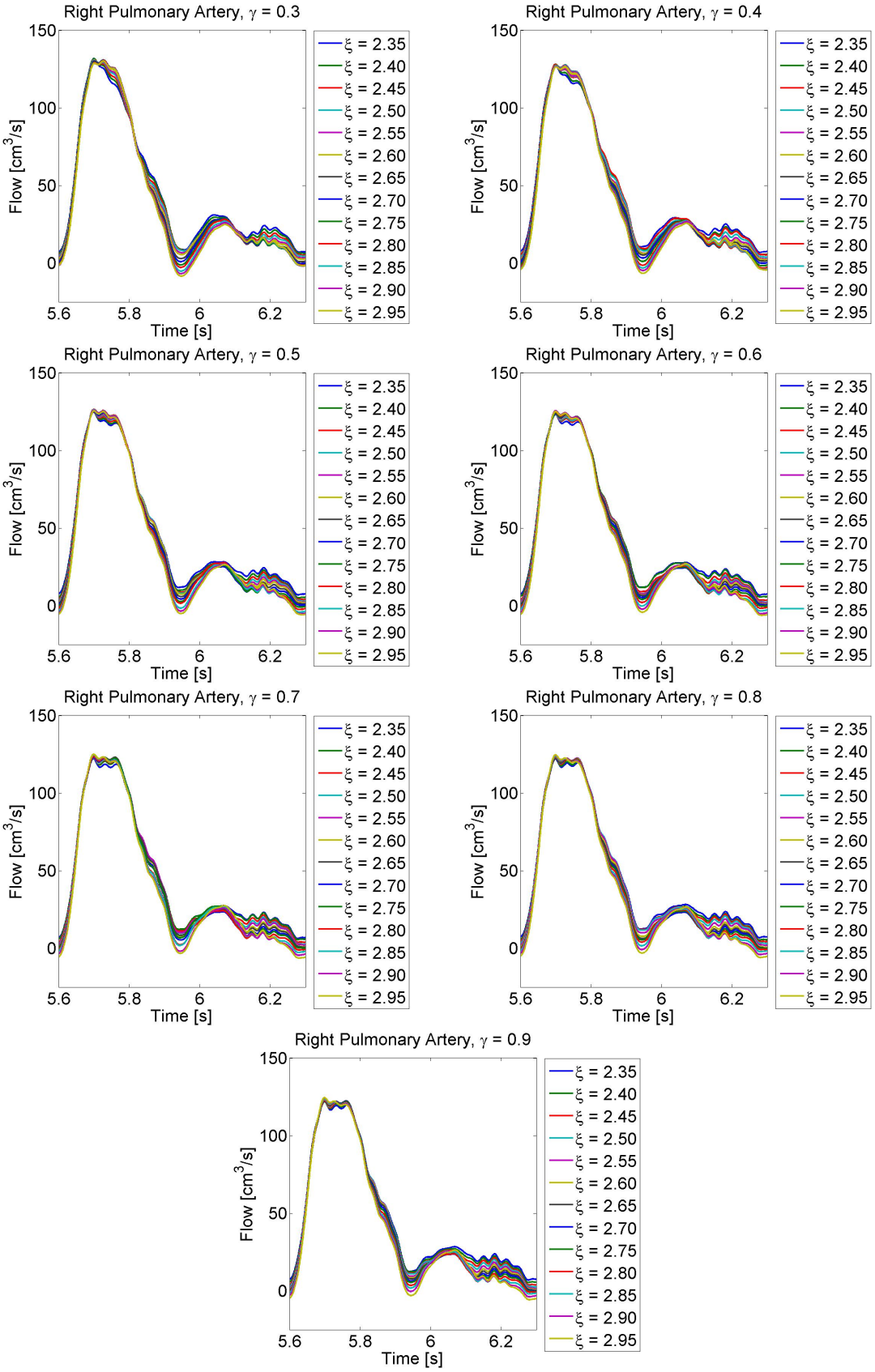

Figure 6.18: Effects of rarefaction on flow waveform in the Right Pulmonary Artery.

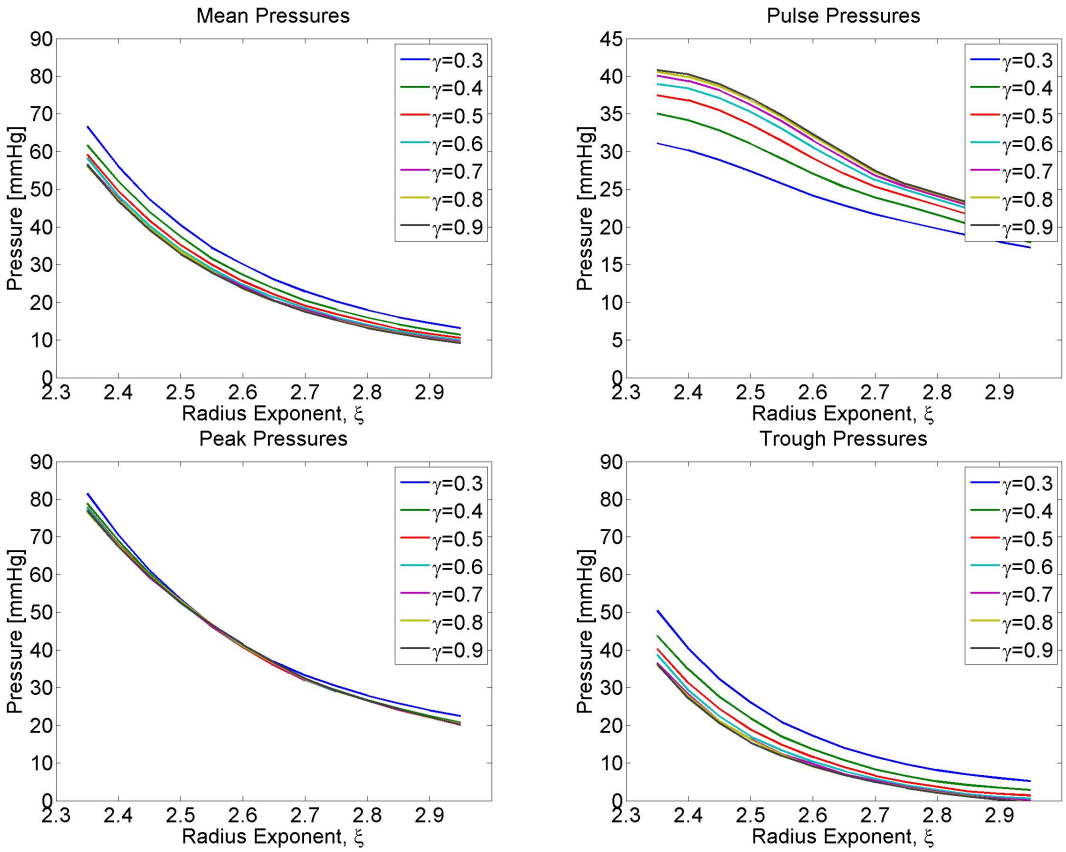

Figure 6.19: Effects of rarefaction on mean, pulse, peak and trough pressure in the Right Pulmonary Artery.

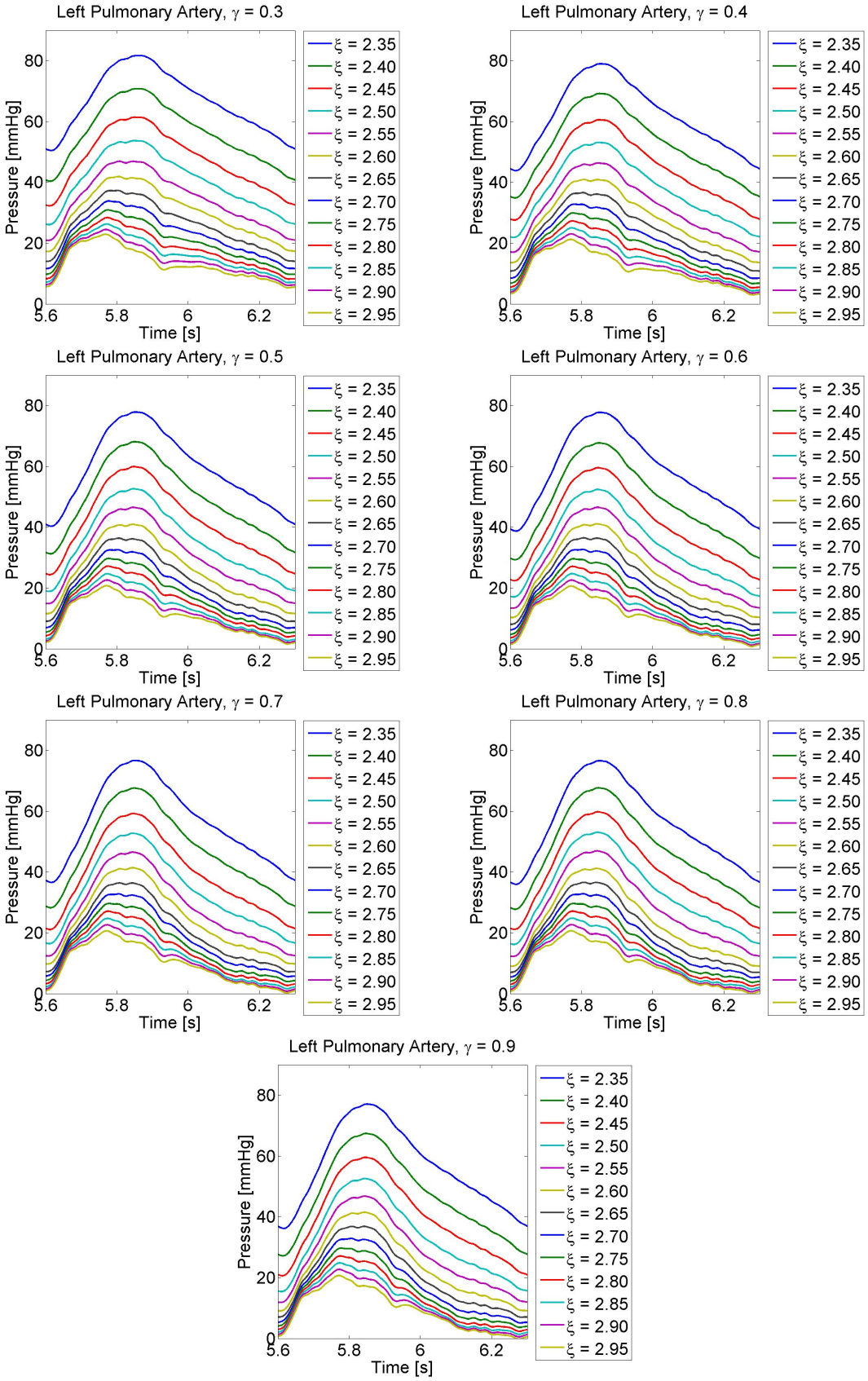

Figure 6.20: Effects of rarefaction on pressure pulse waveform in the Left Pulmonary Artery.

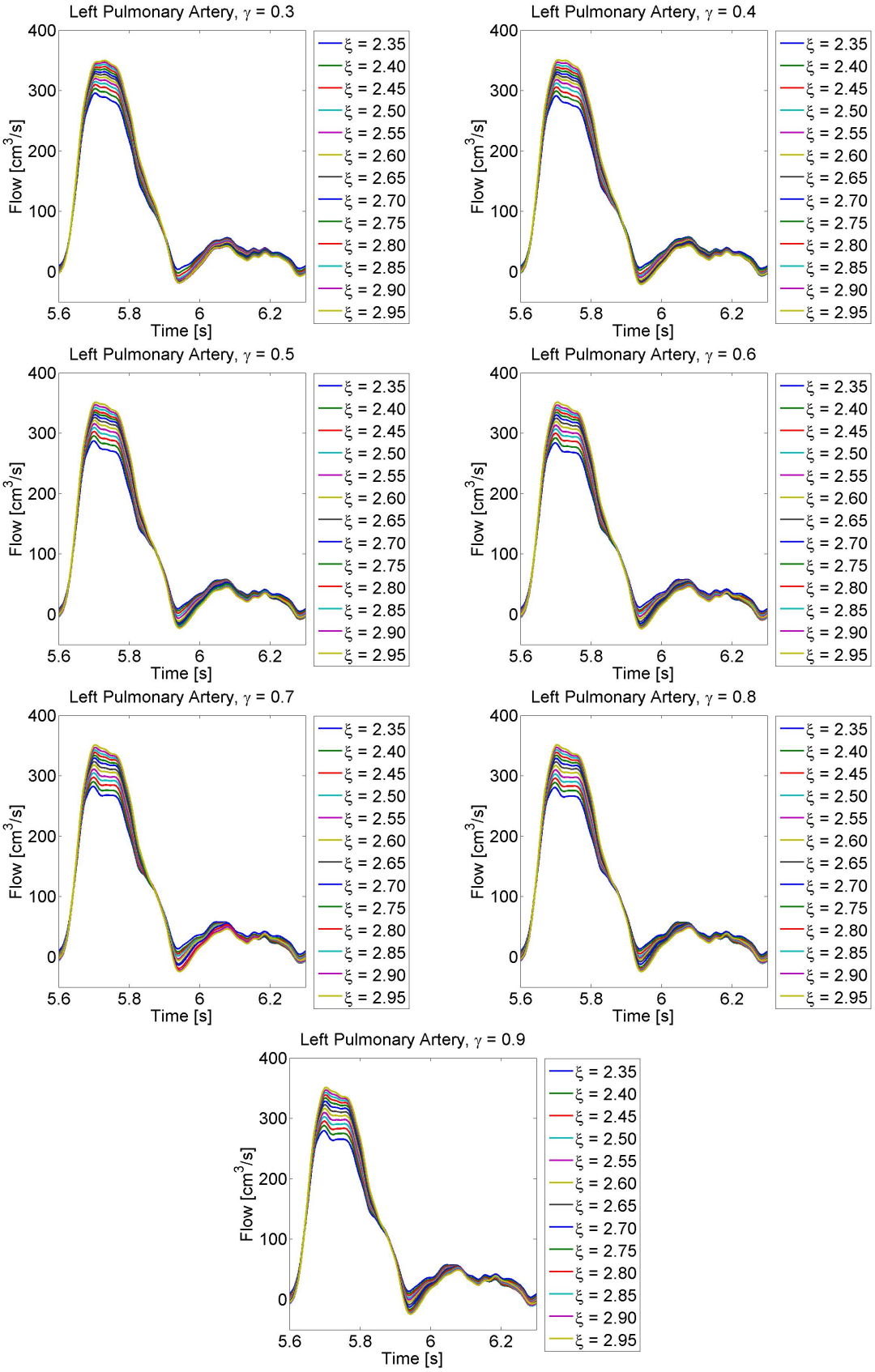

Figure 6.21: Effects of rarefaction on flow waveform in the Left Pulmonary Artery.

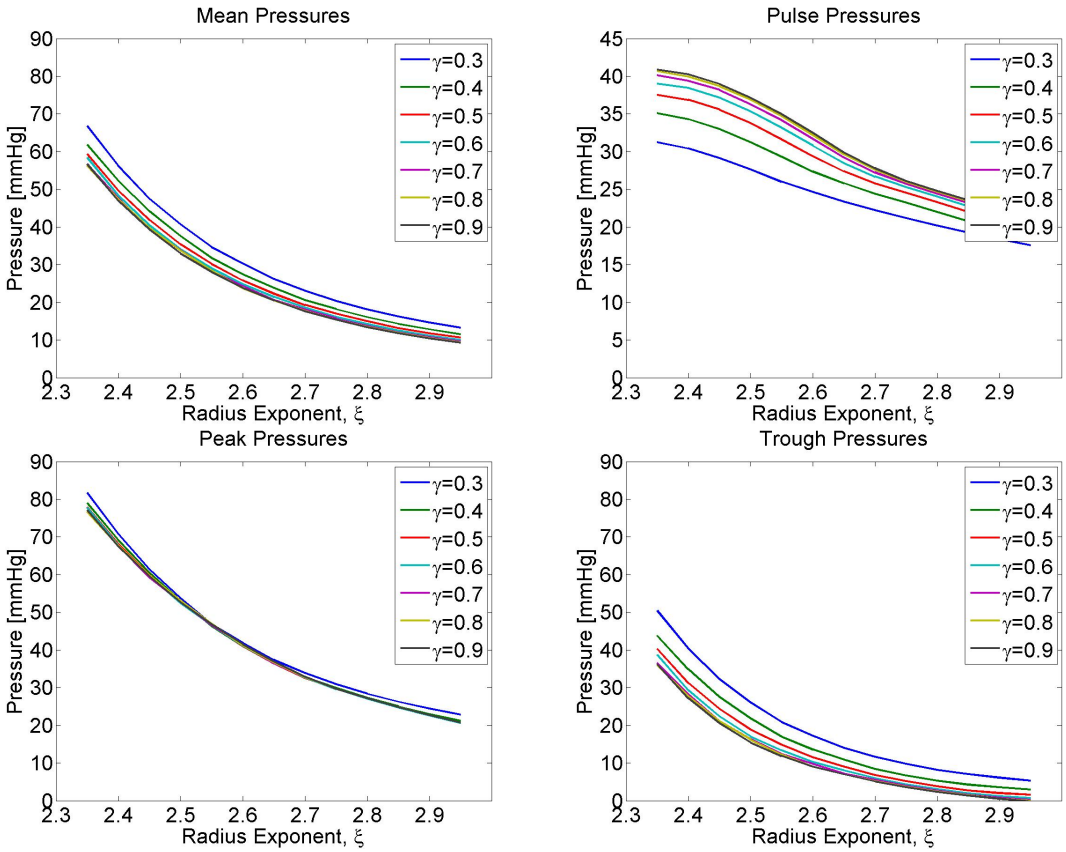

Figure 6.22: Effects of rarefaction on mean, pulse, peak and trough pressure in the Left Pulmonary Artery.

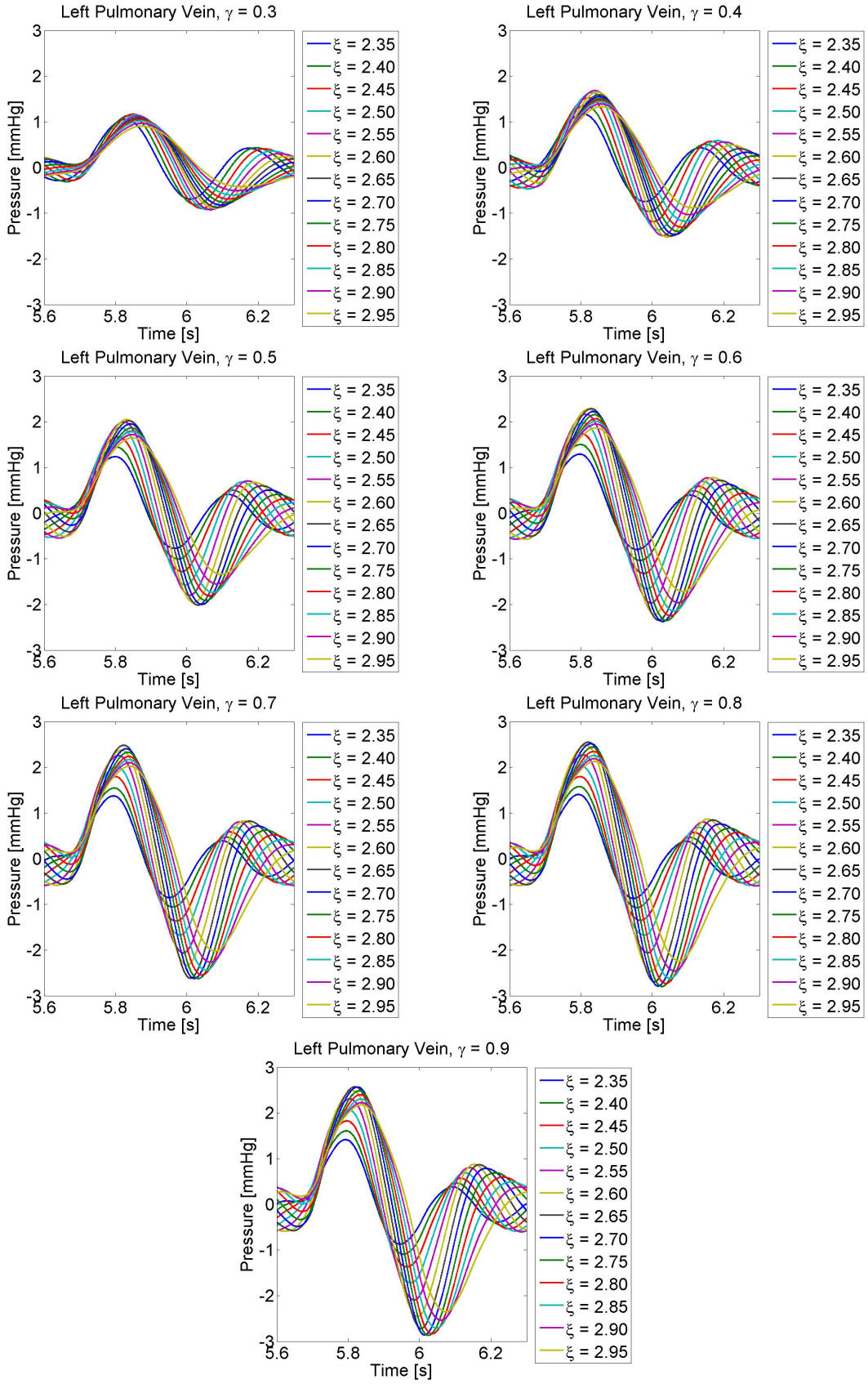

Figure 6.23: Effects of rarefaction on pressure pulse waveform in the Left Pulmonary Vein.

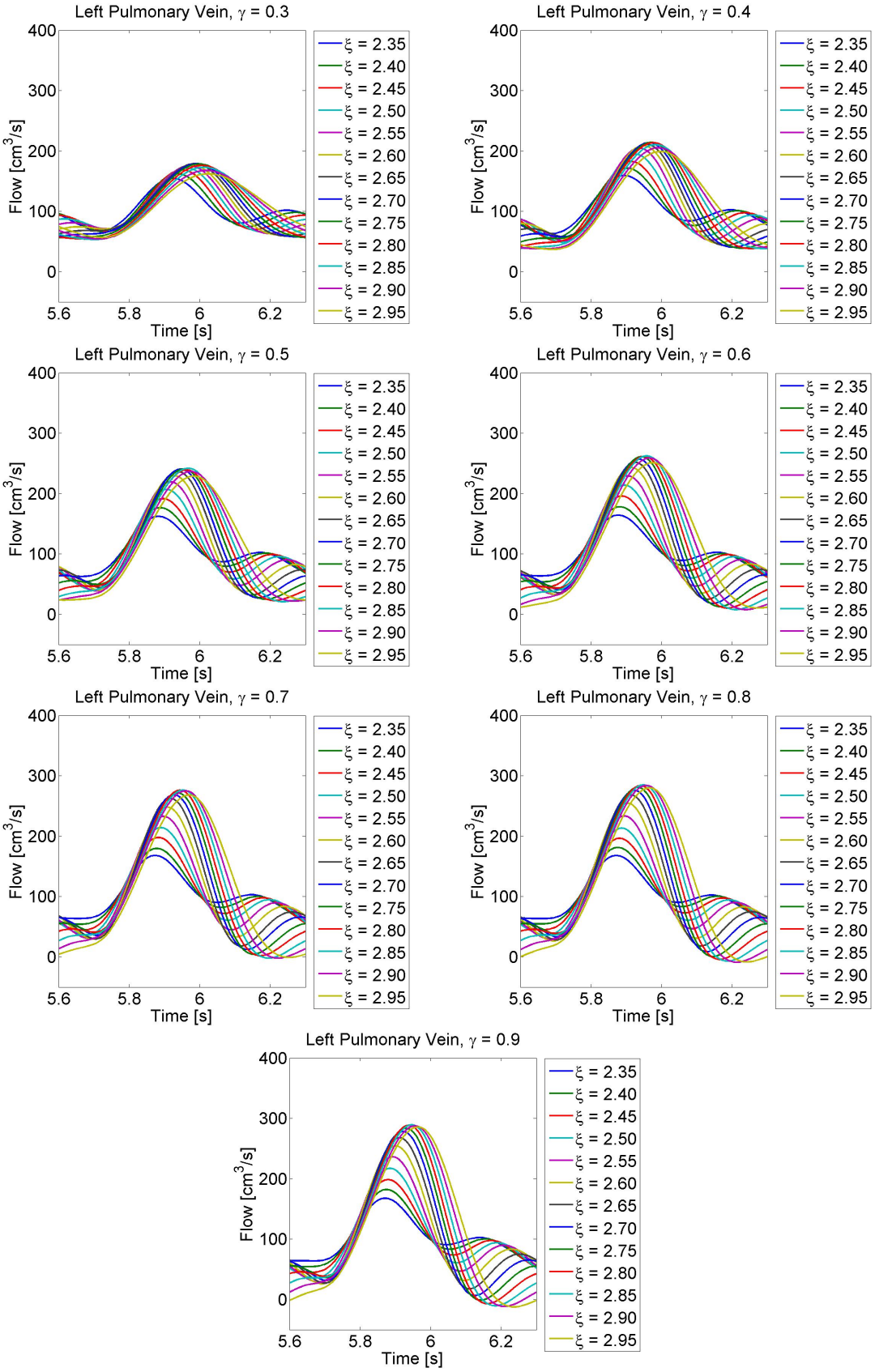

Figure 6.24: Effects of rarefaction on flow waveform in the Left Pulmonary Vein.

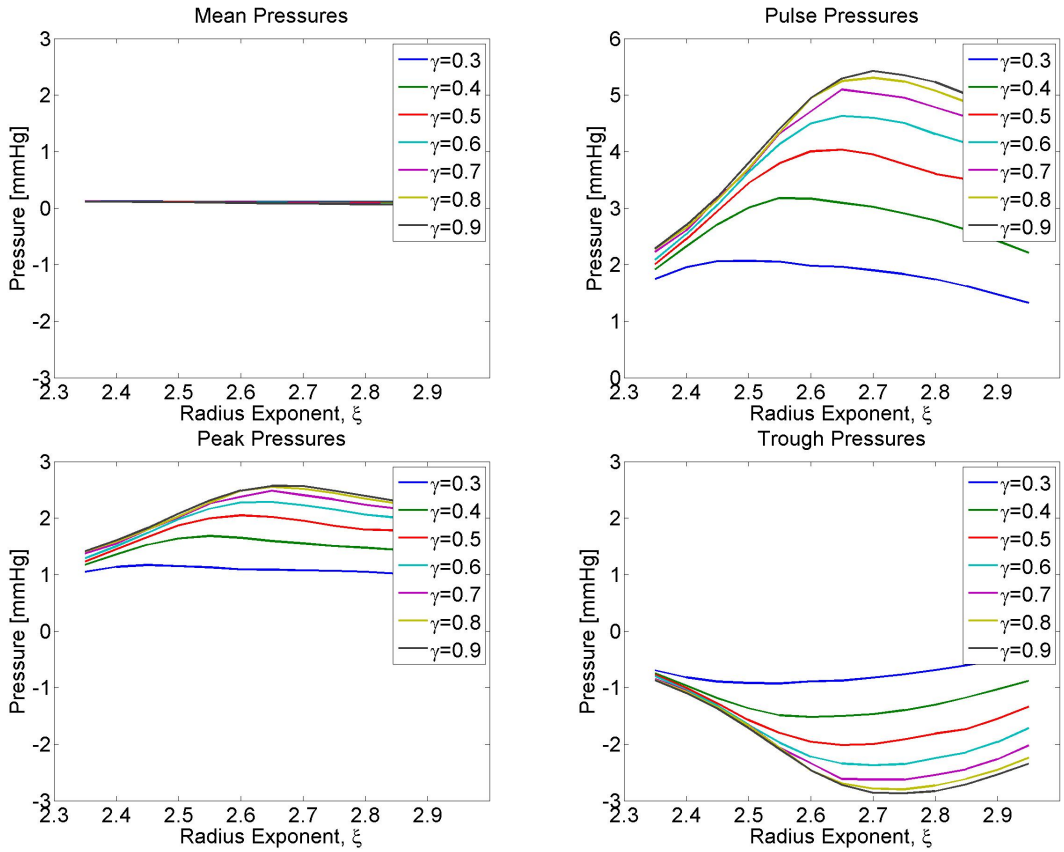

Figure 6.25: Effects of rarefaction on mean, pulse, peak and trough pressure in the Left Pulmonary Vein.

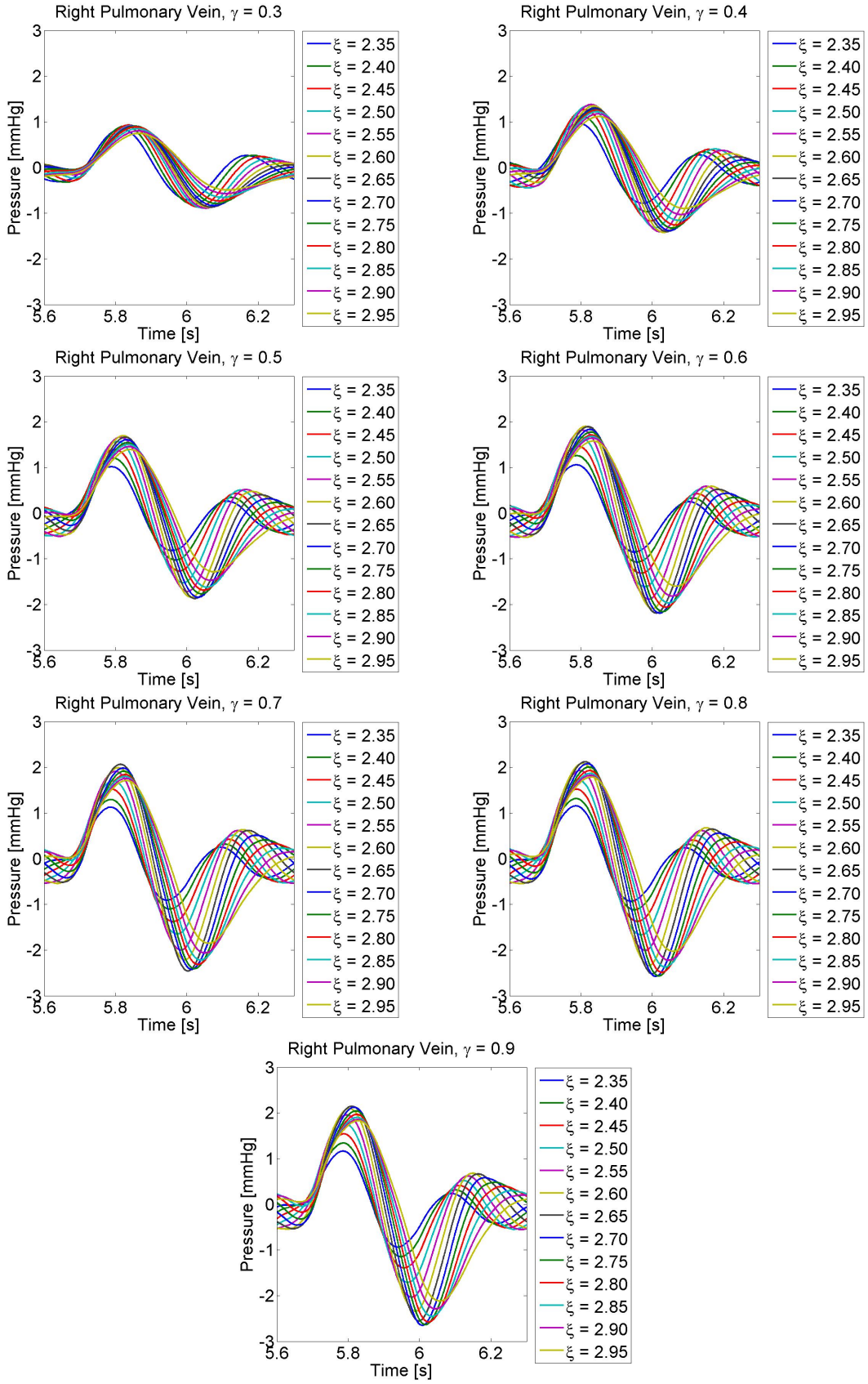

Figure 6.26: Effects of rarefaction on pressure pulse waveform in the Right Pulmonary Vein.

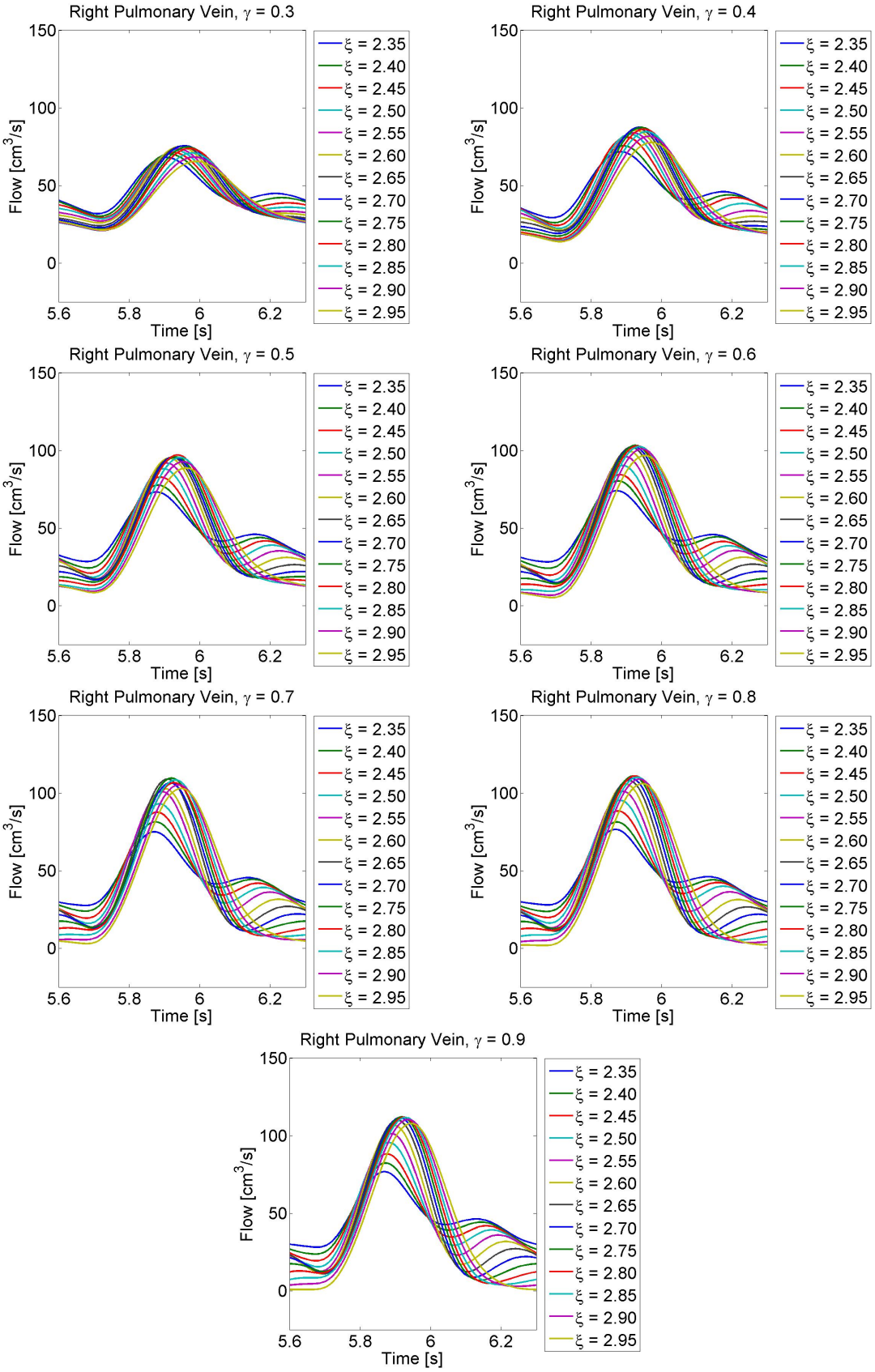

Figure 6.27: Effects of rarefaction on flow waveform in the Right Pulmonary Vein.

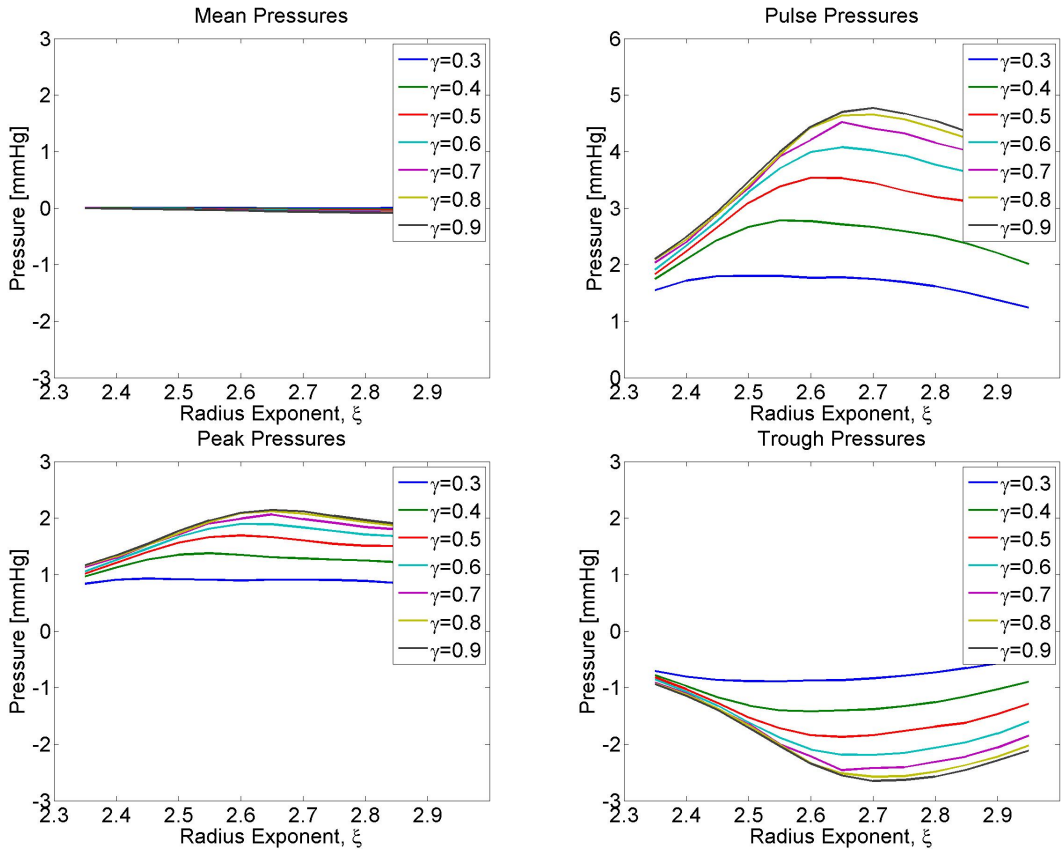

Figure 6.28: Effects of rarefaction on mean, pulse, peak and trough pressure in the Right Pulmonary Vein.

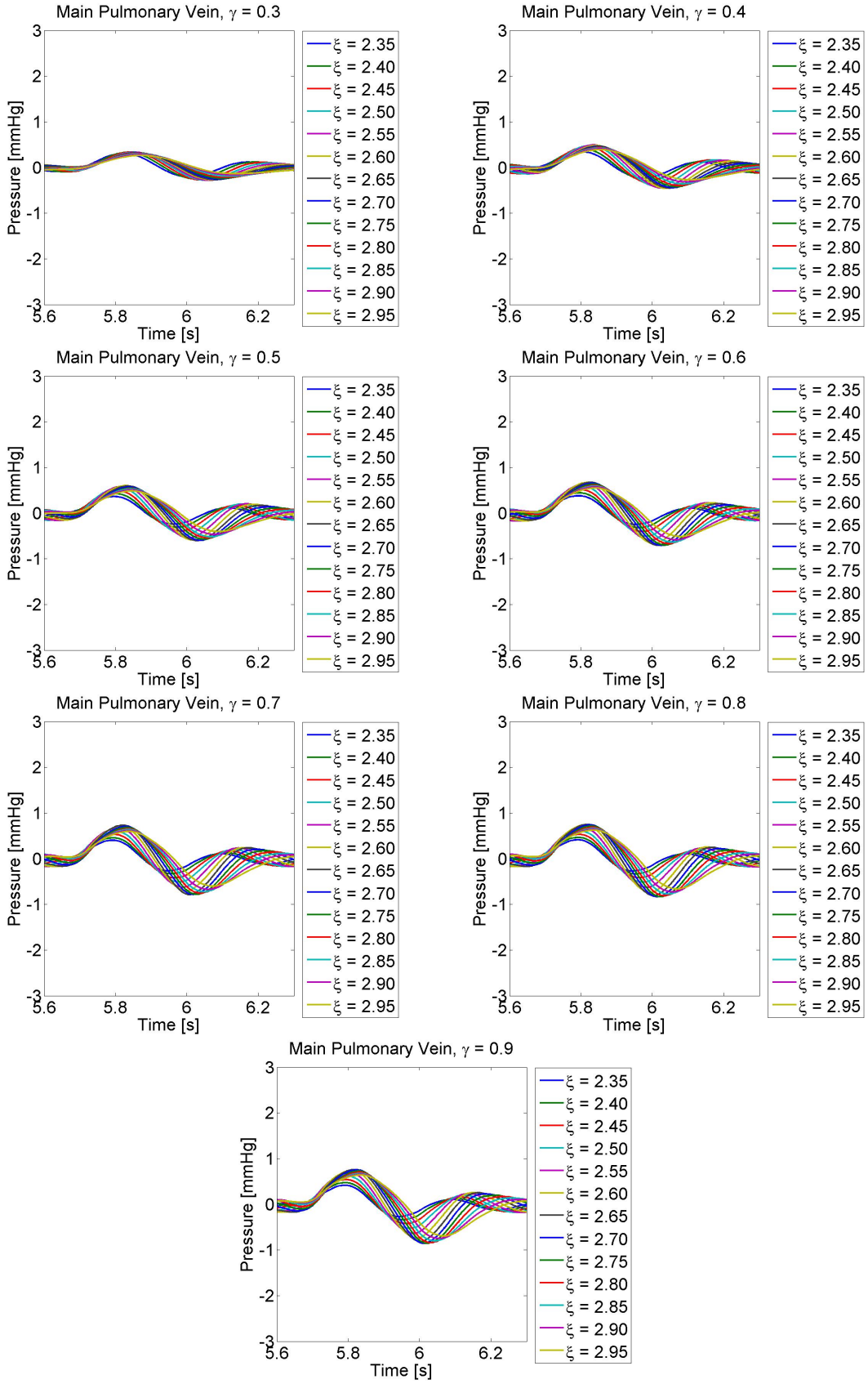

Figure 6.29: Effects of rarefaction on pressure pulse waveform in the Main Pulmonary Vein.

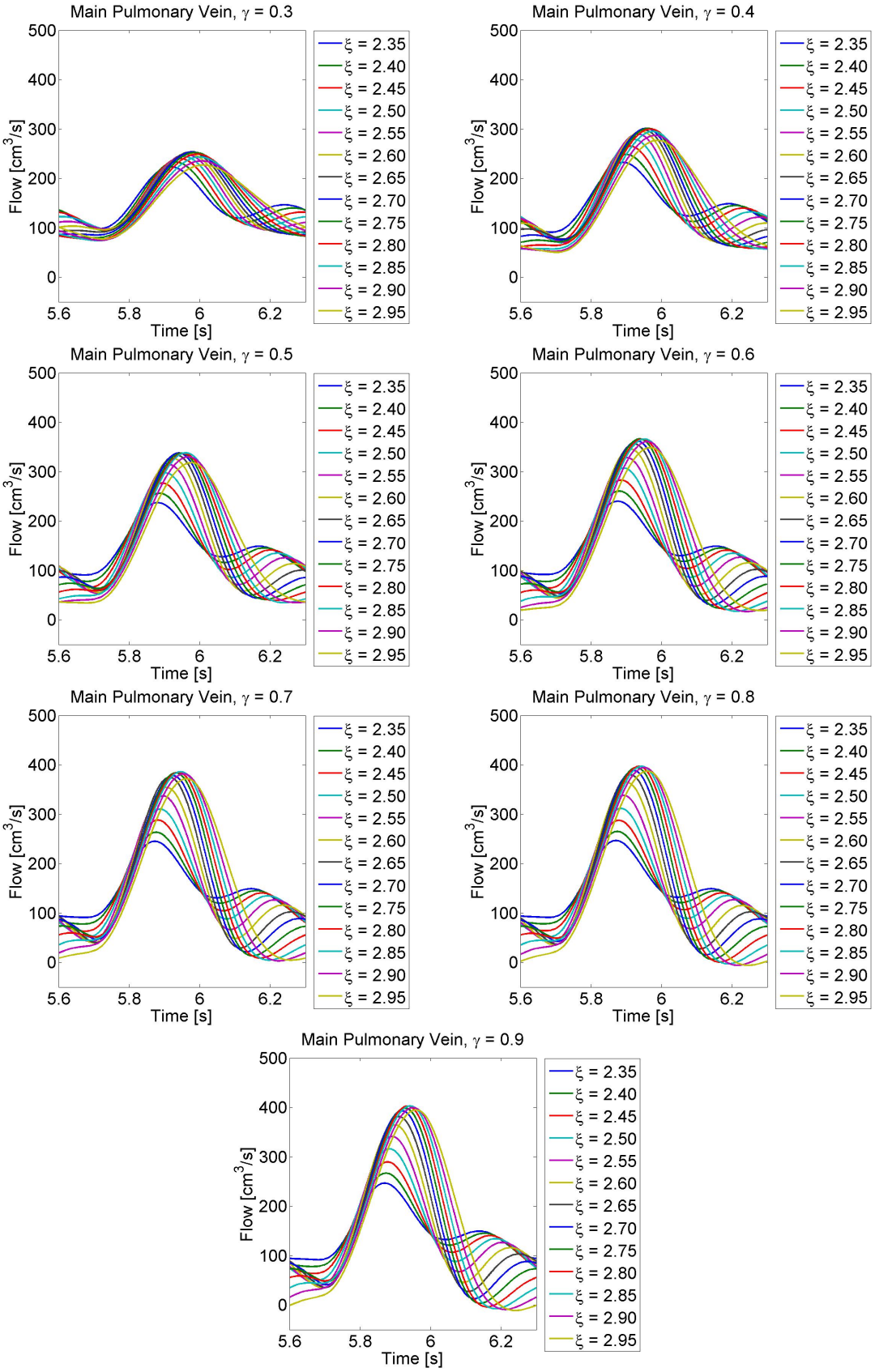

Figure 6.30: Effects of rarefaction on flow waveform in the Main Pulmonary Vein.

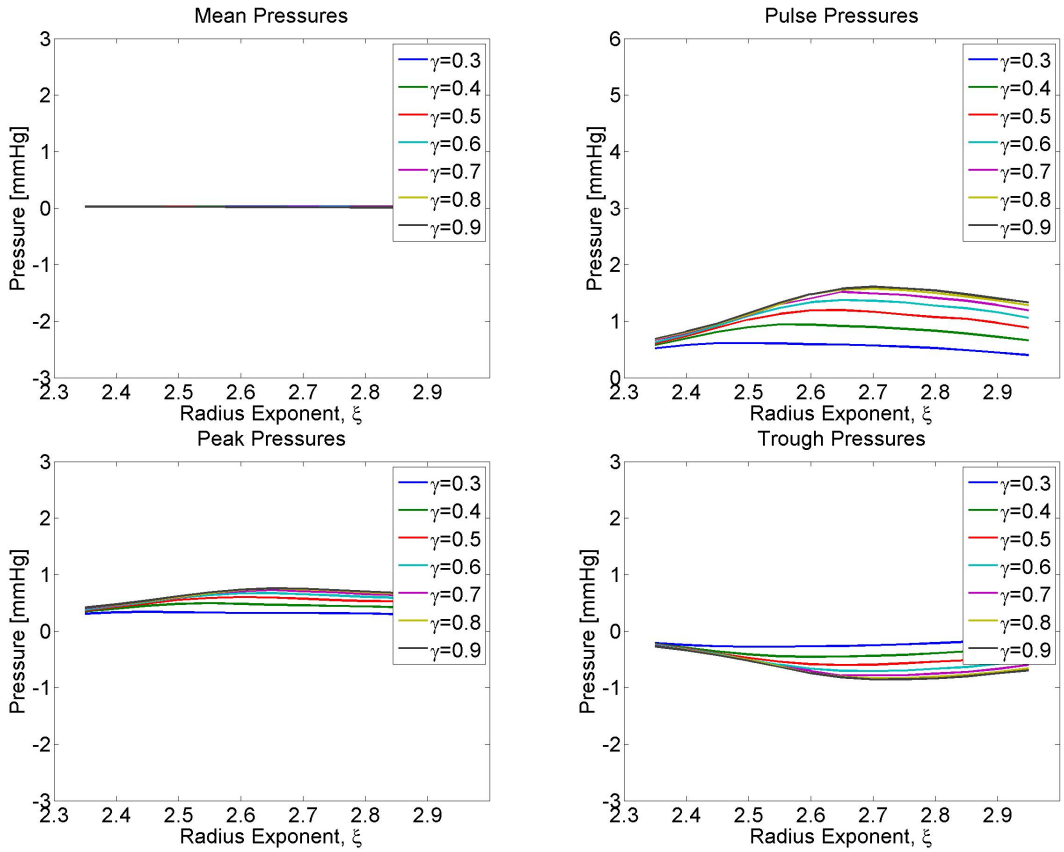

Figure 6.31: Effects of rarefaction on mean, pulse, peak and trough pressure in the Main Pulmonary Vein.

6.2.4 Chronic Thromboembolic Pulmonary Hypertension

The pathophysiology of Chronic Thromboembolic Pulmonary Hypertension is similar to that of Pulmonary Arterial Hypertension, except that it occurs in the larger proximal pulmonary arteries [7], [11], although the small vessels may also become involved evenually.

As we did in Section 3.4 for the systemic arteries, and in Section 6.2.1 of this chapter when modelling Pulmonary Arterial Hypertension, we can simulate the initial effects of chronic thromboembolic pulmonary hypertension by stiffening the large arteries only. We can then model the later effects, when the small arteries become involved, by stiffening both the large and small arteries uniformly.

Results

In Figure 6.32, we see how increasing the stiffness of the large pulmonary arteries results in an increase in peak and pulse pressure in those arteries, and that there is a steeper, earlier peak to the pressure pulse in stiffer arteries, with a secondary peak appearing shortly after the first. This increase in pressure and appearance of a second peak agrees with the observations of pressure pulses in patients with chronic thromboembolic pulmonary hypertension by Lankhaar et al. [27] (middle graphs of Figure 6.5), although the scale of the observed increase in peak pressure is much greater than in our predictions.

Predicted flows in the pulmonary arteries are shown in Figure 6.33, with little effect seen apart from slightly later peaking of the flow wave in the left and right pulmonary arteries, a less pronounced effect than suggested in clinical observations [27].

In the pulmonary veins, a slight increase in amplitude of both the pressure waveform (Figure 6.34) and flow waveform (Figure 6.35) is seen in instances of stiffer large arteries without any notable changes in the shape of the waveforms.

When we add in the effects of the small vessels by carrying out uniform changes of both large and small vessel stiffness, we see a more significant increase in pressure in the pulmonary arteries (Figure 6.36) with increased stiffness, as well as the earlier peaking of the pressure pulse we observed previously. This is more in line with clinical observations.

The same slight effect of later peaking of left and right pulmonary arterial flow waveforms can be seen in Figure 6.37, while in the pulmonary veins more significant increases in amplitude of both the pressure (Figure 6.38) and flow (Figure 6.39) waveforms are seen in instances of stiffer arteries, as well as earlier peaking of both waveforms.

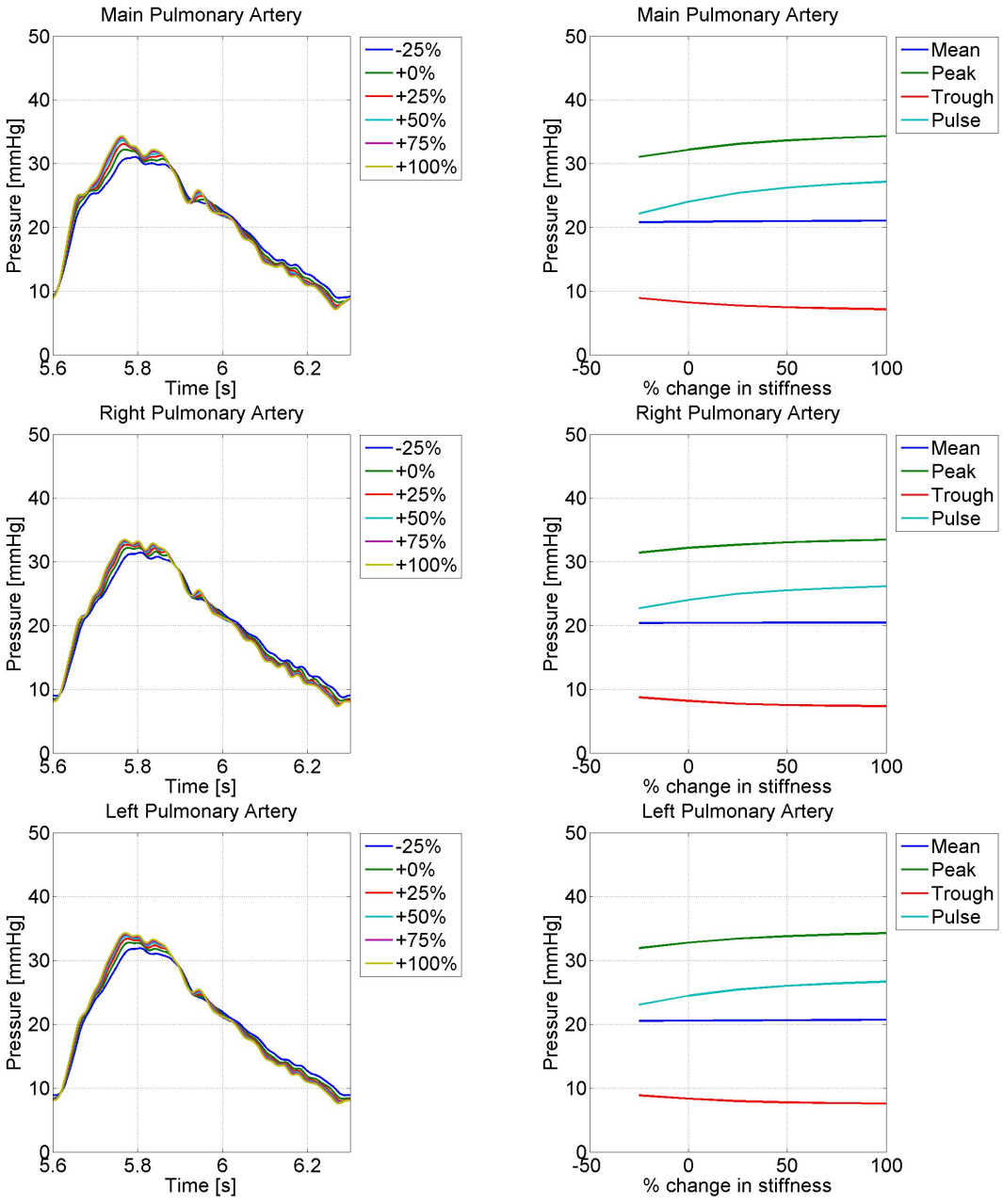

Figure 6.32: Effects of changing large vessel compliance on Pulmonary Artery Pressure.

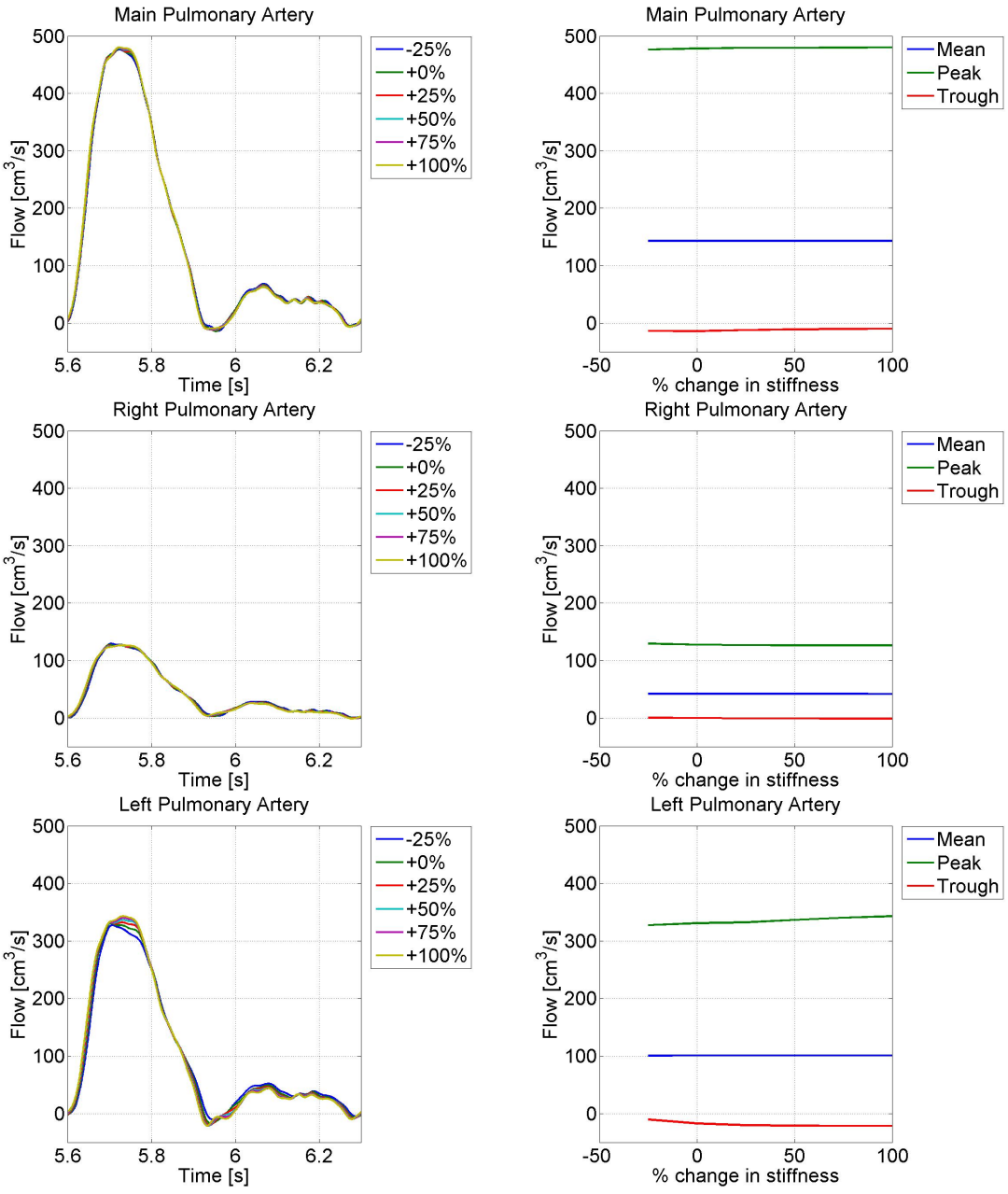

Figure 6.33: Effects of changing large vessel compliance on Pulmonary Artery Flow.

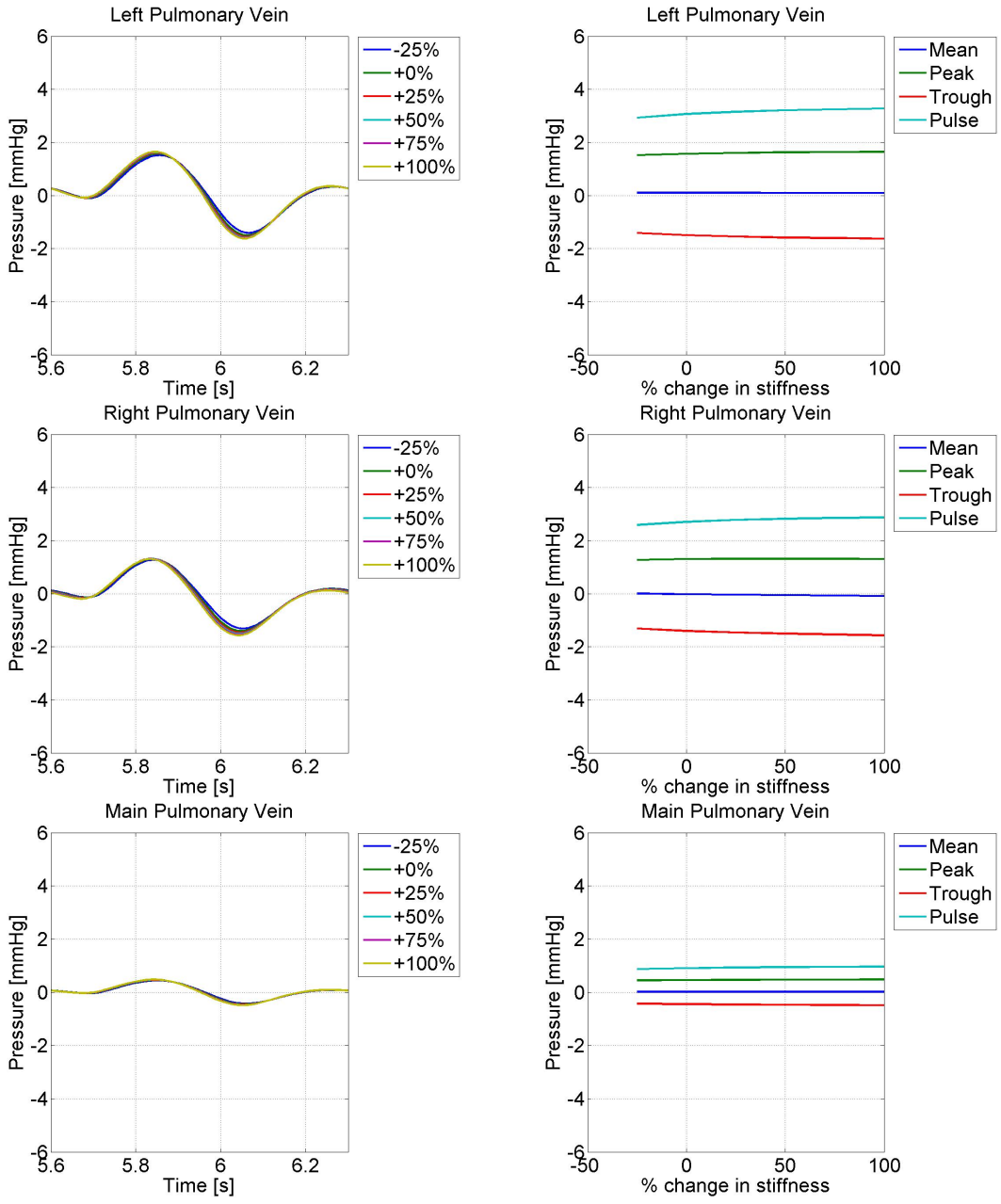

Figure 6.34: Effects of changing large vessel compliance on Pulmonary Venous Pressure.

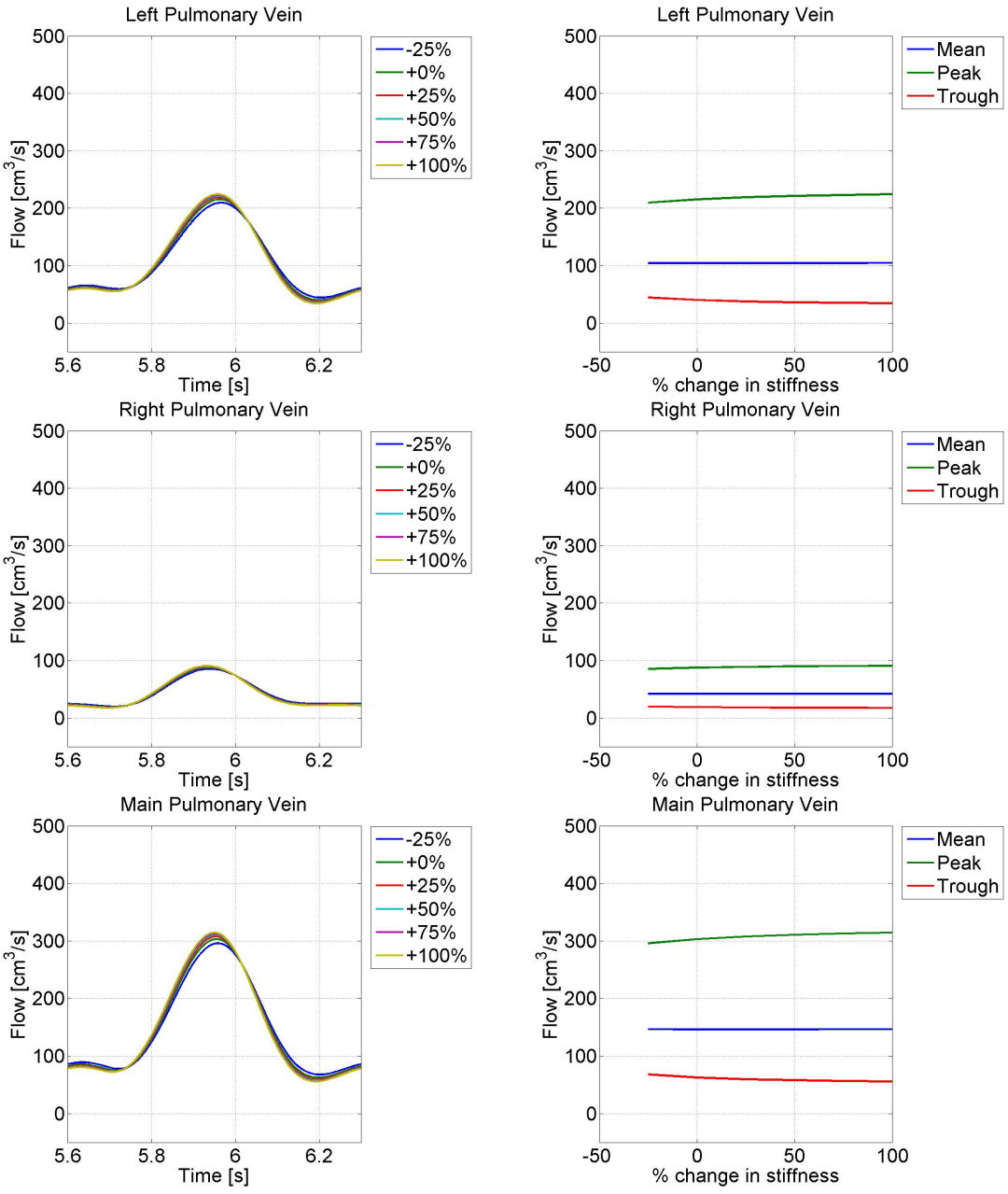

Figure 6.35: Effects of changing large vessel compliance on Pulmonary Venous Flow.

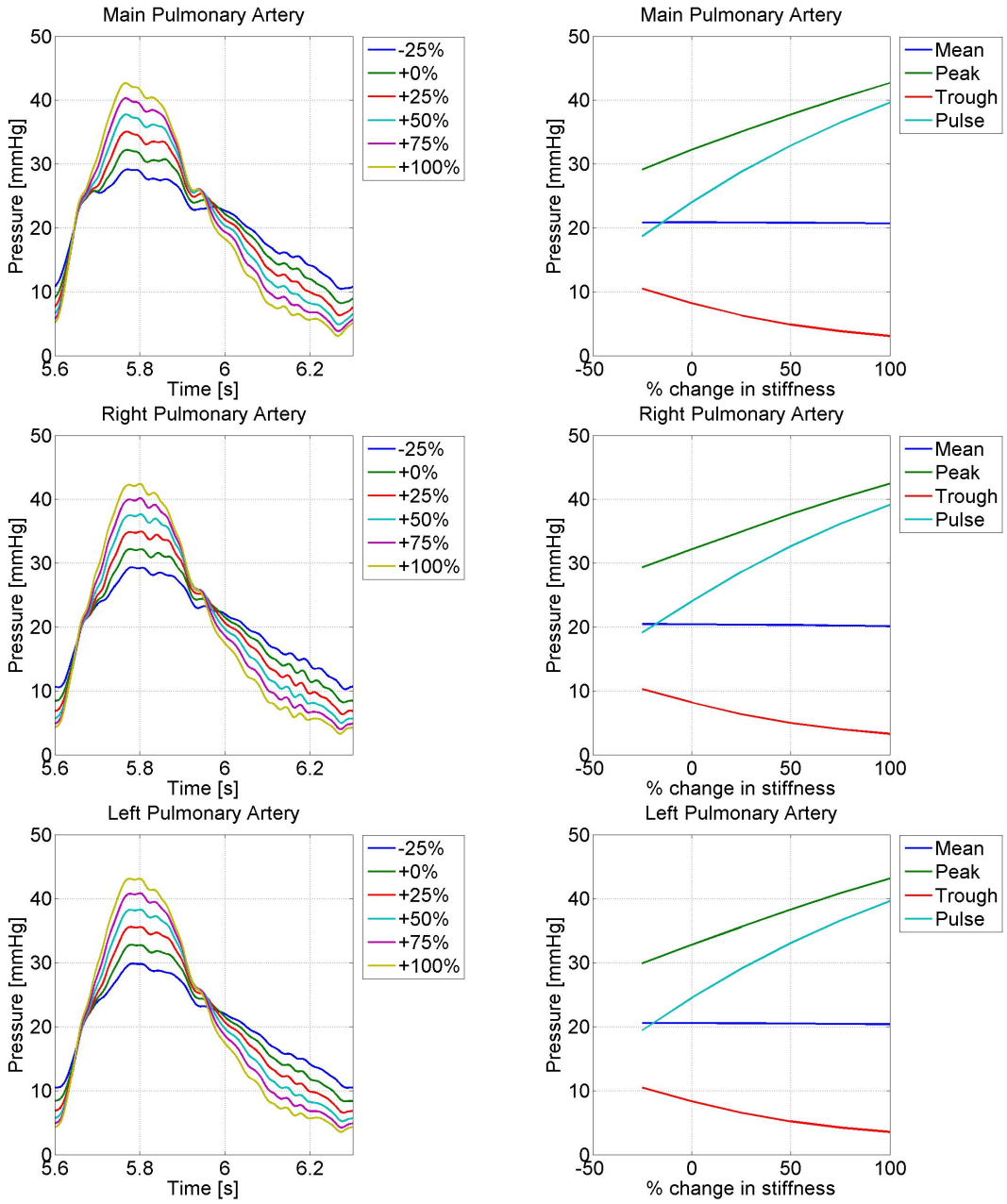

Figure 6.36: Effects of changing both large and small vessel compliance on Pulmonary Artery Pressure.

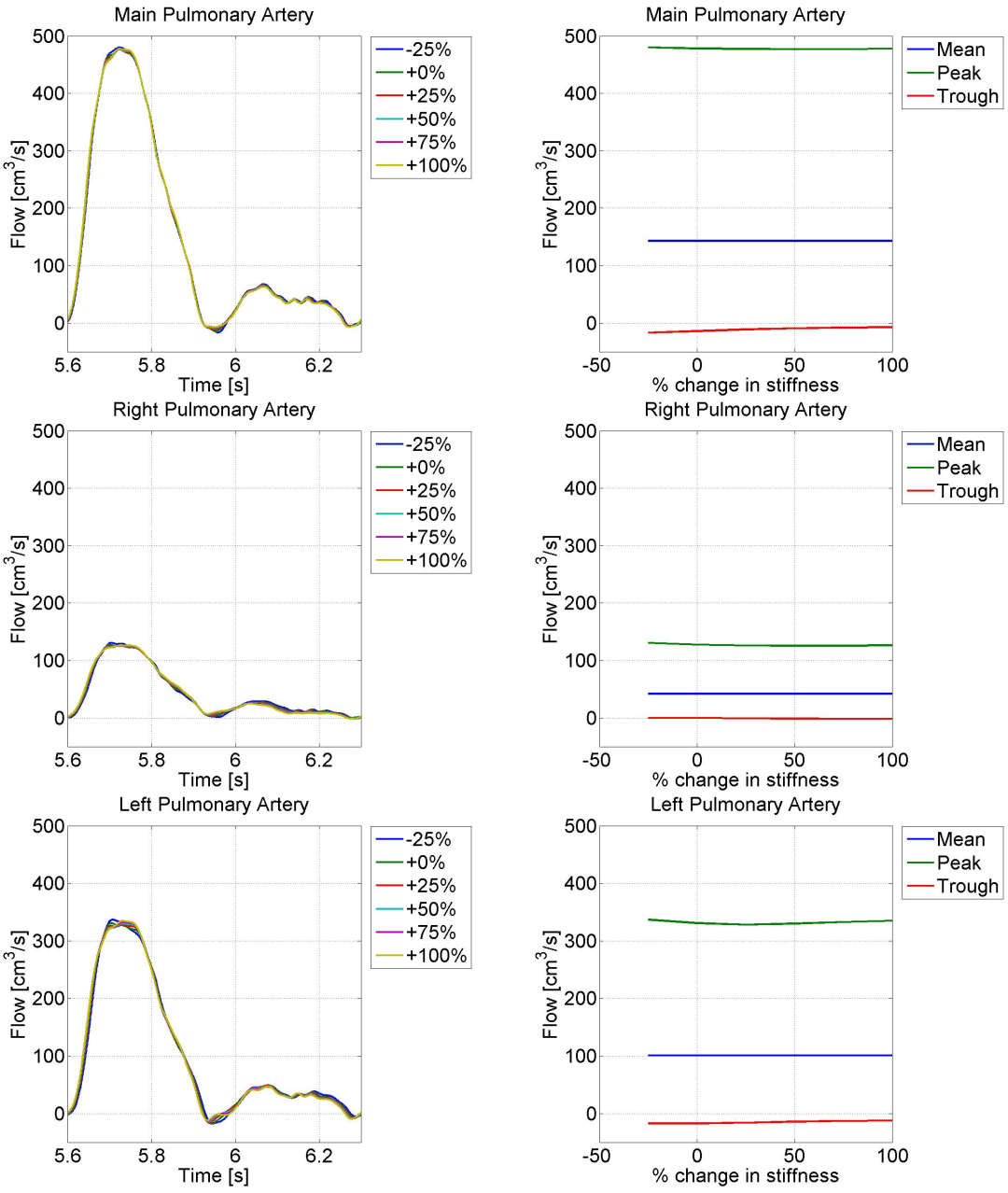

Figure 6.37: Effects of changing both large and small vessel compliance on Pulmonary Artery Flow.

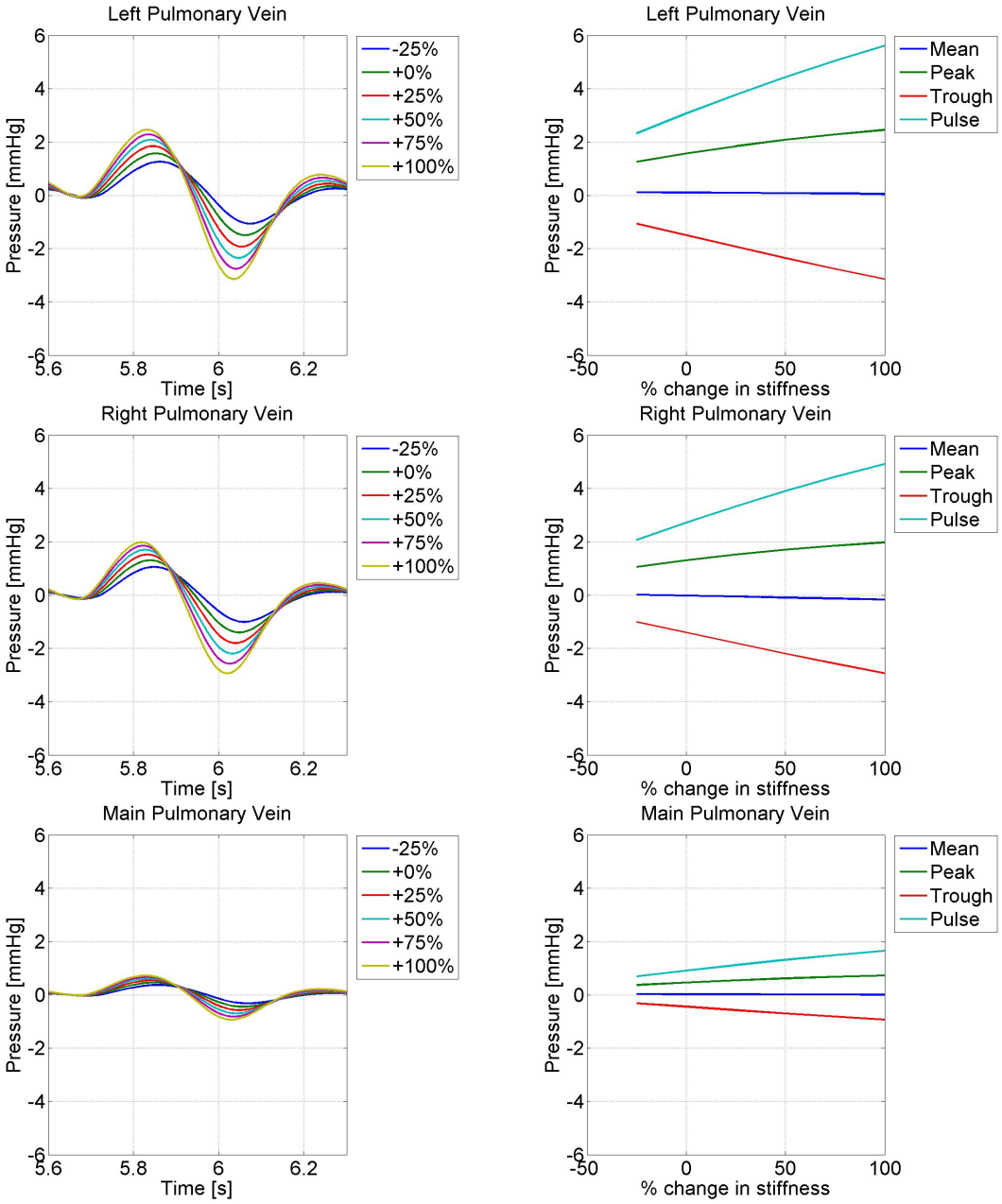

Figure 6.38: Effects of changing both large and small vessel compliance on Pulmonary Venous Pressure.

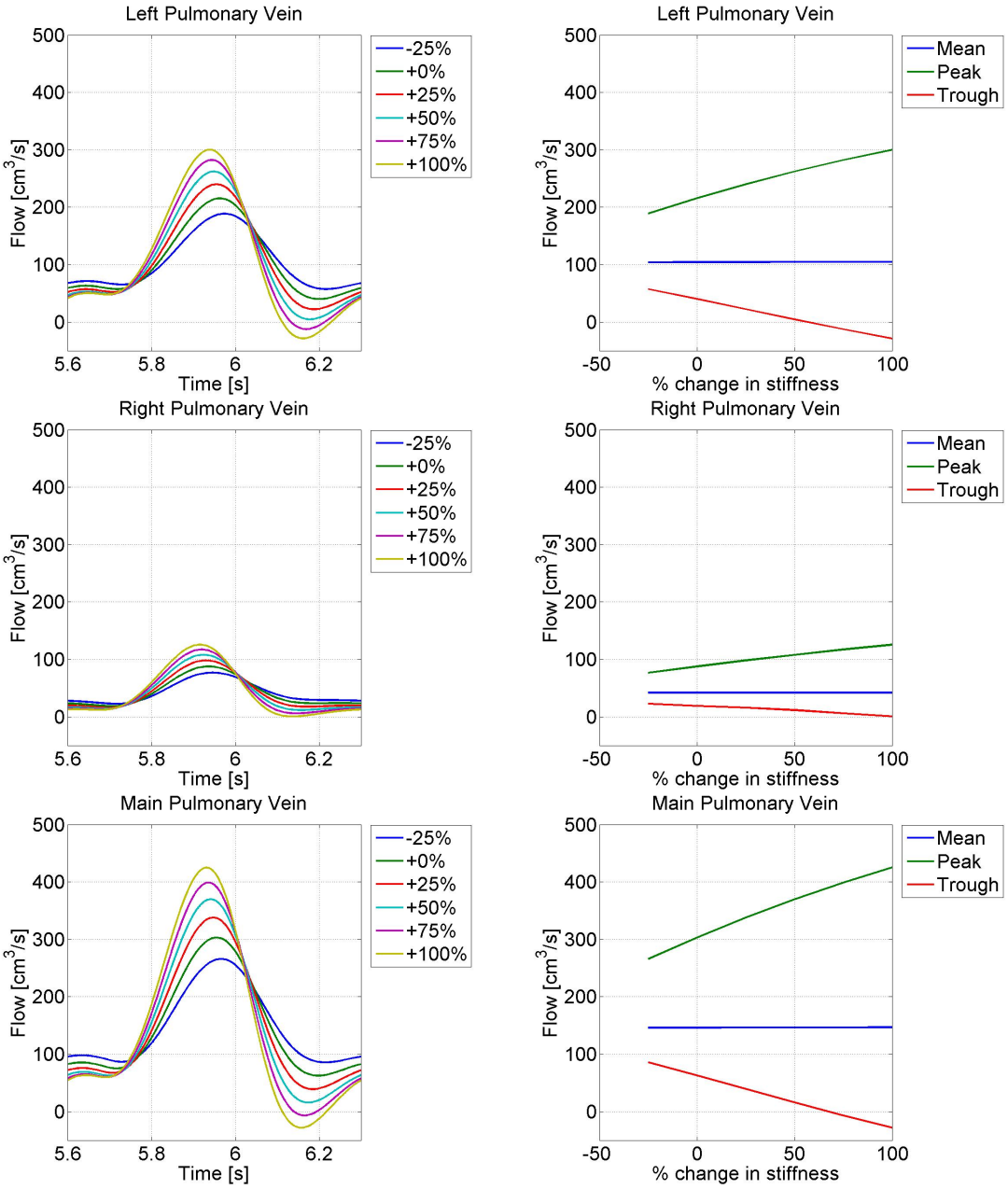

Figure 6.39: Effects of changing both large and small vessel compliance on Pulmonary Venous Flow.

Chapter 7

Conclusions and Discussion

The first aim of the work in this thesis was to further develop the model of Olufsen, with particular reference to the small arteries. In Sections 3.1 and 3.2 we used the systemic arterial model to examine the hypotheses of two conditions linked to systolic hypertension. We saw how the stiffening of the arterial vessel walls, and the rarefaction of the microcirculation both resulted in increased pressure in our simulations in the large arteries. The second case, in particular, showed the advantage of being able to model the small vessels when compared with other models using a lumped peripheral resistance outflow condition.

In Section 3.3 we derived new equations, as an extension to Olufsen's model, to explicitly determine flow and pressure profiles in the small arteries of the systemic circulation. We showed that a steep drop in pressure occurs over a range of arteries of around 0.030-0.050cm radius, which is in agreement with clinical observation and estimations of the location of the resistance arteries. However, clinical observations also suggest that the pressure drop tails off over vessels of around 0.001-0.010cm radius, which is not seen in our model due to the termination of the structured tree at vessels of 0.010cm radius, above capillary level, forcing the pressure to go to zero at this point. A simple improvement to rectify this would be to section the structured tree model by vessel radius into three parts — the arteries, arterioles and capillaries — each with different structural and physical properties. We believe that this would produce a more accurate simulation of the pressure drop over the small arteries.

The second aim of the work in this thesis was to develop a new model of the pulmonary circulation, including detailed flow and pressure simulations in the large pulmonary arteries and veins, with a new model for connecting an arterial and venous tree. Over the course of Section 3.4, and Chapters 4 and 5 we described the properties of the pulmonary arteries

(and constructed a stand alone pulmonary arterial model), derived the new equations for determining the admittance matrix of a connected network of arterial and venous trees, and described the properties of the small pulmonary vessels and large pulmonary veins. This allowed us to construct a new model of the pulmonary circulation, for which we defined normal conditions at the start of Chapter 6. This model displayed the characteristics expected in the pulmonary circulation — little change in the amplitude of the pressure pulse along the pulmonary arteries, and a low amplitude but visible pressure pulse in the pulmonary veins.

In Section 6.2 we tested several hypotheses underlying the pathogenesis of hypertensive disorders in the pulmonary circulation. In each case, changes away from the normal conditions of the pulmonary circulation in line with the hypotheses resulted in increases in the systolic pressure predicted in the pulmonary arteries. In simulating the hypothesis of pulmonary arterial hypertension (Section 6.2.1) and chronic thromboembolic pulmonary hypertension (Section 6.2.4) in particular, our results were in good agreement with clinical observations. The addition of a venous circulation to our model allowed us to better investigate pulmonary venous hypertension (Section 6.2.2), and to simulate venous flows and pressures in each abnormal situation.

Limitations of the current model and further work

The most notable limitation of the current model is the lack of available data for validation. While clinical measurements of pulmonary flow and pressure in normal and abnormal conditions [27] have been used to provide some validation (Section 6.2), an ideal scenario would be to use MRI flow measurements from the same subject in each of the main pulmonary artery (for model inflow, as is already used), further down the arterial tree in the left and right pulmonary arteries (for model validation), and if possible also in the pulmonary veins for further validation.

A further limitation of the structured tree model is that there is currently no allowance for the possibility of trifurcations in the branching structure. While bifurcations are far more prevalent, trifurcations can and do occur in the pulmonary anatomy, and so a potential improvement to the model would be to add an allowance for this.

It has already been mentioned that the model for predicting pressure in the small systemic arteries could be improved by sectioning the structured tree model, and including a

capillary model, which would allow greater insight into the function of the microcirculation. Similarly, the effects of the pulmonary capillaries are not included in our pulmonary circulation model. Instead, the arterial tree is joined directly to the venous tree with no accounting for the complex network of tiny vessels around the alveoli. Theory exists [14], [15] as to the structure of, and flow in, these tiny vessels, and it is possible that they have an effect on the resistance in, and pressure drop across, the pulmonary circulation. We saw at the beginning of Chapter 6 that when we reduce the minimum radius of our structured trees to include capillary, or near-capillary sized vessels, the predicted pressure in the pulmonary arteries rises well above physiological values, proving that the structured tree model is not a suitable one for describing the capillaries.

It has been suggested, however, that the effect of the pulmonary microcirculation on the input impedance of the larger vessels is small, but that the effect on the phase difference between the pressure and flow in these arteries is large [16]. As such, the development and inclusion of a new model to describe flow in the capillary network around the alveoli would greatly enhance the pulmonary circulation model.

The description of the large pulmonary veins used in the pulmonary circulation model is largely a mirror image of the large pulmonary arteries. This is justifiable as the arterial, venous and brachial trees generally follow the same closely linked branching structure, however the venous tree does not reconverge to a single vessel as the model suggests, but rather four large pulmonary veins drain blood into the left atrium. The model could be improved with a new description of the largest pulmonary veins, with four outflow conditions at the end of the four largest pulmonary veins, rather than the one that is currently used.

The outflow condition itself may also be improved upon. Currently, the outflow condition for blood draining from the pulmonary veins into the left atrium is that the pressure at this point is zero. However, while the pressure at this point is indeed minuscule, the beating of the heart and resulting opening and closing of the valve at the entrance to the left atrium means that fluid periodically collects, and then drains away, in the pulmonary veins, and a new outflow condition to describe this would also improve the validity of the model.

The above mentioned outflow condition could also be improved as part of a solution to an issue that affects both the pulmonary and systemic models, namely that the inflow condition is given as a prescribed flow into the largest artery over time. This means that

the inflow to the model, i.e. the output from the heart, can not and does not react to any stimuli that may occur elsewhere in the system — the heart rate stays the same, and cardiac output never increases nor decreases. This is particularly limiting to the current model when attempting to model diseased states of the cardiovascular system. Further, the imposed inflow profile may contain encoded information which may adversely affect the predictions of the simulated flows and pressures further down the tree. A dynamic heart model controlling cardiac output (and, in phase, venous return in the pulmonary circulation model) would be the most significant advancement that could be made to these circulation models.

These models have been demonstrated to be both interesting and useful, as confirmed by our clinical collaborators, but it is also clear that there is still scope for improvement to them which would further enhance their credibility as useful and accurate clinical model, and possibly even a diagnostic tool.

Appendix A

Lax-Wendroff Scheme

In conservation form, the equations to be solved are,

$$\frac{\partial}{\partial t}\mathbf{U} + \frac{\partial}{\partial x}\mathbf{R} = \mathbf{S}, \tag{A.1}$$

where the dependent variables are represented by

$$\mathbf{U} = \begin{pmatrix} A \\ q \end{pmatrix}, \tag{A.2}$$

the system flux by,

$$\mathbf{R} = \begin{pmatrix} q \\ \frac{q^2}{A} + B \end{pmatrix}, \tag{A.3}$$

and the right hand side of the equation by

$$\mathbf{S} = \begin{pmatrix} 0 \\ \frac{-2\pi r_0}{\delta \mathcal{R}} \frac{q}{A} + \left(2\sqrt{A}\left(\sqrt{\pi} f + \sqrt{A_0}\frac{df}{dr_0}\right)\frac{dr_0}{dx}\right) \end{pmatrix}. \tag{A.4}$$

Equations

Let $\mathbf{U}_m^n = \mathbf{U}(m\Delta x, n\Delta t)$, and similarly for $\mathbf{R}$ and $\mathbf{S}$. The solution at all points in the interior is determined by first determining some intermediate values at steps $(m+1/2, n+1/2)$. Using a uniform grid, we can derive a four point formula, predicting the flow at time level $(n+1)$ as follows,

$$\mathbf{U}_m^{n+1} = \mathbf{U}_m^n - \frac{\Delta t}{\Delta x}\left(\mathbf{R}_{m+1/2}^{n+1/2} + \mathbf{R}_{m-1/2}^{n+1/2}\right) + \frac{\Delta t}{2}\left(\mathbf{S}_{m+1/2}^{n+1/2} + \mathbf{S}_{m-1/2}^{n+1/2}\right). \tag{A.5}$$

Using two intermediate points at time level $(n+1/2)$, and using (A.3) and (A.4), it is possible to determine,

$$\begin{matrix} \mathbf{R}_{m+1/2}^{n+1/2} & \mathbf{S}_{m+1/2}^{n+1/2} \\ \mathbf{R}_{m-1/2}^{n+1/2} & \mathbf{S}_{m-1/2}^{n+1/2} \end{matrix}$$

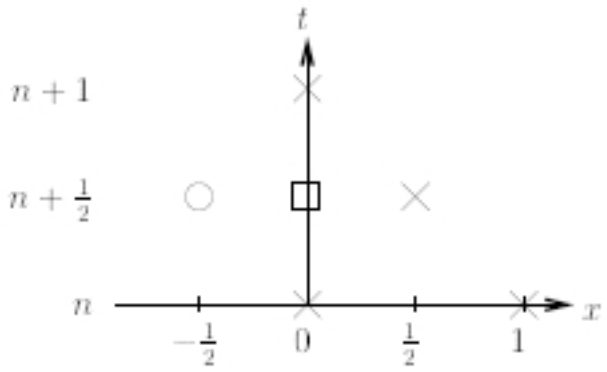

Figure A.1: Ghost point, marked with a circle, at distance point $-1/2$ – a half step before the opening of a vessel – and at time-step $n+1/2$. Points marked with a cross are already known, and the point marked with a square is found by averaging between its adjacent time-steps.

This is done using the definition,

$$\mathbf{U}_j^{n+1/2} = \frac{\mathbf{U}_{j+1/2}^n + \mathbf{U}_{j-1/2}^n}{2} + \frac{\Delta t}{2}\left(-\frac{\mathbf{R}_{j+1/2}^n - \mathbf{R}_{j-1/2}^n}{h} + \frac{\mathbf{S}_{j+1/2}^n + \mathbf{S}_{j-1/2}^n}{2}\right) \tag{A.6}$$

for $j = m + 1/2$ and $j = m - 1/2$.

A.1 Inflow Condition

The inflow into the system is described by a periodic function, Figure 2.3. Also, A will be determined from the boundary condition for q. In order to find A, we need to evaluate $q_{1/2}^{n+1/2}$. This can be found by introducing a ghost point, see Figure A.1. Then,

$$q_0^{n+1/2} = \frac{1}{2}\left(q_{-1/2}^{n+1/2} + q_{1/2}^{n+1/2}\right) \tag{A.7}$$

$$\Leftrightarrow q_{-1/2}^{n+1/2} = 2q_0^{n+1/2} - q_{1/2}^{n+1/2}, \tag{A.8}$$

and from (A.5),

$$A_0^{n+1} = A_0^n - \frac{\Delta x}{\Delta t}\left((R_1)_{1/2}^{n+1/2} - (R_1)_{-1/2}^{n+1/2}\right) + \frac{\Delta t}{2}\left((S_1)_{1/2}^{n+1/2} + (S_1)_{-1/2}^{n+1/2}\right), \tag{A.9}$$

where $(R_1)_{-1/2}^{n+1/2} = q_{-1/2}^{n+1/2}$ and $(S_1)_{-1/2}^{n+1/2} = 0$.

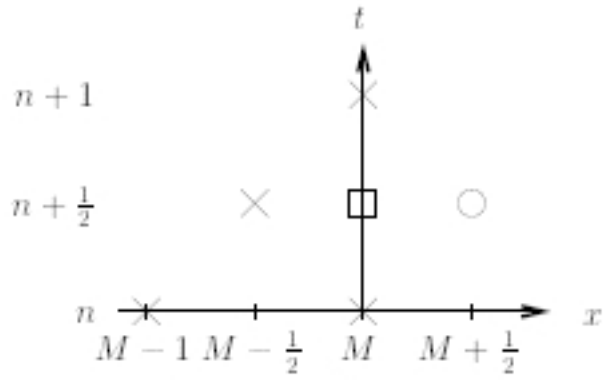

Figure A.2: Ghost point, marked with a circle, at distance point $M + 1/2$ – a half step beyond the end of a vessel – and at time-step $n + 1/2$. Points marked with a cross are already known, and the point marked with a square is found by averaging between its adjacent time-steps.

A.2 Bifurcation Condition and Systemic Outflow Condition

The numerical equations for a bifurcation boundary, and for the systemic outflow boundary, are described in detail in [32]. Since these have not been altered in any of the models described in this thesis, a full description has not been included here.

A.3 (Pulmonary) Matching Condition

Arterial Side

On the arterial side of the matching boundary, the convolution integral can be written as,

$$q_A(M\Delta x, t) = \int_0^T \left(p_A(M\Delta x, t-\tau)y_{11}(M\Delta x, \tau) + p_V(0, t-\tau)y_{12}(M\Delta x, \tau)\right) d\tau, \quad \text{(A.10)}$$

where the subscripts A and V denote the arterial and venous sides of the matching boundary respectively, and the matrix $\mathbf{Y}$ relates the flow and pressure on either side of the matching boundary by,

$$\begin{pmatrix} q_A \\ q_V \end{pmatrix} = \begin{pmatrix} y_{11} & y_{12} \\ y_{21} & y_{22} \end{pmatrix} \begin{pmatrix} p_A \\ p_V \end{pmatrix}.$$

Equation (A.10) can be discretised by,

$$q_M^n = \left(p_A(M, A_M^n)(y_{11})^0 + p_V(0, A_0^n)(y_{12})^0\right)\Delta t + (q_{tms}^A)_M^n, \quad \text{(A.11)}$$

where the current time is $t = n\Delta t$ and,

$$(q^A_{tms})^n_M = \sum_{k=1}^{N-1} \left((p_A)^{<n-k>_N}_M y^k_{11} + (p_V)^{<n-k>_N}_M y^k_{12} \right) \Delta t. \tag{A.12}$$

Here, N is the number of time-steps per period, and $< \cdot >_N$ denotes the modulo operator, the range of which is the set $\{0, 1, \ldots, N-1\}$.

From the numerical scheme, (A.5), we had,

$$\begin{aligned} A^{n+1}_M &= A^n_M - \frac{\Delta x}{\Delta t}\left((R_1)^{n+1/2}_{M+1/2} - (R_1)^{n+1/2}_{M-1/2} \right) + \frac{\Delta t}{2}\left((S_1)^{n+1/2}_{M+1/2} + (S_1)^{n+1/2}_{M-1/2} \right) & \text{(A.13)} \\ &= A^n_M - \frac{\Delta x}{\Delta t}\left((R_1)^{n+1/2}_{M+1/2} - (R_1)^{n+1/2}_{M-1/2} \right), & \text{(A.14)} \end{aligned}$$

since $S_1 = 0$, and

$$q^{n+1}_M = q^n_M - \frac{\Delta x}{\Delta t}\left((R_2)^{n+1/2}_{M+1/2} - (R_2)^{n+1/2}_{M-1/2} \right) + \frac{\Delta t}{2}\left((S_2)^{n+1/2}_{M+1/2} + (S_2)^{n+1/2}_{M-1/2} \right). \tag{A.15}$$

The unknowns in these equations are q^{n+1}_M, A^{n+1}_M, $(R_1)^{n+1/2}_{M+1/2}$, $(R_2)^{n+1/2}_{M+1/2}$, and $(S_2)^{n+1/2}_{M+1/2}$. As for the inflow boundary, these can be determined by establishing a ghost point, see Figure A.2, such that,

$$\begin{aligned} A^{n+1/2}_M &= \frac{1}{2}\left(A^{n+1/2}_{M-1/2} + A^{n+1/2}_{M+1/2} \right), & \text{(A.16)} \\ \text{and } q^{n+1/2}_M &= \frac{1}{2}\left(q^{n+1/2}_{M-1/2} + q^{n+1/2}_{M+1/2} \right). & \text{(A.17)} \end{aligned}$$

These equations add two more unknowns to the system, namely $q^{n+1/2}_M$ and $A^{n+1/2}_M$. These can be found using the boundary condition at the time levels $n + 1/2$ and $n + 1$,

$$\begin{aligned} q^{n+1/2}_M &= \left(p_A(M, A^{n+1/2}_M)(y_{11})^0 + p_V(L, A^{n+1/2}_L)(y_{12})^0 \right) \Delta t + (q^A_{tms})^{n+1/2}_M & \text{(A.18)} \\ \text{and } q^{n+1}_M &= \left(p_A(M, A^{n+1}_M)(y_{11})^0 + p_V(L, A^{n+1}_L)(y_{12})^0 \right) \Delta t + (q^A_{tms})^{n+1}_M. & \text{(A.19)} \end{aligned}$$

Venous Side

By following an identical argument as for the arterial side of the matching boundary, we find the following six equations for the venous side of the matching boundary for a vessel of length $L\Delta x$,

$$A^{n+1}_L = A^n_L - \frac{\Delta x}{\Delta t}\left((R_1)^{n+1/2}_{L+1/2} - (R_1)^{n+1/2}_{L-1/2} \right), \tag{A.20}$$

$$q^{n+1}_L = q^n_L - \frac{\Delta x}{\Delta t}\left((R_2)^{n+1/2}_{L+1/2} - (R_2)^{n+1/2}_{L-1/2} \right) + \frac{\Delta t}{2}\left((S_2)^{n+1/2}_{L+1/2} + (S_2)^{n+1/2}_{L-1/2} \right), \tag{A.21}$$

$$A^{n+1/2}_L = \frac{1}{2}\left(A^{n+1/2}_{L-1/2} + A^{n+1/2}_{L+1/2} \right), \tag{A.22}$$

$$q_L^{n+1/2} = \frac{1}{2}\left(q_{L-1/2}^{n+1/2} + q_{L+1/2}^{n+1/2}\right), \tag{A.23}$$

$$q_L^{n+1/2} = \left(p_A(M, A_M^{n+1/2})(y_{21})^0 + p_V(L, A_L^{n+1/2})(y_{22})^0\right)\Delta t + (q_{tms}^V)_L^{n+1/2}, \tag{A.24}$$

and

$$q_L^{n+1} = \left(p_A(M, A_M^{n+1})(y_{21})^0 + p_V(L, A_L^{n+1})(y_{22})^0\right)\Delta t + (q_{tms}^V)_L^{n+1}. \tag{A.25}$$

Solving the equations.

The twelve equations (A.14 - A.19) and (A.20 - A.25) have the following twelve unknowns,

$$\begin{array}{cccccc} A_M^{n+1} & q_M^{n+1} & A_M^{n+1/2} & q_M^{n+1/2} & A_{M+1/2}^{n+1/2} & q_{M+1/2}^{n+1/2} \\ A_L^{n+1} & q_L^{n+1} & A_L^{n+1/2} & q_L^{n+1/2} & A_{L+1/2}^{n+1/2} & q_{L+1/2}^{n+1/2} \end{array}$$

The number of equations can be reduced by substituting (A.16), (A.17) and (A.22) into (A.18), and by substituting (A.16), (A.22) and (A.23) into (A.24). Hence (A.18) and (A.24) can be written as,

$$\frac{q_{M-1/2}^{n+1/2}+q_{M+1/2}^{n+1/2}}{2} = \left(p_A(M, \frac{A_{M-1/2}^{n+1/2}+A_{M+1/2}^{n+1/2}}{2})(y_{11})^0 + p_V(L, \frac{A_{L-1/2}^{n+1/2}+A_{L+1/2}^{n+1/2}}{2})(y_{12})^0\right)\Delta t + (q_{tms}^A)_M^{n+1/2}, \tag{A.26}$$

and

$$\frac{q_{L-1/2}^{n+1/2}+q_{L+1/2}^{n+1/2}}{2} = \left(p_A(M, \frac{A_{M-1/2}^{n+1/2}+A_{M+1/2}^{n+1/2}}{2})(y_{21})^0 + p_V(L, \frac{A_{L-1/2}^{n+1/2}+A_{L+1/2}^{n+1/2}}{2})(y_{22})^0\right)\Delta t + (q_{tms}^V)_L^{n+1/2}. \tag{A.27}$$

Thus, the eight equations to be solved are (A.14), (A.15), (A.19), (A.20), (A.21), (A.25), (A.26) and (A.27) with unknowns

$$\begin{array}{cccc} x_1 = A_M^{n+1}, & x_2 = q_M^{n+1}, & x_3 = A_{M+1/2}^{n+1/2}, & x_4 = q_{M+1/2}^{n+1/2}, \\ x_5 = A_L^{n+1}, & x_6 = q_L^{n+1}, & x_7 = A_{L+1/2}^{n+1/2}, & x_8 = q_{L+1/2}^{n+1/2}, \end{array}$$

and initial guesses,

$$\begin{array}{cccc} (x_1)_0 = A_{M-1/2}^{n+1/2}, & (x_2)_0 = q_{M-1/2}^{n+1/2}, & (x_3)_0 = A_M^n, & (x_4)_0 = q_M^n, \\ (x_5)_0 = A_{L-1/2}^{n+1/2}, & (x_6)_0 = q_{L-1/2}^{n+1/2}, & (x_7)_0 = A_L^n, & (x_8)_0 = q_L^n. \end{array}$$

Newton Scheme - Residual Equations

Equation (A.14) becomes,

$$(fr)_1 = k_1 - x_1 - \theta x_4, \tag{A.28}$$

where

$$\theta = \Delta x/\Delta t,$$

and

$$k_1 = A_M^n + \theta(R_1)_{M-1/2}^{n+1/2}.$$

Equation (A.15) becomes,

$$(fr)_2 = k_2 - x_2 - \theta\left(\frac{x_4^2}{x_3} + B(M+1/2, x_3)\right) + \gamma\left(F(M+1/2, x_4, x_3) + \frac{dB(M+1/2, x_3)}{dx}\right), \tag{A.29}$$

where

$$\gamma = \Delta t/2,$$

$$k_2 = q_M^n + \theta(R_2)_{M-1/2}^{n+1/2} + \gamma(S_2)_{M-1/2}^{n+1/2},$$

$$B(M+1/2, x_3) = f(r_0)_{M+1/2}\sqrt{x_3(A_0)_{M+1/2}},$$

$$F(M+1/2, x_4, x_3) = \frac{-2\pi(r_0)_{M+1/2}}{\delta R}\frac{x_4}{x_3},$$

and

$$\frac{dB(M+1/2, x_3)}{dx} = \left(\frac{dB}{dr_0}\frac{dr_0}{dx}\right)_{M+1/2}^{n+1/2} = \left(2\sqrt{x_3}\left(\sqrt{\pi}f(r_0) + \sqrt{A_0}\frac{df}{dr_0}\right) - A\frac{df}{dr_0}\right)_{M+1/2}\left(\frac{dr_0}{dx}\right)_{M+1/2}.$$

Equation (A.19) becomes,

$$(fr)_3 = k_3 - x_2 + k_4 p_A(M, x_1) + k_5 p_V(L, x_5), \tag{A.30}$$

where

$$k_3 = (q_{tms}^A)_M^{n+1},$$

$$k_4 = (y_{11})^0\Delta t,$$

and

$$k_5 = (y_{12})^0\Delta t.$$

Equation (A.20) becomes,

$$(fr)_4 = k_6 - x_5 - \theta x_8, \tag{A.31}$$

where

$$\theta = \Delta x/\Delta t,$$

and

$$k_6 = A_L^n + \theta(R_1)_{L-1/2}^{n+1/2}.$$

Equation (A.21) becomes,

$$(fr)_5 = k_7 - x_6 - \theta\left(\frac{x_8^2}{x_7} + B(L+1/2, x_7)\right) + \gamma\left(F(L+1/2, x_8, x_7) + \frac{dB(L+1/2, x_7)}{dx}\right), \tag{A.32}$$

where

$$\gamma = \Delta t/2,$$

$$k_7 = q_L^n + \theta(R_2)_{L-1/2}^{n+1/2} + \gamma(S_2)_{L-1/2}^{n+1/2},$$

$$B(L+1/2, x_7) = f(r_0)_{L+1/2}\sqrt{x_7(A_0)_{L+1/2}},$$

$$F(L+1/2, x_8, x_7) = \frac{-2\pi(r_0)_{L+1/2}}{\delta R}\frac{x_8}{x_7},$$

and

$$\frac{dB(L+1/2, x_7)}{dx} = \left(\frac{dB}{dr_0}\frac{dr_0}{dx}\right)_{L+1/2}^{n+1/2} = \left(2\sqrt{x_7}\left(\sqrt{\pi}f(r_0) + \sqrt{A_0}\frac{df}{dr_0}\right) - A\frac{df}{dr_0}\right)_{L+1/2}\left(\frac{dr_0}{dx}\right)_{L+1/2}.$$

Equation (A.25) becomes,

$$(fr)_6 = k_8 - x_6 + k_9 p_A(M, x_1) + k_{10} p_V(L, x_5), \tag{A.33}$$

where

$$k_8 = (q_{tms}^V)_L^{n+1},$$

$$k_9 = (y_{12})^0 \Delta t,$$

and

$$k_{10} = (y_{22})^0 \Delta t.$$

Equation (A.26) becomes,

$$(fr)_7 = k_{11} - \frac{x_4}{2} + k_4 p_A(M, (k_{12} + x_3)/2) + k_5 p_V(L, (k_{13} + x_7)/2), \tag{A.34}$$

where

$$k_{11} = (q_{tms}^A)_M^{n+1/2} - 1/2(q_{M-1/2}^{n+1/2}),$$

$$k_{12} = A_{M-1/2}^{n+1/2},$$

and

$$k_{13} = A_{L-1/2}^{n+1/2}.$$

Equation (A.27) becomes,

$$(fr)_8 = k_{14} - \frac{x_8}{2} + k_9 p_A(M, (k_{12} + x_3)/2) + k_{10} p_V(L, (k_{13} + x_7)/2), \tag{A.35}$$

where

$$k_{14} = (q_{tms}^V)_L^{n+1/2} - 1/2(q_{L-1/2}^{n+1/2}).$$

Newton Scheme - Jacobian

$$\begin{pmatrix} -1 & 0 & 0 & -\theta & 0 & 0 & 0 & 0 \\ 0 & -1 & \xi_1 & \xi_2 & 0 & 0 & 0 & 0 \\ \xi_3 & -1 & 0 & 0 & \xi_4 & 0 & 0 & 0 \\ 0 & 0 & 0 & 0 & -1 & 0 & 0 & -\theta \\ 0 & 0 & 0 & 0 & 0 & -1 & \xi_5 & \xi_6 \\ \xi_7 & 0 & 0 & 0 & \xi_8 & -1 & 0 & 0 \\ 0 & 0 & \xi_9 & -\frac{1}{2} & 0 & 0 & \xi_{10} & 0 \\ 0 & 0 & \xi_{11} & 0 & 0 & 0 & \xi_{12} & -\frac{1}{2} \end{pmatrix} \tag{A.36}$$

where,

$$\begin{aligned}
\xi_1 &= \theta\left(\left(\frac{x_4}{x_3}\right)^2 - \frac{dB(M+1/2,x_3)}{dx_3}\right) + \gamma\left(\frac{dF(M+1/2,x_4,x_3)}{dx_3} + \frac{d^2B(M+1/2,x_3)}{dxdx_3}\right), \\
\xi_2 &= -\theta\frac{2x_4}{x_3} + \gamma\frac{dF(M+1/2,x_4,x_3)}{dx_4}, \\
\xi_3 &= k_4\frac{dP_A(M,x_1)}{dx_1}, \\
\xi_4 &= k_5\frac{dP_V(L,x_5)}{dx_5}, \\
\xi_5 &= \theta\left(\left(\frac{x_8}{x_7}\right)^2 - \frac{dB(L+1/2,x_7)}{dx_7}\right) + \gamma\left(\frac{dF(L+1/2,x_8,x_7)}{dx_7} + \frac{d^2B(L+1/2,x_7)}{dxdx_7}\right), \\
\xi_6 &= -\theta\frac{2x_8}{x_7} + \gamma\frac{dF(L+1/2,x_8,x_7)}{dx_8}, \\
\xi_7 &= k_9\frac{dP_A(M,x_1)}{dx_1}, \\
\xi_8 &= k_{10}\frac{dP_V(L,x_5)}{dx_5}, \\
\xi_9 &= k_4\frac{dP_A(M,(k_{12}+x_3)/2)}{dx_3}, \\
\xi_{10} &= k_5\frac{dP_V(L,(k_{13}+x_7)/2)}{dx_7}, \\
\xi_{11} &= k_9\frac{dP_A(M,(k_{12}+x_3)/2)}{dx_3}, \\
\xi_{12} &= k_{10}\frac{dP_V(L,(k_{13}+x_7)/2)}{dx_7}.
\end{aligned}$$

A.4 (Pulmonary) Outflow Condition

In contrast to the inflow to the system, at the outflow from the system the area A is know, but the flow q is unknown and will be determined from the boundary condition for A. In order to do this, we need to evaluate $A^{n+1/2}_{M+1/2}$ by again using a ghost point, see Figure A.2. Then,

$$A^{n+1/2}_{M} = \frac{1}{2}\left(A^{n+1/2}_{M-1/2} + A^{n+1/2}_{M+1/2}\right) \tag{A.37}$$

$$\Leftrightarrow A^{n+1/2}_{M-1/2} = 2A^{n+1/2}_{M} - A^{n+1/2}_{M+1/2}. \tag{A.38}$$

Now, (A.5) tells us that,

$$q^{n+1}_{M} = q^{n}_{M} - \frac{\Delta x}{\Delta t}\left((R_2)^{n+1/2}_{M+1/2} - (R_2)^{n+1/2}_{M-1/2}\right) + \frac{\Delta t}{2}\left((S_2)^{n+1/2}_{M+1/2} + (S_2)^{n+1/2}_{M-1/2}\right), \tag{A.39}$$

where $(R_2)^{n+1/2}_{M+1/2}$ and $(S_2)^{n+1/2}_{M+1/2}$ are given by (A.3) and (A.4) respectively. (A.5) also tells us that,

$$A^{n+1}_{M} = A^{n}_{M} - \frac{\Delta x}{\Delta t}\left((R_1)^{n+1/2}_{M+1/2} - (R_1)^{n+1/2}_{M-1/2}\right) + \frac{\Delta t}{2}\left((S_1)^{n+1/2}_{M+1/2} + (S_1)^{n+1/2}_{M-1/2}\right)$$

$$\Rightarrow q^{n+1/2}_{M+1/2} = \frac{\Delta t}{\Delta x}\left(A^{n}_{M} - A^{n+1}_{M}\right) + q^{n+1/2}_{M-1/2}, \tag{A.40}$$

since $(R_1)^{n}_{m} = q^{n}_{m}$ and $(S_1)^{n}_{m} = 0$.

Equations (A.38), (A.39) and (A.40) provide us with a system of 3 equations for the three unknowns $A^{n+1/2}_{M+1/2}$, $q^{n+1/2}_{M+1/2}$, and most importantly, q^{n+1}_{M}.

Appendix B

Generations and Orders in Branching Trees

The 'generation' and 'order' of a branching tree are two similar, but not identical concepts. A 'vessel' is a segment of a branching tree between two points of bifurcation, have a parent and two daughter vessels - except in the case of the root vessel, which has two daughters but no parent vessel, and in the case of terminal vessels, which have a parent vessel but no daughters.

The 'generation' of a tree of vessels, or the 'generation number' of a vessel in the tree, as used by Weibel [53], simply describes the number of points of bifurcation between a particular vessel and the root vessel. The generation number of a vessel in the tree will always be one greater than its parent vessel - so the root vessel is generation 0, its daughter vessels are generation 1, their daughters are generation 2, and so on.

In the structured tree model used by Olufsen, and in our pulmonary model, the asymmetric nature of the branching tree means that terminal vessels of the tree can exist over a wide range of generations, and that vessels of the same generation may be of widely varying lengths and radii. This means that there is little or no relation between generation and properties such as lengths and radii of vessel segments. As such, most studies on the morphometry of smaller vessels use an ordering system such as the ones described below to index the vessels of a branching tree, and data from these, such as lengths as radii, is presented as an average for a particular order rather than a particular generation as vessels of the same order are more likely to be similar.

B.1 The Strahler Ordering System

In the popular Strahler system [14], [20], [46] of ordering vessels in a branching tree, the smallest vessels (terminal vessels) of the tree are said to be of order 1. When two vessels of order 1 meet, the next largest vessel is a vessel of order 2. Two vessels of order 2 meet to form a larger vessel of order 3, etc. However, if an order 1 vessel meets an order 2 vessel, the larger combined vessel remains of order 2. Similarly, if an order 2 vessel and and order 3 vessel meet, the combined trunk's order remains at 3, and so on.

If the branching tree is of a binary symmetric form, i.e. every vessel gives birth to two identical daughter vessels, then the tree will have the same number of orders as it does generations (albeit numbered from opposite ends). However, this is very rarely the case in physiological situations.

B.2 The Diameter-Defined Strahler Ordering System

A variation on the previously mentioned ordering system is the diameter-defined Strahler system. Again, in this system, the smallest vessels are said to be of order 1, and two order 1 vessels combine to form a vessel of order 2, etc, but a vessel of order 1 and a vessel of order 2 may combine to form a vessel of order 2 (as in the normal Strahler system), or of order 3 if the diameter of the confluent vessel is greater than a certain value [23]. This means that, in general, the diameter-defined Strahler system leads to more orders in the branching tree than the normal Strahler method would describe. Once again, however, if the tree is a binary symmetric tree, then the Strahler and diameter-defined Strahler orders are identical, and there are again the same number of orders as generations.

References

[1] C. Acott. The diving "law-ers" a brief resume of their lives. *SPUMS Journal*, 29(1), 1999.

[2] T.F. Antonios, F.M. Rattray, D.R. Singer, N.D. Markandu, P.S. Mortimer, and G.A. MacGregor. Rarefaction of skin capillaries in normotensive offspring of individuals with essential hypertension. *Heart*, 89:175–178, 2003.

[3] K. Azer and C.S. Peskin. A one-dimensional model of blood flow in arteries with friction and convection based on the Womersley velocity profile. *Cardiovasc Eng*, 7:51–73, 2007.

[4] R.J. Barst, M. McGoon, A. Torbicki, O. Sitbon, M.J. Krowka, H. Olschewski, and S. Gaine. Diagnosis and differential assessment of pulmonary arterial hypertension. *J Am Coll Cardiol*, 43:40S–47S, 2004.

[5] K.S. Burrowes, P.J. Hunter, and M.H. Tawhai. Anatomically based finite element models of the human pulmonary arterial and venous trees including supernumerary vessels. *J Appl Physiol*, 99:731–738, 2005.

[6] K.S. Burrowes and M.H. Tawhai. Computational predictions of pulmonary blood flow gradients: Gravity versus structure. *Resp Physiol Neurobiol*, 154:515–523, 2006.

[7] V. Castelain, P. Herve, Y. Lecarpentier, P. Duroux, G. Simonneau, and D. Chemla. Pulmonary artery pulse pressure and wave reflection in chronic pulmonary thromboembolism and primary pulmonary hypertension. *J Am Coll Cardiol*, 7(4):1085–1092, 2001.

[8] C.P. Cheng, R.J. Herfkens, A.L. Lightner, C.A. Taylor, and J.A. Feinstein. Blood flow conditions in the proximal pulmonary arteries and vena cavae: healthy children

during upright cycling exercise. *Am J Physiol Heart Circ Physiol*, 287:H921–H926, 2004.

[9] C.P. Cheng, R.J. Herfkens, and J.A. Taylor, C.A. andd Feinstein. Proximal pulmonary artery blood flow characteristics in healthy subjects measured in an upright posture using MRI: The effects of exercise and age. *J Magn Res Img*, 21:752–758, 2005.

[10] K.L Christensen and M.J. Mulvany. Location of resistance arteries. *J Vasc Res*, 38:1–12, 2001.

[11] P. Dartevelle, E. Fadell, S. Mussot, A. Chapelier, P. Hervel, M. de Perrot, J. Cerrinal, F.L. Laduriel, D. Lehouerou, M. Humbert, O. Sitbon, and G. Simonneau. Chronic thromboembolic pulmonary hypertension. *Eur Respir J*, 23:637–648, 2004.

[12] F. Feihl, L. Liaudet, B. Waeber, and B.I. Levy. Hypertension: a disease of the microcirculation? *Hypertension*, 48:1012–1017, 2006.

[13] S. Franklin. Systolic blood pressure. *Am J Hypertens*, pages 49S–54S, 2004.

[14] Y.C. Fung. *Biomechanics: Circulation*. Springer, 1996.

[15] Y.C. Fung and S.S. Sobin. Theory of sheet flow in lung alveoli. *J Appl Physiol*, 26(4):472–488, 1969.

[16] J. Gao, W. Huang, and R.T. Yen. Microcirculation impedance analysis in cat lung. *J Biomech Eng*, 122(1):99–103, 2000.

[17] J.H. Gerrard and L.A. Taylor. Mathematical model representing blood flow in arteries. *Med & Biol Eng & Comput*, 15:611–617, 1977.

[18] D.P. Giddens, C.K. Zarins, and S. Glagov. The role of fluid mechanics in the localization and detection of atherosclerosis. *J Biomech Eng*, 115(4B):588–594, 1993.

[19] T. Griffith, P. Klassen, and S. Franklin. Systolic hypertension: an overview. *Am Heart J*, 149(5):769–775, 2005.

[20] K. Horsfield. Morphometry of the small pulmonary arteries in man. *Circ Res*, 42:593–597, 1978.

[21] W. Huang, R.T. Yen, M. McLaurine, and G. Bledsoe. Morphometry of the human pulmonary vasculature. *J Appl Physiol*, 81(5):2123–2133, 1996.

[22] A. Iberall. Anatomy and steady flow characteristics of the arterial system with an introduction to its pulsatile characteristics. *Math Biosci*, 1:375–385, 1967.

[23] Z.L. Jiang, G.S. Kassab, and Y.C. Fung. Diameter-defined strahler system and connectivity matrix of the pulmonary arterial tree. *J Appl Physiol*, 76(2):882–892, 1994.

[24] G.S. Krenz and C.A. Dawson. Flow and pressure distributions in vascular networks consisting of distensible vessels. *Am J Physiol Heart Circ Physiol*, 284:H2192–H2203, 2003.

[25] D.N. Ku. Blood flow in arteries. *Ann Rev Fluid Mech*, 29:399–434, 1997.

[26] D.J. Lang and B.L. Johns. Rat venule mechanical characteristics during venous pressure elevation. *Am J Physiol Heart Circ Physiol*, 252:H704–H713, 1987.

[27] J-W. Lankhaar, N. Westerhof, T.J.C. Faes, K.M.J. Marques, J.T. Marcus, P.E. Postmus, and A. Vonk-Noordegraaf. Quantification of right ventricular afterload in patients with and without pulmonary hypertension. *Am J Physiol Heart Circ Physiol*, 291:H1731–H1737, 2006.

[28] B.I. Levy, G. Ambrosio, A.R. Pries, and H.A. Struijker-Boudier. Microcirculation in hypertension: a new target for treatment? *Circulation*, 104:735–740, 2001.

[29] W.W. Nichols. Clinical measurement of arterial stiffness obtained from noninvasive pressure waveforms. *Am J Hypertens*, 18(1):3S–10S, 2005.

[30] W.W. Nichols and M.F. O'Rourke. *MacDonald's Blood flow in arteries: Theoretical, Experimental and Clinical Principles.* Edward Arnold, 4th edition, 1998.

[31] J.P. Noon, B.R. Walker, D.J. Webb, A.C. Shore, D.W. Holton, H.V. Edwards, and G.C. Watt. Impaired microvascular dilatation and capillary rarefaction in young adults with a predisposition to high blood pressure. *J Clin Invest*, 99:1873–1879, 1997.

[32] M.S. Olufsen. *Modeling the Arterial System with Reference to an Anesthesia Simulator.* PhD thesis, Roskilde University, 1998.

[33] M.S. Olufsen. Structured tree outflow condition for blood flow in larger systemic arteries. *Am J Physiol Heart Circ Physiol*, 276:H257–H268, 1999.

[34] M.S. Olufsen, C.S. Peskin, W.Y Kim, E.M. Pedersen, A. Nadim, and J. Larsen. Numerical simulation and experimental validation of blood flow in arteries with structured-tree outflow conditions. *Ann Biomed Eng*, 28:1281–1299, 2000.

[35] J.T. Ottesen, M.S. Olufsen, and J.K. Larsen. *Applied Mathematical Models in Human Physiology*. SIAM, 2003.

[36] A.J. Peacock and L.J. Rubin, editors. *Pulmonary Circulation: Diseases and their treatment*. Arnold, 2004.

[37] T.J. Pedley. *The Fluid Mechanics of Large Blood Vessels*. Cambridge University Press, 1980.

[38] T.J. Pedley. Arterial and venous fluid dynamics. In G. Pedrizzetti and K. Perktold, editors, *Cardiovascular fluid mechanics*. Springer, 2003.

[39] T.J. Pedley. Mathematical modelling of arterial fluid dynamics. *J Eng Math*, 47:419–444, 2003.

[40] A.S. Popel and P.C. Johnson. Microcirculation and hemorheology. *Annu Rev Fluid Mech*, 37:43–69, 2005.

[41] A.R. Pries, T.W. Secomb, and P. Gaehtgens. Design principles of vascular beds. *Circ Res*, 77:1017–1023, 1995.

[42] J.K. Raines. *Diagnosis and Analysis of Atherosclerosis in the Lower Limb*. PhD thesis, Massachusetts Institute of Technology, 1972.

[43] J.T. Reeves, J.H. Linehan, and K.R. Stenmark. Distensibility of the normal human lung circulation during exercise. *Am J Physiol Lung Cell Mol Physiol*, 288:L419–L425, 2005.

[44] A. Roy and M. Woldengerg. A generalization of the optimal models of arterial branching. *Bull Math Biol*, 44:349–360, 1982.

[45] G. Simonneau, N. Galie, L.J. Rubin, Langleben, W. Seeger, G. Domenighetti, S. Gibbs, D. Lebrec, R. Speich, M. Beghetti, S. Rich, and A. Fishman. Clinical classification of pulmonary hypertension. *J Am Coll Cardiol*, 43:5–12, 2004.

[46] S. Singhal, R. Henderson, K. Horsfield, K. Harding, and G. Cumming. Morphometry of the human pulmonary arterial tree. *Circ Res*, 33:190–197, 1973.

[47] R.L. Spilker, J.A. Feinstein, D.W. Parker, M. Reddy, and C.A. Taylor. Morphometry-based impedance boundary conditions for patient-specific modeling of blood flow in pulmonary arteries. *Ann Biomed Eng*, 35(4):546–559, 2007.

[48] N. Stergiopulos, D. Young, and T. Rogge. Computer simulation of arterial flow with applications to arterial and aortic stenosis. *J Biomech*, 25:1477–1488, 1992.

[49] W. Stooker, M. Gok, P. Sipkema, H.W.M. Niessen, A. Baidoshvili, N. Westerhof, E.K. Jansen, C.R.H Wildevuur, and L. Eijjsman. Pressure-diameter relationdhip in the human greater saphenous vein. *Ann Thorac Surg*, 76:1533–1536, 2003.

[50] C.A. Taylor and C.A. Figueroa. Patient-specific modeling of cardiovascular mechanics. *Annu Rev Biomed Eng*, 11:109–34, 2009.

[51] R.M. Tuder, J.H. Yun, A. Bhunia, and I. Fijalkowska. Hypoxia and chronic lung disease. *J Mol Med*, 85:1317–1324, 2007.

[52] H.B.M. Uylings. Optimization of diameters and bifurcation angles in lung and vascular tree structures. *Bull Math Biol*, 59:509–520, 1977.

[53] E.R. Weibel. *Morphometry of the Human Lung*. Springer-Verlag, 1963.

[54] J.R. Womersley. Method for the calculation of velocity, rate of flow and viscous drag in arteries when the pressure gradient is known. *J Physiol*, 127:553–563, 1955.

[55] T. Young. On the functions of the heart and arteries. *Phil Trans R Soc London*, 99:1–31, 1809.

[56] F.Y. Zhuang, Y.C. Fung, and R.T. Yen. Analysis of blood flow in cats lung with detailed anatomical and elasticity data. *J Appl Physiol*, 55(4):1341–1348, 1983.

[57] G. Zwas. On two step lax-wendroff methods in several dimensions. *Numer Math*, 20:350–355, 1973.